

Department of Engineering Materials and Biomaterials

Faculty of Mechanical Engineering

Silesian University of Technology

DOCTORAL DISSERTATION

“The influence of hybrid processes of surface microalloying on the structure and properties of surface layers of Ti and Ti alloy-based biomedical materials”

Oktawian Bialas, M.Sc., Eng.

Discipline: Materials Engineering

SUPERVISOR

Marcin Adamiak, DSc, Ph.D., Eng.

GLIWICE 2023

Abbreviations

AE – Acidic Etching
AFM – Atomic Force Microscopy
ALD – Atomic Vapour Deposition
BIC – Bone – Implant Contact
BII – Bone – Implant Interface
CA – Contact Angle
CP Ti – Commercial Pure Titanium
CVD – Chemical Vapour Deposition
DAPI - diamidino-2-phenylindole blue, fluorescent stain specific for DNA
DNA - Deoxyribonucleic Acid
EAM – Embedded Atom Method
EBSD – Electron Backscatter Diffraction
EDS – Energy Dispersive Spectroscopy
EEC – Electrical Equivalent Circuit
EIS – Electrochemical Impedance Spectroscopy
FBS – Fetal Bovine Serum
GID – Grazing Incidence Diffraction
IBAD – Ion Beam Assisted Deposition
IIT – Instrumented Indentation Technique
IMC – Intermetallic Compound
LC₅₀ – Lethal Concentration 50% (in population)
LSTO – Laser Surface Texturing Oxidation
MD – Molecular Dynamics
MRI – Magnetic Resonance Imaging
NHDF – Neonatal Human Dermal Fibroblasts
OWRK - The Owens, Wendt, Rabel and Kaelble method
PBC – Periodic Boundary Conditions
PLD – Pulsed Laser Deposition
PVD – Physical Vapour Deposition
RVE – Representative Volume Element
SB – Sandblasting
SEM – Scanning Electron Microscopy
SFE – Surface Free Energy
TAH – Total Artificial Heart
TCT – Thermal – Chemical Treatment
TEM – Transmission Electron Microscopy
VAD – Ventricular Assist Device
XRD – X – ray Diffraction

Table of contents

1. Introduction	17
2. State-of-the-art	20
2.1. Biomedical materials	20
2.1.1. Metals used in medicine	21
2.1.2. Ti and its alloys.....	22
2.1.3. Gold additives and coupling with Ti	23
2.2. Surface engineering in medicine	27
2.2.1 Surface engineering as key to the tissue-material interface	27
2.2.2 Selected methods for modifying surface layers.....	32
2.3 Laser impact on the solid matter	39
2.3.1 Physical basis of the laser impact on the solid matter	40
2.3.2 Laser melting and alloying	42
3. Aim and thesis of the work.....	43
4. Experimental section	46
4.1 Research methodology	46
4.1.1 Research plan.....	46
4.1.2 Materials	47
4.1.3 Coating application.....	48
4.1.4 Laser alloying	49
4.2 Methodology for evaluating the material obtained	50
4.2.1 Numerical analysis	50
4.2.2 Hardness assessment by Nanoindentation simulation study	59
4.2.3 Roughness tests.....	60
4.2.4 Light microscopy	61
4.2.5 Scanning Electron Microscopy (SEM).....	61
4.2.6 X Ray Diffraction Analysis	61
4.2.7 Electron Backscatter Diffraction (EBSD)	62
4.2.8 Transmission Electron Microscopy (TEM)	62
4.2.9 Atomic Force Microscopy (AFM).....	63

4.2.10	Wetting Angle measurements.....	63
4.2.11	Corrosion Tests.....	63
4.2.12	Tribological tests	64
4.2.13	Nanohardness test	64
4.2.14	Cytotoxicity tests	65
5	Results and Discussion	67
5.1	Numerical Analysis results.....	67
5.2	Indentation test for understanding the mechanical response of Ti and Ti ₃ Au slabs at nanoscale	69
5.3	Roughness Tests	71
5.4	Light microscopy.....	72
5.5	Scanning Electron Microscopy on cross sections	76
5.6	Energy Dispersive Spectroscopy.....	80
5.7	XRD.....	83
5.8	EBSD.....	87
5.9	TEM.....	92
5.10	AFM	99
5.11	Wetting Angle	101
5.12	Corrosion	103
5.13	Tribological tests	116
5.14	Nanoindentation test.....	121
5.15	Cytotoxicity	124
6	Conclusions.....	127
7	Acknowledgements.....	129
8	Bibliography.....	129

Abstract

In the dissertation presented here, a hybrid approach was used to obtain layers containing the Ti_3Au phase, enabling new potential biomedical applications for materials modified in this way. The process involved the use of both an electrochemical deposition techniques to deposit gold Au onto titanium Ti and $Ti_{13}Zr_{13}Nb$ alloy, and subsequent laser microalloying to obtain a multilayer surface enriching the base material in Au. The obtained samples were then analysed in order to determine the composition and characteristics of the microstructure and functional properties.

In the course of the study, research techniques such as light microscopy, atomic force microscopy, scanning electron microscopy, transmission electron microscopy, backscattered electron diffraction, X-ray diffraction, contact roughness measurement methods, wettability measurement, corrosion studies including electroimpedance spectroscopy, as well as tribological studies, nanohardness studies and cytotoxicity studies were used. Empirical studies were preceded by numerical simulation of heat flow and nanoindentation.

The results of this study showed that the hybrid approach was effective in producing the Ti_3Au phase, and that the gold enriched materials produced by this original method had desirable properties such as high biocompatibility, corrosion resistance, and better tribological properties than the base materials used for this study. This research has the potential to contribute to the development of new materials for use in the field of biomedicine.

Streszczenie

W prezentowanej pracy doktorskiej zastosowano podejście hybrydowe w celu uzyskania warstw zawierających fazę Ti_3Au , co umożliwia nowe potencjalne zastosowania biomedyczne materiałów w ten sposób modyfikowanych. Proces obejmował wykorzystanie elektrochemicznego osadzania złota Au na powierzchni materiałów - tytanu Ti i jego stopu $Ti_{13}Zr_{13}Nb$, a następnie mikrostopowania laserowego do uzyskania wielowarstwowej powierzchni wzbogacając materiał bazowy w Au. Uzyskane próbki poddano następnie analizie w celu określenia składu chemicznego, charakterystyk mikrostruktury oraz właściwości użytkowych.

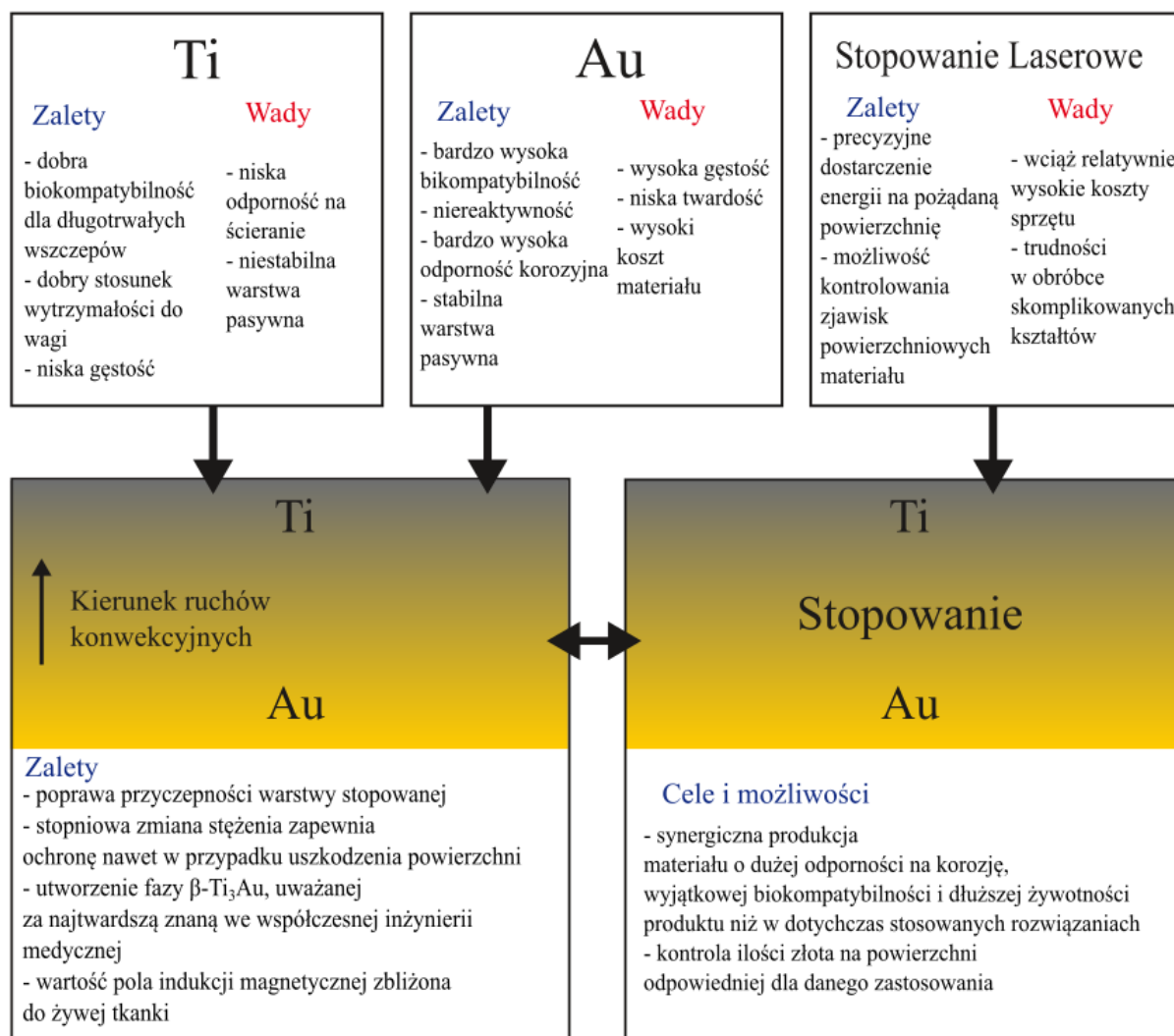
W trakcie realizacji pracy wykorzystano takie techniki badawcze jak mikroskopia świetlna, mikroskopia sił atomowych, skaningowa mikroskopia elektronowa, transmisyjna mikroskopia elektronowa, dyfrakcja elektronów wstecznie rozproszonych, dyfrakcja rentgenowska, kontaktowe metody pomiaru chropowatości, pomiar zwilżalności, badania korozyjne, w tym spektroskopia elektroimpedancyjna, a także badania tribologiczne, badania nanotwardości oraz badania cytotoksyczności. Badania empiryczne poprzedzono symulacją numeryczną przepływu ciepła i nanoindentacji.

Wyniki badań wykazały, że podejście hybrydowe pozwoliło na wytworzenie fazy Ti_3Au , a materiały wzbogacone w złoto wytworzone tą oryginalną metodą miały pożądane właściwości, takie jak wysoka biokompatybilność, odporność na korozję i lepsze właściwości tribologiczne w porównaniu do materiałów bazowych użytych do badań. Wyniki przedstawionej pracy doktorskiej mogą potencjalnie przyczynić się do opracowania nowych materiałów do zastosowania w dziedzinie biomedycyny.

Streszczenie poszerzone

Streszczenie zawiera w szczególności odpowiednio: zakres, cele i tezy rozprawy, opis przedmiotu badań, główne wyniki i wnioski, najważniejsze schematy, rysunki, wykresy, tabele.

Przedstawiona praca doktorska skupia się na hybrydowym wytwarzaniu nowoczesnych materiałów mogących znaleźć zastosowanie w sektorze materiałów biomedycznych. Dysertacja koncentruje się na zastosowaniu nakładania elektrochemicznego warstwy złota, a następnie powierzchniowej obróbce laserowej materiału z powłoką w celu wytworzenia na powierzchni mikrostruktury wielofazowej. Zastosowane materiały wyjściowe, tytan Ti Grade II oraz jego stop $Ti_{13}Zr_{13}Nb$ są szeroko stosowanymi materiałami wykorzystywanymi do biomedycznych zastosowań w organizmie ludzkim. Przeprowadzony przegląd literatury wskazuje na szerokie zastosowanie stopów tytanu wynikające z ich dobrej odporności na korozję poprzez szybko tworzącą się (aczkolwiek niestabilną) warstwę pasywną, dobre właściwości mechaniczne w stosunku do gęstości, co pozwala na zmniejszenie masy wyrobów oraz ogólną dobrą biokompatybilność w porównaniu do innych metalicznych materiałów biomedycznych. Wadami stopów tytanu jest natomiast słaba odporność na ścieranie, powodowanie artefaktów w trakcie obrazowania za pomocą rezonansu magnetycznego oraz wymagająca poprawy odporność korozyjna. Złoto jest znanym metalem szlachetnym wykorzystywanym w przemyśle jubilerskim. Złote wypełnienia i elementy protez były również szeroko stosowane w protetyce stomatologicznej w ubiegłym stuleciu. Współcześnie złoto jest również popularne w medycynie jako skuteczny system dostarczania leków. Z punktu widzenia mechaniki protez, główną wadą złota jest jego wysoka gęstość i masa, a także niska twardość. Jednak połączenie złota oraz tytanu w odpowiednich proporcjach z użyciem obróbki laserowej, może doprowadzić do wytworzenia fazy, która będzie charakteryzowała się właściwościami pożądanymi dla potencjalnych implantów długotrwałych, a więc lepszą niż materiał bazowy twardością, niższym zużyciem trybologicznym oraz lepszą odpornością korozyjną przy równocześnie niskiej cytotoksyczności. Najważniejsze wady, zalety a także możliwości płynące z zastosowania podejścia wykorzystanego w pracy doktorskiej zostały przedstawione na rys 1.



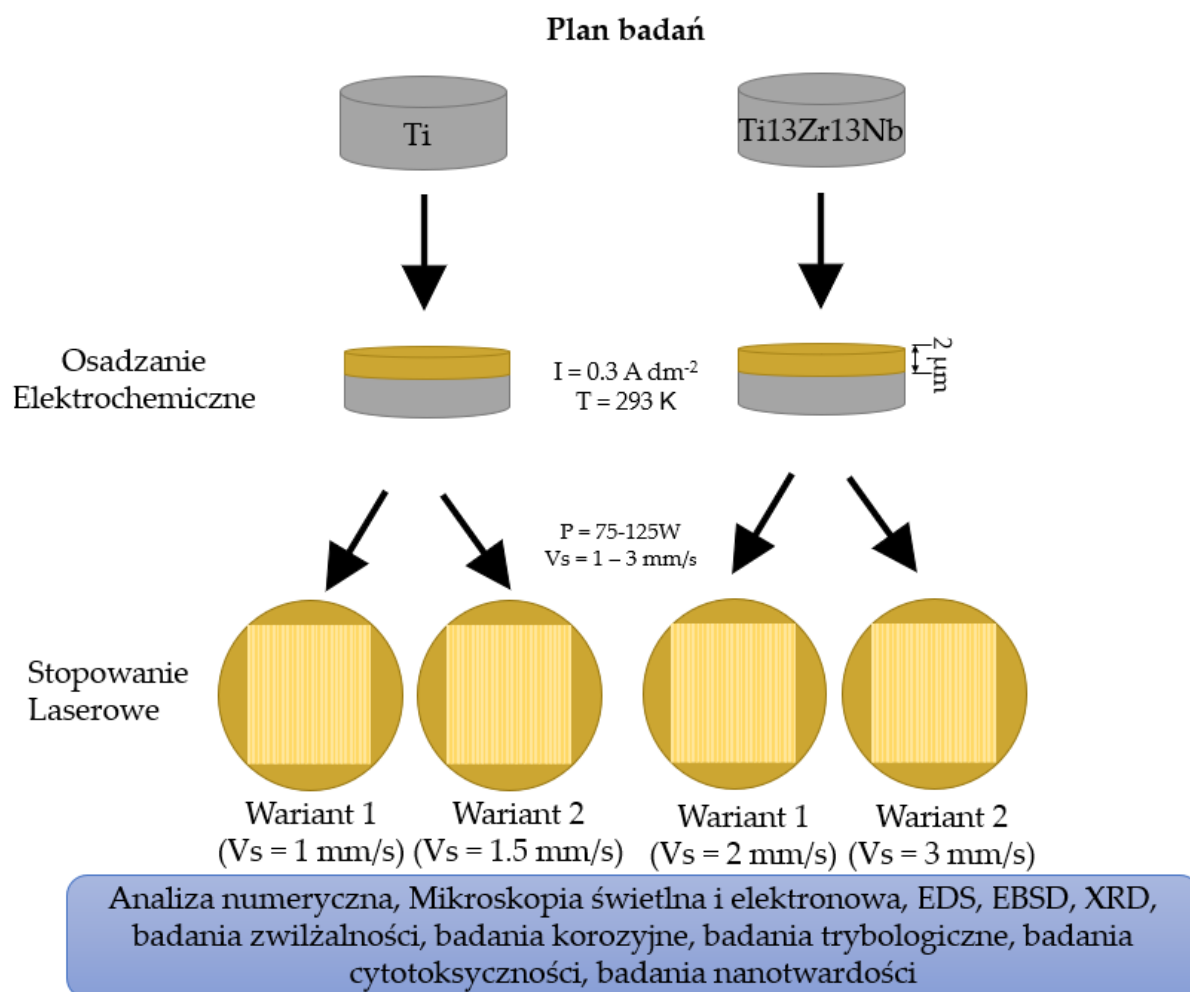
Rysunek 1. Diagram uzasadnienia celów oraz możliwości uzasadniających podjęcie badań w ramach realizowanej pracy

Celem zaplanowanych badań była ocena wpływu stopowania laserowego tytanu Ti oraz jego stopu Ti₁₃Zr₁₃Nb pokrytych mikrometryczną warstwą złota na strukturę i właściwości powierzchni tych materiałów do dalszych zastosowań biomedycznych. W zakres prac badawczych włączono w szczególności, określenie warunków niezbędnych do elektrochemicznego osadzania złota na tytanie i jego stopach, oraz określenie wpływu laserowego stopowania na zjawiska zachodzące w obrębie warstwy wierzchniej, następnie wskazanie warunków pozwalających na wytworzenie oczekiwanego składu fazowego warstwy modyfikowanej. Ocena uzyskanych materiałów odbyła się z wykorzystaniem szeregu technik badawczych wykorzystywanych w dyscyplinie inżynieria materiałowa takich jak, badania

technikami mikroskopii świetlnej, elektronowej oraz sił atomowych, badania dyfrakcji rentgenowskiej, testy odporności na korozję, ocenę właściwości mechanicznych takich jak nanotwardość, chropowatość, zużycie ściernie. Dokonano również oceny cytotoksyczności otrzymanych materiałów. Dodatkowo w celu określenia modelu oddziaływania wiązki lasera z wytworzoną warstwą powierzchniową posłużono się analizą numeryczną.

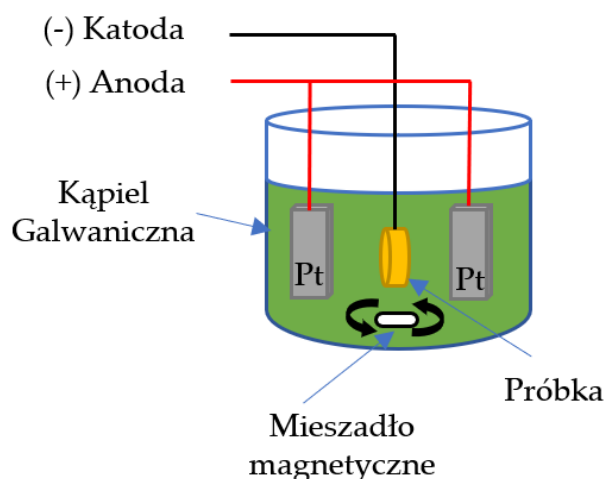
Zaplanowane badania eksperymentalne obejmowały przygotowanie powłoki złota o grubości około 2 μm nałożonej na każdy z materiałów bazowych (Ti i Ti₁₃Zr₁₃Nb) za pomocą procesu elektrochemicznego. Szczegóły procesu osadzania powłoki, takie jak rodzaj elektrolitu czy gęstość prądu, zostały określone i zoptymalizowane, aby uzyskać jednolitą i przylegającą powłokę złota. Po nałożeniu powłoki Au, pokryte materiały zostały poddane mikrostopowaniu laserowemu z zastosowaniem zmiennych parametrów procesu. Parametry i sam proces stopowania laserowego zostały dobrane, aby osiągnąć jednorodną pod względem składu chemicznego i fazowego warstwę wierzchnią materiału wzbogaconego w Au.

Wybrane parametry obróbki laserowej zostały poddane wnikliwej analizie materiałoznawczej. Badania obejmowały analizę numeryczną, mikroskopię świetlną, skaningową mikroskopię elektronową (SEM), transmisyjną mikroskopię elektronową (TEM), dyfrakcję elektronów wstecznie rozproszonych (EBSD), dyfrakcję rentgenowską (XRD), testy zwilżalności, odporności na korozję, badania trybologiczne, badania cytotoksyczności i testy nano-twardości. Wyniki tych badań zostały wykorzystane do porównawczej oceny właściwości materiałów w stanie wyjściowym, po nałożeniu powłoki oraz po stopowaniu laserowym. Plan badań w postaci diagramu został przedstawiony na Rys. 2.



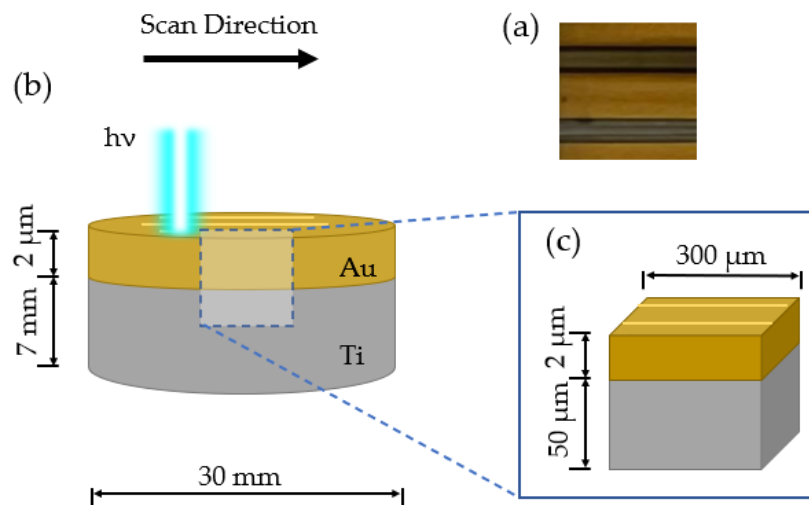
Rysunek 2. Schemat prowadzenia eksperymentu

Odpowiednio przygotowane - wypolerowane, umyte i odtłuszczone próbki tytanu wytrawiono we wrzącym roztworze kwasu solnego (HCl) (50% v/v). Bezpośrednio przed procesem złocenia, wytrawione próbki polaryzowano katodowo przez 10 minut w 1 molowym roztworze kwasu siarkowego (H₂SO₄), w celu całkowitej redukcji tlenku tytanu obecnego na powierzchni próbki. Proces złocenia przeprowadzono przy użyciu prądu stałego o natężeniu 0,3 A dm⁻² w komercyjnej kąpieli galwanicznej z wykorzystaniem urządzenia KIKUSUI PWR 800H (Kikusui, Yokohama, Japonia). Schemat procesu osadzania został przedstawiony na rys. 3



Rysunek 3. Schemat osadzania galwanicznego złota

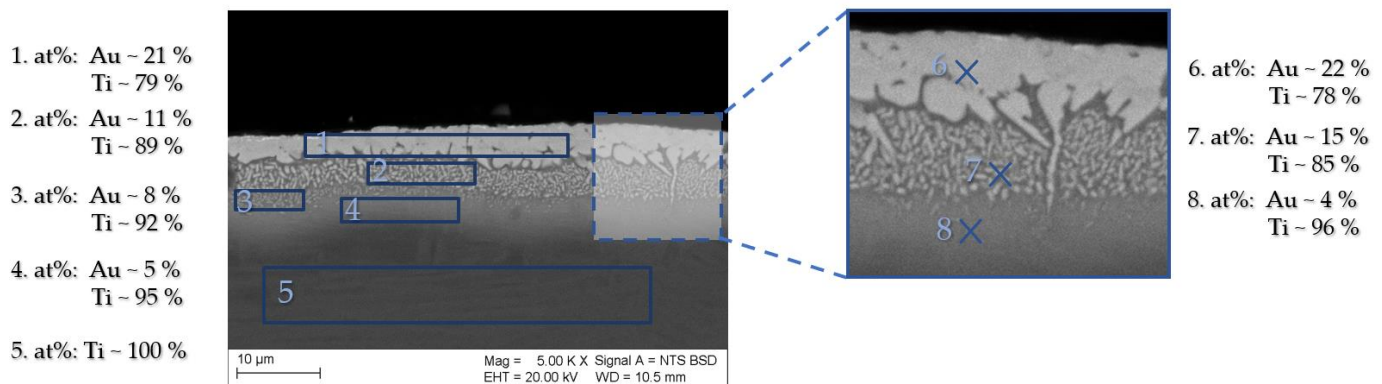
W kolejnym kroku próbki poddano obróbce laserowej. Eksperyment wykonano przy użyciu urządzenia Trumph TruDisk 3302 opartego na neodymowym Nd: Y3Al5O12 laserze o ciągłym modzie pracy z wiązką w kształcie typu flat-top o długości fali 1030 nm. Na podstawie symulacji numerycznej oraz eksperymentalnie dobrano energię wiązki układu, która pozwalała na kontrolowane przetopienie materiału obrabianego. Eksperymenty prowadzono w atmosferze gazu ochronnego - argonu. W celu uzyskania jednolicie przetopionej warstwy (co wymaga stopienia obu składników o różnych temperaturach topnienia, odpowiednio 1668°C dla Ti i 1064°C dla Au) o grubości nieprzekraczającej 10 μm , zastosowano wiązkę rozogniskowaną +10mm. Zastosowanie rozogniskowanej wiązki zmienia rozkład ciepła, a tym samym modyfikuje również zmiany w mikrostrukturze i kinetyce przemian fazowych. Rozogniskowanie powoduje, że próbka nagrzewa się wolniej, na większym obszarze ale na mniejszej głębokości. Z uwagi na fakt, że konwekcja w krystalicznych ciałach stałych charakteryzujących się zwartym wypełnieniem przestrzeni jest utrudniona i zachodzi wyłącznie w jeziorce przetopu, możliwym stało się uformowanie fazy TiAu na pożądanej (kontrolowanej parametrami i rozogniskowaniem wiązki) głębokości. Wyższe stężenia Au było obecne przypowierzchniowo, a w miarę wnikania do rdzenia materiału stężenie Ti wzrastało gradientowo. Schemat procesu obróbki laserowej oraz reprezentatywny model objętościowy wykorzystany do symulacji numerycznej został przedstawiony na Rys 4.



Rysunek 4. Widok próbki Ti-Au: a) powierzchnia po wykonaniu mikrostopowania laserowego b) schemat obróbki laserowej c) reprezentatywny element objętościowy (RVE) próbki do analizy metodą elementów skończonych. Schematy w b i c nie są proporcjonalne (oś pionowa jest znacznie rozciągnięta w stosunku do osi poziomej), aby umożliwić właściwą widoczność pokrytej cienkiej warstwy

Wyniki ilościowych analiz EDS wykonane po przeprowadzeniu eksperymentu potwierdziły zmiany składu chemicznego w wyniku przetopienia próbek na bazie tytanu i oznaczonych TiAu 1 mm/s, TiAu 1,5 mm/s, oraz na bazie stopu tytanu i oznaczonych Ti13Zr13NbAu 2 mm/s oraz Ti13Zr13NbAu 3 mm/s. Na prezentowanych obrazach można wyróżnić kilka głównych obszarów zmian koncentracji. Wyniki otrzymane dla próbki TiAu 1.5 mm/s, gdzie widoczne są cztery obszary o różnych koncentracjach pierwiastków zostały zaprezentowane na Rys. 5. W regionie 1 stosunek koncentracji atomów Ti do Au jest bliski wartości oczekiwanej dla fazy Ti_3Au .

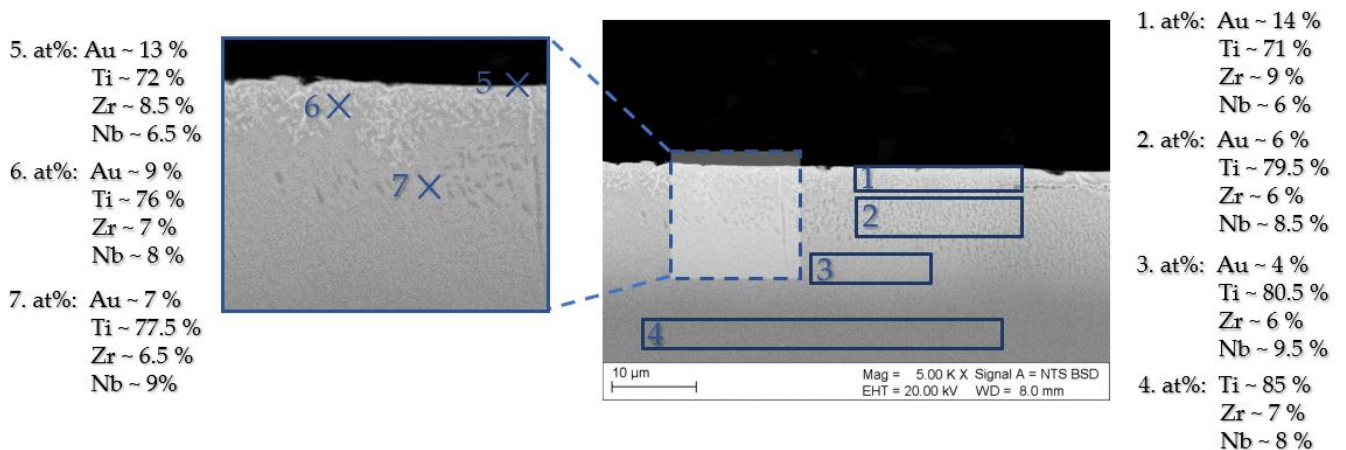
TiAu 1.5mm/s



Rysunek 5. Wyniki ilościowej analizy EDS dla próbki TiAu 1,5 mm/s

W przypadku grupy próbek opartych na Ti13Zr13Nb zmiany są bardziej niejednorodne, a obszary o podobnej koncentracji Au trudniejsze do wyznaczenia. Dla przedstawionej na Rys. 6 próbki Ti13Zr13NbAu 2 mm/s można wyróżnić trzy obszary, w których zawartość Au maleje od wartości maksymalnej (ok. 14 at%) do 4 at%.

Ti13Zr13NbAu 2 mm/s

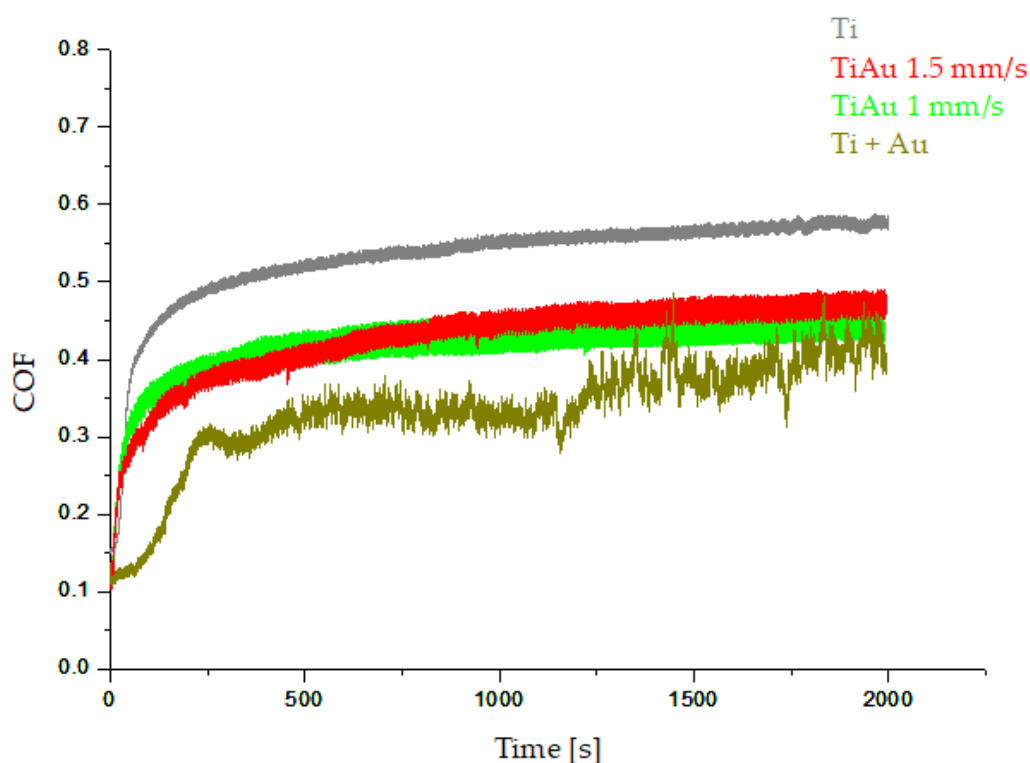


Rysunek 6. Wyniki ilościowej analizy EDS dla próbki TiAu 1,5 mm/s

Do badań odporności tribologicznej użyto tribometru CSM w celu wykonania próby zużycia metodą ball-on-plate. Jako przeciwpróbkę zastosowano kulkę ZrO₂ o średnicy 5,6 mm. Badania

przeprowadzono w roztworze Ringera (NaCl - 8,6 g/cm³, KCl - 0,3 g/cm³, CaCl₂ × 2H₂O - 0,33 g/cm³) w temperaturze pokojowej i pH 7,4. Test zużycia przeprowadzono z amplitudą 4 mm przy obciążeniu 2 N i częstotliwością 1,25 Hz w ilości 2500 cykli i szybkości akwizycji równej 4,0 Hz. Warunki testu zgodnie z literaturą odpowiadały symulacji fizjologicznego chodu. Wartość współczynnika tarcia COF obliczono na podstawie danych, które zostały pobrane podczas eksperymentu.

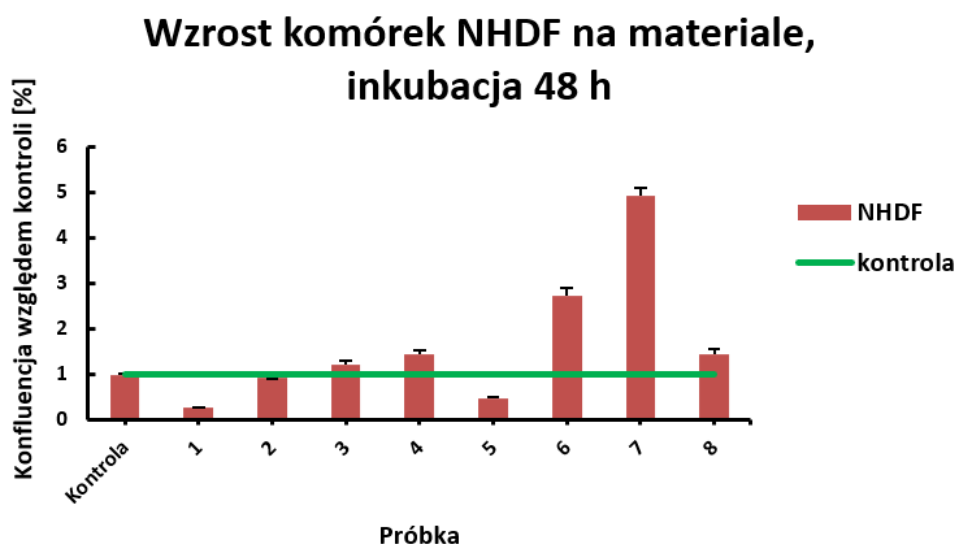
Na rys. 7 odnoszącym się do badania grupy próbek na bazie Ti przy założonych parametrach badania, z wykresów zależności COF od czasu widać, że dla złota osadzonego elektrochemicznie i niepoddanego obróbce laserowej, warstwa złota ściera się po około 250s, po czym COF systematycznie wzrasta, aż do osiągnięcia COF równego 0,35, bliskiego parametrom TiAu 1,0mm/s i 1,5mm/s. Ponadto COF osiągnięty przez czysty Ti jest najwyższy (0,48), co świadczy o szybszym zużyciu materiału. Próbki poddane obróbce laserowej ustabilizowały się na podobnym do siebie poziomie (średnio 0,40).



Rysunek 7. Wykres zależności współczynnika tarcia od czasu dla próbek o podłożu z Ti

Ponad to, w testach cytotoksyczności, większość z badanych materiałów nie wykazała gorszej biokompatybilności od kontrolnej powierzchni plastiku hodowlanego (dołek płytki

polistyrenowej, format 6-well, Sarstedt). Wyjątkiem mogą być próbki oznaczone numerami 1 i 5 (Tab. 1.), gdzie ilość zliczonych komórek na skanowaną powierzchnię była mniejsza od nietraktowanej kontroli (K). Pozostałe materiały wykazują zgodność, co do braku toksyczności wobec prawidłowej linii fibroblastów ludzkich NHDF (Rys. 8).



Rysunek 8. Gęstość komórek NHDF na materiałach, 48 h inkubacji. Wyniki ze zliczeń jąder komórkowych ze skanowanej powierzchni. Wyniki przedstawiono jako procentową zmianę względem populacji kontrolnej; średnia z 3 eksperymentów +/- SD

Tabela 1. Oznaczenie próbek w testach cytotoksyczności

nr	1	2	3	4	5	6	7	8
próbka	Ti	Ti + Au	TiAu 1 mm/s	TiAu 1.5 mm/s	Ti13Zr13Nb + Au	Ti13Zr13NbAu 2 mm/s	Ti13Zr13NbAu 3 mm/s	Ti13Zr13Nb

W 48-godzinnym teście wzrostu i tworzenia biofilmu na materiałach można stwierdzić, że modyfikowane powierzchnie nadają się do aplikacji *in vitro*, ponieważ efekty wzrostu nie zostały obniżone poniżej wartości 70% ilości komórek kontrolnych (hodowanych na polistyrenowych plastikach kontrolnych). Wszystkie czynności i badania wykonywano w warunkach sterylnych, zgodnie z wytycznymi oceny cytotoksyczności wg normy ISO 10993-5 dla biologicznej ewaluacji materiałów medycznych za pomocą testów *in vitro*. W przypadku braku obniżenia frakcji przeżywającej poniżej 70 % kontroli nie uznaje się wpływu badanego materiału jako cytotoksycznego.

Badania zawarte w pracy doktorskiej nad wytworzeniem materiału prezentującego cienką warstwę powierzchniową wzbogaconą w Au na bazie materiału stosowanego w medycynie i kardiologii - Ti i jego stopu nowej generacji Ti13Zr13Nb, pozwoliły na sformułowanie następujących wniosków:

1. Tytan i jego stopy mają silną tendencję do tworzenia niejednorodnej, niestabilnej warstwy pasywnej złożonej z tlenków, co wymusza stosowanie trawienia bezpośrednio przed procesem elektrochemicznego osadzania złota.
2. Skład kąpieli trawiącej, czas trawienia oraz temperatura kąpieli mają decydujący wpływ na chropowatość i topografię materiału. W celu zapewnienia odpowiednio niskiej chropowatości (zbyt wysoka chropowatość może spowodować lokalne spowolnienie przepływu krwi i w konsekwencji sprzyjać powstawaniu skrzeplin), dobór parametrów procesu prowadzono tak, aby uzyskać materiał o docelowej chropowatości niższej niż $Ra = 1,04 \mu\text{m}$ - odpowiadającej chropowatości obwodowej naczynia wieńcowego. Elektrochemiczne osadzanie złota skutkuje niewielkim spadkiem Ra dla Ti i wzrostem Ra dla materiału Ti13Zr13Nb, ale nie uwidoczniło wzrostu chropowatości powyżej założonej wartości.
3. Numeryczna analiza przepływu ciepła pozwoliła na wstępną ocenę osiągniętej temperatury podczas obróbki laserowej, pozwalając na stwierdzenie, że przy wybranych parametrach zarówno materiał podłoża, jak i powłoki (Au) znajdowały się w stanie ciekłym, umożliwiając dynamiczną wymianę masy między sobą w wyniku ruchów konwekcyjnych. Zjawisko to potwierdzono w badaniach przy użyciu mikroskopii świetlnej oraz elektronowej.
4. Dobór parametrów procesu z wykorzystaniem obróbki laserowej pozwolił na ustalenie okna parametrów zapewniających dobrą jakość powłoki po przetopieniu (uniknięcie z jednej strony pęknięć pod wpływem naprężeń hartowniczych i zbyt intensywnej konwekcji cząstek złota uniemożliwiającej koncentrację stechiometryczną pozwalającą na krystalizację fazy Ti_3Au , a z drugiej strony zbyt niskiego przetopienia i braku kontroli przetopienia). Wykazano, że najlepszą jakość powłoki uzyskuje się przy mocy wiązki $P = 100 \text{ W}$, prędkości skanowania wiązki $= 1\text{-}3 \text{ mm/s}$ i rozogniskowania wiązki $+ 10 \text{ mm}$.
5. Analiza z wykorzystaniem szerokiej gamy technik mikroskopowych zarówno w postaci obserwacji obrazu, jak i określenia składu fazowego, analiza XRD pozwoliły na ocenę poszczególnych obszarów przekroju poprzecznego uzyskanych warstw. Po obróbce laserowej otrzymano wielowarstwowe warstwy o różnym stężeniu –złota Au. Obecność fazy $\beta\text{-Ti}_3\text{Au}$ w postaci drobnych krystalitów ujawniono również w analizie EBSD i TEM.

6. Badania zwilżalności powierzchni wskazały na wzrost wartości kąta zwilżania w kierunku hydrofobowości po każdym kolejnym etapie obróbki materiału, jednak ostatecznie otrzymana powierzchnia nadal znajduje się w zakresie hydrofilowym, co ma szczególnie pozytywne znaczenie dla możliwości zastosowania materiału do celów biomedycznych.

7. Badania odporności na korozję generalnie wskazywały na poprawę właściwości korozyjnych próbek wzbogaconych w złoto. Badania technikami EOC, analiza krzywych Tafela oraz EIS pozwoliły na korzystną ocenę materiału pod względem zachowania korozyjnego. Należy jednak zwrócić uwagę na spadek odporności korozyjnej w przypadku lokalnych zmian koncentracji złota charakterystycznych dla wariantu Ti13Zr13Nb 3 mm/s, w którym taka zmiana koncentracji prowadzi do powstawania mikroogniw korozyjnych.

8. Badania odporności tribologicznej w warunkach obciążeń imitujących fizjologiczny chód wykazały zmniejszenie współczynnika tarcia COF, dla wariantów próbek z podłożem Ti, jest to niewątpliwie związane z kombinacją obróbki laserowej i obecnością fazy Ti₃Au charakteryzującej się lepszymi właściwościami tribologicznymi oraz wyższą twardością. Natomiast dla próbek z podłożem Ti13Zr13Nb następuje wzrost COF, co nie jest korzystne. Powłoka Au bez obróbki laserowej ściera się po 250 s eksperymentu.

9. Badania nanotwardości, podobnie jak analiza numeryczna nanotwardości, wykazały wzrost twardości dla próbek poddanych obróbce laserowej posiadających w swoim składzie fazy Ti₃Au. Zasadna wydaje się dalsza optymalizacja procesu w celu maksymalizacji udziału Ti₃Au w składzie powłoki.

10. Testy cytotoksyczności nie wykazały toksycznego wpływu materiałów badanych na przeżywalność komórek posianych na ich powierzchni.

Badania przeprowadzone w niniejszej rozprawie pozwalają tym samym na pozytywną ocenę materiału zarówno pod względem właściwości mechanicznych jak i biologicznych oraz otwierają drogę do dalszych analiz zgodnie z normą PN-EN 10993-1:2010, "Biologiczna ocena wyrobów medycznych - Część 1: Ocena i badania w procesie zarządzania ryzykiem".

1.Introduction

"We have to remember that what we observe is not nature in itself but

nature exposed to our method of questioning."

— *Werner Heisenberg*

In the second half of the 18th century, the British chemist, clergyman and educator Joseph Priestley isolated substances such as oxygen, ammonia, sulphuric acid and hydrogen chloride through his research work. In 1772, Priestley synthesized nitrous oxide (N₂O). Initially used as a "laughing gas", the new substance was spread mainly at fairs for entertainment shows. At the time, it was unimaginable that this compound, along with chloroform (CHCl₃) and diethyl ether ((C₂H₅)₂O), would revolutionize medicine in the future [1,2].

Here, more than 60 years later in the span of four years (1844-1847), Horace Wells, William Morton, and James Simpson performed the first painless operations on their patients, the success of which reverberated throughout a world previously filled with pain and fear of surgical intervention. Bertrand Gosset described the history of surgery and its origins in 1956 in the following words: "The history of surgery is the history of the last 100 years, which started in 1846 with the discovery of narcosis and the possibility of no – pain operation. Everything, which was before, is just a night of ignorance, pain and barren groping in the dark" [3,4].

The possibilities created by anaesthesia were the catalyst for the development of surgery, and it is thanks to this that we know the field in its present form. As surgeries become more extensive and attempts to treat complex conditions increase, there is a need for a specific supply of specialized instruments and materials that have the ability to replace malfunctioning parts of the patient's body. Nowadays, an interdisciplinary research team made up of specialists from various fields is responsible for the success of a treatment. Only the synergistic action of several branches of science has the potential to advance the current state of knowledge.

In addition to the rapidly developing biotechnology, attempts to 'grow' organs using stem cells or genetics, the engineering of biomedical materials is also finding its place. Thanks to archaeological discoveries, it is known that the first attempts at prosthesising lost limbs and even the beginnings of successful open cranial operations (trepanation) were already made in the Neolithic period [5], however, the conscious shaping of chemical and phase structure, or the in-depth knowledge of human anatomy, is certainly attributable to our time.

An achievement similar to the discovery of anaesthesia, which will change the face of science forever in the current state of knowledge, is unattainable, but during the work on this dissertation, the guiding Authors' thought was to push the current state of knowledge at least a small step forward, to make the world at least a little more patient-friendly.

The aim of the planned research was to assess the impact of laser microalloying on titanium base material coated by gold on the structure and properties of selected - most sensitive for cytotoxicity of biomedical materials' surfaces. The combination of this type of treatment with the production of advanced thin multiphase/multilayer electrochemical coatings will allow us to obtain a gradient of the concentrations of the phases/mixtures constituting the coating as a function of depth from the surface. The proceeding will also improve the adhesion of the substrate-coating layer, which will ensure an increase in the durability of biomedical implants and significantly extend the product's lifetime in the working environment (organism). This state will be achieved without causing adverse reactions of the immune system, such as metallosis or thrombosis [6,7]. Moreover, the application of the multilayer coating will ensure appropriate operating conditions even in the case of incorrect implantation with partial damage to the surface, which so far has made the success of the implantation dependent on the operator's skills [8].

The purpose of the research project is to apply surface enriched layers using laser microalloying in two different variations, which is the original method for improving the connection between gold and titanium. The tests will be conducted on two base materials using a range of parameters. The best performing parameters for each base material will be carefully characterized and tested for their potential utility properties.

Specific objectives of the dissertation:

- Definition of the conditions necessary for the electrochemical deposition of gold on titanium and its alloys, due to the rapid formation of oxides on the titanium surface, the deposition will require a strictly defined procedure.

- Definition of the influence of laser alloying on the surface phenomena within the surface layer, indication of the conditions under which the most advantageous intermetallic composition is formed using TEM and XRD technics
- Evaluation of the obtained materials: corrosion resistance, description of the mechanical properties, visualisation of the surface through the scanning electron microscopy SEM and transmission electron microscopy TEM
- Checking the biological response through cytotoxicity tests as the most critical factor for future technology implementation and as a first step in the assessment of the properties according to ISO 10993-1:2018 - *Biological evaluation of medical devices - Part 1: Evaluation and testing within a risk management process*) [9–13].

2.State-of-the-art.

2.1. Biomedical materials

Due to the specific working environment, the materials used for medical implants require strictly defined physical and chemical properties. The criteria according to which medical devices are designed and tested stem from the desire to maximise the usefulness of the implant in the working environment, but above all to ensure the patient's safety [12]. Depending on their exact purpose and chemical nature, materials used for medical purposes must be designed to withstand factors such as corrosion, continuous and cyclic loading, repeated bending, abrasion (tribological resistance), protein adsorption or fluid absorption. They must have the lowest possible thrombogenicity (tendency to clot), calcification (calcification due to deposition of calcium salts in the soft tissues and on the surface of the material), minimal cytotoxicity and adequate magnetic and electrical properties. They must therefore be as immunologically inactive as possible [10,14,15]. The most common way of shaping the best properties is to model the specificity of the replaced tissue, allowing the biophysical contact bond to be realised and the load transfer to be as smooth (non-stiff) as possible. The set of criteria for evaluating a material's suitability for medical purposes is referred to as *biocompatibility* in the literature. This characteristic determines how well the material functions in the tissue environment, which

ions. The second important group of elements is the semi-metals. Although they do not always form positive ions, they have good electrical and conductive properties, making them components of many alloys used successfully in medicine [9].

The most common metallic materials can be broadly classified into consecutive and property-differentiated groups: Austenitic Cr - Ni - Mo steels, cobalt matrix alloys, titanium alloys and Ni - Ti shape memory alloys, the so-called Nitinol. In addition to the different properties that determine their specific application, they are characterised by different biotolerance. The applicability of each group has been described and strictly defined by their respective PN - ISO, ASTM, DIN, ISO and other standards, which require manufacturers of these products to maintain high standards in terms of both quantity and quality of critical factors, i.e. mechanical and physical characteristics, chemical and/or phase composition and electrochemical properties [12,18,19].

2.1.2. Ti and its alloys

Today, titanium alloys are the most widely used metals because of their special properties, which meet the criteria for biocompatibility in a way that is unattainable for other materials. These include, in particular, high corrosion resistance in a tissue environment, low density with appropriate mechanical properties, paramagnetic properties, low electrical and thermal conductivity and inertness to the biological environment. In addition, the ability to lower the longitudinal modulus of elasticity (Young's modulus) is important for implants that work with bone [11,13,19,20].

The most widely recognised titanium alloy is Ti6Al4V. It has been used clinically in the last century and even today, but today it is avoided for long-term implants because of the risk of the release of the toxic elements vanadium and aluminium when it is used. Due to this fact, 'vanadium- and alumina-free' alloys are more readily used. These are alloys such as Ti6Al7Nb (ASTM F1295 standard), Ti13Nb13Zr (ASTM F1295 standard) or Ti12Mo6Zr (ASTM F1813 standard) [21–23]. The ability to spontaneously generate a passive layer and thus have good corrosion resistance, as well as a high strength-to-density ratio, are two of the most distinctive characteristics of superior behavior in titanium [24]. But easily formed passive layer can contain imperfections (inclusions and discontinuities—weak spots) that might lead to the onset of corrosion; therefore it does not completely guarantee corrosion protection [25]. The

fundamental drawback of titanium is also its low wear resistance, which is often worse than that of other metallic biomaterials [26]. It might cause the surface to deteriorate, release elements, and accumulate corrosion products, which would result in metallosis [27]. According to Salem et al. [28], Titanium implant components are more likely to cause metallosis than cobalt-chrome implant components. As a result, altering the titanium implants' surface characteristics is still acknowledged as a key means of enhancing biocompatibility [29]. To improve the state of pure titanium, several surface alterations including ion implantation, plasma treatment, and chemical etching, physical vapour deposition (PVD) and atomic layer deposition (ALD) coating deposition methods are being used [26,27,29]. With the pursuit of newer and better solutions, and the increasing availability of laser techniques, this dissertation focuses on the application of coatings and subsequent laser alloying of coatings to produce competitive/better coatings than those already available in medicine.

2.1.3. Gold additives and coupling with Ti

The remedy for the previously described problems with titanium may be the use of a precious element, which is gold. This element has a long history of usage in the jewellery business as a valuable metal. Research has proven the widely held belief that it does not cause allergies when it comes into contact with the human skin and has also demonstrated its great biocompatibility and advantageous characteristics [30,31]. In the last century, gold fillings and denture components were also frequently employed in dental prostheses. Due to their extremely low corrosion rate, they continue to play a significant role in dental prosthetics today [32]. The use of gold as a precious metal seems to be an excellent option that has the potential to considerably increase the utility of titanium in biomedical applications. This is made feasible by the qualities of gold, including its biocompatibility, antibacterial property, lack of toxicity, lack of immunogenicity, and high tolerance without impairing cellular function. Additionally, the use of gold nanoparticles can benefit from their antioxidant properties, which are internalized in the cell nucleus [33–35]. The major drawback of gold from the perspective of mechanical engineering of prosthesis is its high density, $\rho_{Au} = 19.3 \text{ g/cm}^3$, which results in its weight and poor hardness. Although it may reach 81 GPa, the Young Modulus is lower than that of titanium. Other metals have been added to gold alloys as alloying agents to modify the mechanical properties. Palladium (Pd) and platinum (Pt) increase the solidus temperature, while non-precious elements like indium (In) and tin (Sn) are added to improve hardness and modify

the coefficient of thermal expansion of the ceramic components in prostheses. These additives have been and continue to be popular in gold alloys over the years.

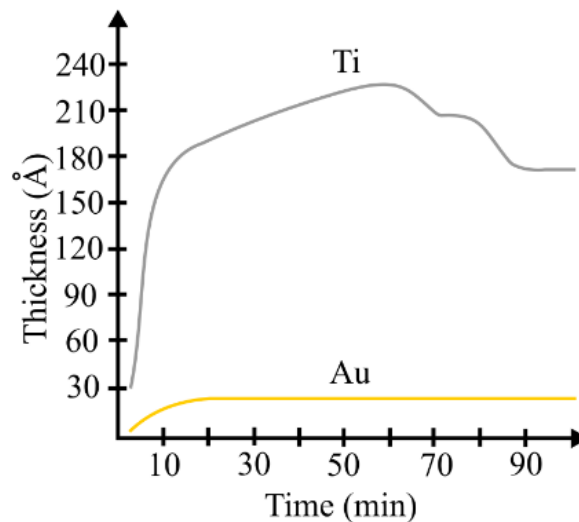


Figure 2. Protein adsorption (biofilm) thickness onto gold and titanium diagram.

Studies conducted by Sundgren et. al. [36] indicated that there is a significant difference between protein adsorption on hydrophilic titanium and hydrophobic gold surfaces (Fig. 2). The primary distinction is that titanium surfaces tend to generate an extended, loosely packed protein layer with a tendency to fluctuate over time, whereas gold surfaces tend to form a narrow, compact protein layer that is consistent with time. The unstable oxide layer of the titanium passivation layer, among others, intensifies this phenomenon [37]. Employing TiAu intermetallics may minimise the impact of artificial materials and blood flow patterns on the clotting system by managing the biofilm layer [36,38]. Furthermore, according to a research by Kodama et al.[39], using intermetallic compounds made of a diamagnetic element like Au and a paramagnetic element like Pt can help reduce artifacts brought on by a disturbed magnetic field close to an imaging target (region) because the metal and the surrounding living tissue have different magnetic susceptibilities [39]. Surface application of coatings comprising these metals may be a less expensive option for applications needing a high magnetic field because the Au-Ti pair is also a diamagnetic and paramagnetic pair (like Au-Pt). Currently, the range of magnetic induction values for Magnetic Resonance Imaging (MRI) in typical practice is from 1.5 to 3.0T; however, a magnetic induction value of > 3.0T is required for accurate imaging of microscopic anatomical structures [40,41]. Stracukova et al. [42] explains that artifacts produced by metallic implants during MRI are attributed to two main factors: 1st. Susceptibility-related artifacts caused by a disrupted magnetic field at the imaging target site

due to a susceptibility discrepancy between the metal and the surrounding live tissue. 2nd. Artifacts caused by the development of a local magnetic field by the electric current created within the metal as a result of the gradient magnetic field and radiofrequency coil pulse operating on the imaging target location. While the first cause is unavoidable, the second can be minimised. Knowing the magnetic induction of living tissues to be -11 to -7ppm, Kodama et al [39] obtained an approach (in Ti-Pt alloy) to a value of -9ppm, which (apart from copper, which however presents tissue toxicity) does not occur for any other known metallic material. This resulted in much less MRI artifacts, particularly under conditions of intense magnetic excitation. Since the Ti-Au pair is also diamagnetic-paramagnetic, it may be predicted that the coatings we create would have a similar set of characteristics but need less raw material. Additionally, the Ti-Au combination satisfies every other material criterion for implants, particularly those relating to non-toxicity, strong corrosion resistance, and high electric conductivity. In order to attempt to produce a material or coating consisting of Ti and Au, it is necessary to trace the phase equilibrium diagram. A studied diagram of the mutual phase ratios and solid solutions gives us the necessary information about the possible molar concentration and the potential phases that can be produced in equilibrium state. A stocktaking of the literature will allow us to answer the question of which phase is of interest in terms of material properties.

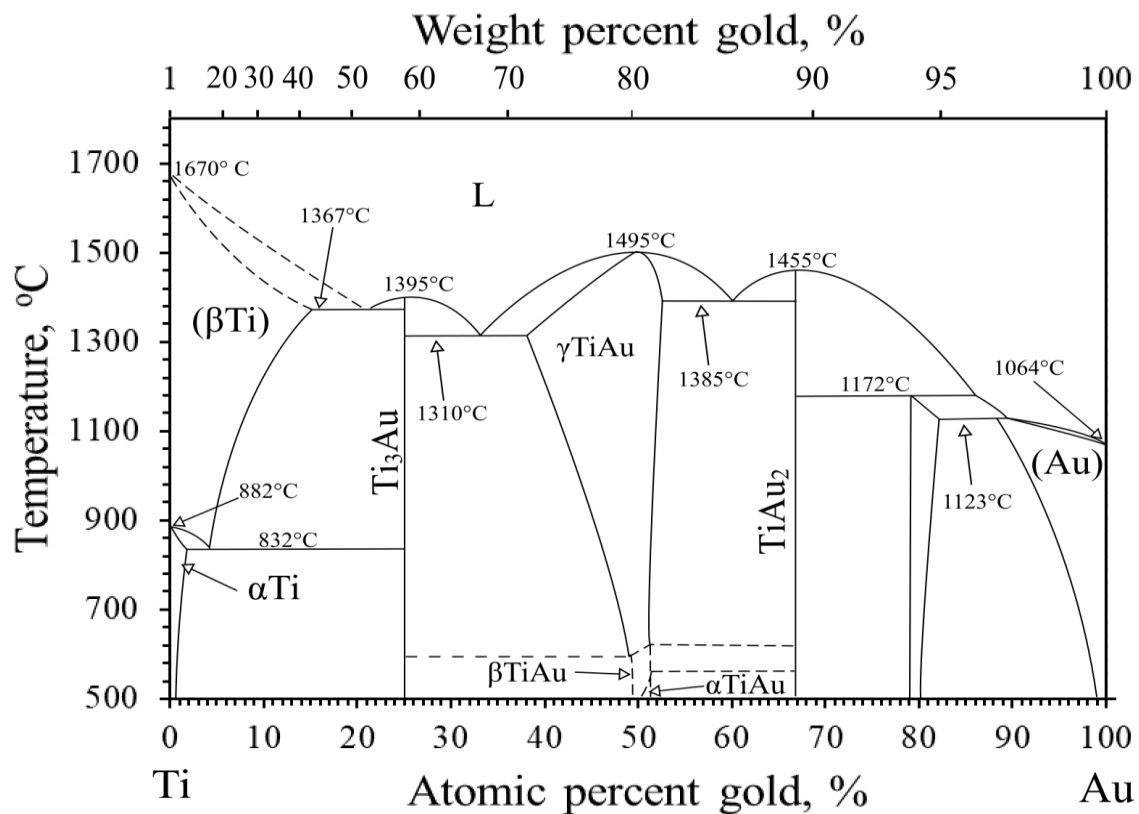


Figure 3. Ti - Au equilibrium diagram scheme [43]

The phase diagram of Ti-Au binary system is presented in Fig. 3. In 2000, Fischer [32] studied a binary alloy of titanium (Ti) and gold (Au) in which Ti acted as an alloying agent at a range of 0-10% by weight. He concluded that a cast alloy with a content of 8% or more Ti was too brittle to be used in prosthetics [32]. 16 years later, Svanidze et al. [31] observed remarkable mechanical qualities in an intermetallic - Ti₃Au composition that were, in their opinion, the result of three factors:

- cubic crystal form with a high (14) coordination of Ti atoms and naturally short Ti-Au bonding.

- high density of valence electrons.

- the development of pseudogaps. In comparison with the two cubic Ti₃Au complexes, the Ti-Au bond length is smaller for the β-phase ($d_{\text{Ti-Au}} = 2.845 \text{ \AA}$) compared to the α-phase ($d_{\text{Ti-Au}} = 2.932 \text{ \AA}$). This prevents dislocation formation and contributes to the high hardness of β-Ti₃Au, which is combined with the more complicated crystallographic environments of Ti and Au. This 4-fold increase in hardness allows β-Ti₃Au to be described as the hardest

biocompatible material known [31]. This indicates a huge potential in Ti-Au system that is still undiscovered.

The models of elementary unit cells of Ti, Au and the most desirable intermetallic between those two elements is presented in the Fig. 4. Models were made using Vesta Software.

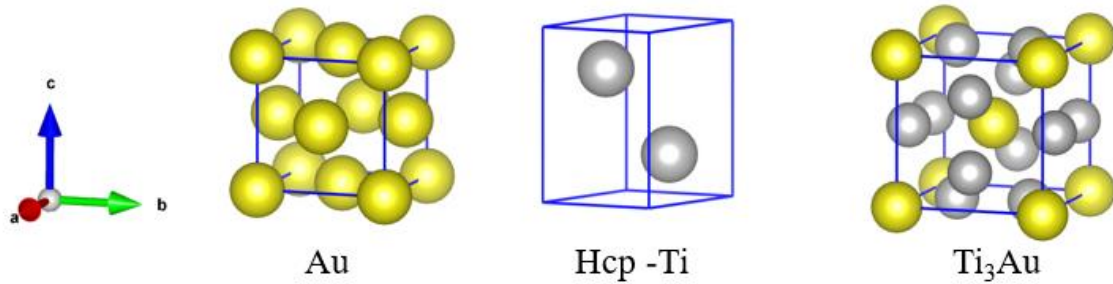


Figure 4. Elemental unit cells of gold, titanium and the most desirable intermetallic Ti₃Au in β – form

The aforementioned literature studies influenced the decision to fabricate Ti and Au intermetallic multilayers for biomedical and anti-corrosion applications using laser assistance. Due to greater control of the passive layer compared to titanium, strong mechanical qualities mentioned in the literature, and yet relatively good economic ratio, suggested coatings have the potential to replace already applied coatings (due to achieving material with a thin gold layer and without platinum).

2.2. Surface engineering in medicine

2.2.1 Surface engineering as key to the tissue-material interface

Designing appropriate surfaces has been a major focus in the design of orthopedic, dental, cardiac, and neural implants over the past decade. This is due to the close link between surface roughness and the effect on the sequence of events occurring in the healing process and the associated 'recovery' of the patient. At the molecular level, roughness affects wettability, which facilitates the initial interaction of the implant surface with proteins and other molecules. This also affects platelet adhesion and the process of thrombogenesis. Porous surfaces prolong the persistence of blood clots at the implant site by physically trapping fibrin particles [20,44–46].

On the other hand, the high mortality rate associated with cardiovascular problems means that a number of devices have become commercially available for assisting the heart and restoring normal coronary vascular function by preventing clots, embolic aneurysms or managing cholesterol deposits. Such applications require a fundamentally different approach at the property design level. Any aforementioned platelet adhesion, activation of the coagulation system or overly effective contact of constantly flowing body fluids with the material is detrimental or even unacceptable.

Since the usability of the implant is primarily determined by the surface in contact with living tissue (100-200 μm into the bone measured from the implant surface), the surface layers of the implant should be the primary focus when designing new materials. Modified surfaces of metallic implants should provide [9,47]:

- durability and functionality of the layer
- high adhesion which excludes the possibility of layer delamination
- homogeneous structure of the entire surface
- thickness small enough not to significantly alter the geometrical features of the object and to maximise phase homogeneity in the case of diffusion coatings
- resistance to sterilisation
- specific physico-chemical and biochemical properties to provide an appropriate microstructure or topography to favour the adsorption of organic compounds (e.g. osteoblasts) resulting in faster osseointegration, i.e. a structural and functional connection between structured, living bone and the surface of the loaded implant.

Despite the rigor of the material, the implantation of a foreign body into the body is not always successful. The term "Bone-Implant Interface (BII)" is a commonly used term that encompasses all phenomena relevant to successful implantation. Bone is a complex, multi-component system that evolves over time and is difficult to estimate due to its continuous remodeling. The phenomena that occur as a result of this are still problematic to determine in vivo. In addition to an appropriate surface structure, a suitable geometry, which manufacturers have been constantly refining over the years, often has a decisive influence on the success of treatment. Additional influences are, of course, individual variability (bone quality, lifestyle), as well as complications resulting from the actions of the staff (e.g. aseptic surgical conditions) or the correct fixation of the implant in the implant bed. Both too tight and too loose implant insertion

can produce unfavourable results. It is assumed that the optimum bone-to-implant contact ratio (BIC) should be between 60% and 99%. This is important for the secondary stability of the implant (after remodelling), i.e. several weeks to several months after surgery [8,48,49].

When focusing on modifications to the surface layers of metallic biomedical materials, particular attention should be paid to material degradation in the form of corrosion damage, which effectively causes a decrease in functional properties. The decrease in properties is caused by the impact of the environment on the surface layer of the implant, which is the tissue-implant contact surface. Damage to the coating, according to well-defined corrosion mechanisms, can lead to the release of metal ions from the prosthesis into the surrounding tissues and bloodstream, causing metallosis, a disease entity that is one of the complications observed in patients treated for osseoarthritis with endoprosthesis [11].

The effect of metal ions entering the bloodstream is toxic to the surrounding tissues and leads to numerous inflammatory and allergic reactions or, in the worst cases, necrosis. These conditions, if left untreated, can lead to serious complications and even the need to amputate the limb. The relationship between the concentration of a chemical element and the response of neighbouring tissues can be described using a curve (Fig. 5) analogous to the model curve used in human toxicology, which shows the determination of the LC_{50} as an empirical estimate of the dose causing the death of 50% of the cells in the population under study [11,50,51].

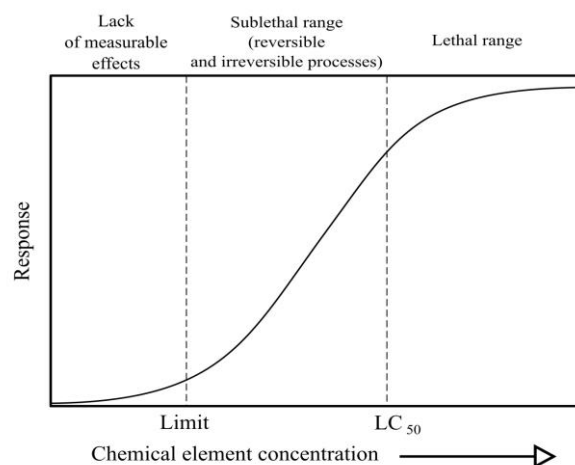


Figure 5. Relationship between tissue reaction and the concentration of a chemical element diagram [50]

Surface modification of metallic biomedical materials is performed by a variety of methods, each of which produces slightly different properties of the final surface.

Manufacturers of many current implants for medical applications use combinations of the methods described below to produce a specific structure. This is the result of many years of research into the effects of micro- and submicro-structure on the response of bone tissue both during primary and secondary remodelling in the implant locus. The types of surface treatment used often results in a structure with the appropriate roughness. The first authors to clearly describe the differences in smooth ($S_a < 0.5 \mu\text{m}$), minimally rough ($S_a = 0.5 - 1 \mu\text{m}$), moderately rough ($S_a = 1 - 2 \mu\text{m}$) and rough ($S_a > 2 \mu\text{m}$) surfaces were Wennerberg & Albrektsson [49]. The S_a defined as a roughness measured as the average deviation in height from the surface. These studies suggest a predominance of roughness defined as medium, but the selection of the most favourable roughness depends on a number of factors, hence a whole cross-section of roughness, types of machining and implant systems used are used in manufacturing practice. Examples of manufacturers and the types of machining they use are shown in the Table 1 below [8,23,48,49,52].

Table 1. The Implant manufacturers and used surface treatment [52]

Manufacturer	Implantation system	Commercial name of the surface	Surface treatment	Processing abbreviation
Straumann	BL	SLA®	Surface treatment Coarse sandblasting + etching	SB + AE
Microdent	Genius	ATEC®	Aluminum oxide sandblasting	SB (Al ₂ O ₃)
Dentsply-Sirona	Astra Tech	OsseoSpeed®	Titanium oxide sandblasting + fluoride addition	SB(TiO ₂) + F
Avinent	OCEAN®	Biomimetic®	Sandblasting + Implantation of Ca and Phosphor ions	SB + Ca + P
Zimmer Biomet	Biomet 3i	Osseotite®	Double etching	2AE

Klockner	Vega®	Vega®	Aluminum oxide sandblasting + thermal-chemical treatment	SB (Al ₂ O ₃) + TCT
Ticare	inHex®	RBM TC®	Sandblasting with resorbable particles + double etching	SB (res) + 2AE
Nobel Biocare	NobelReplace®	TiUnite®	Titanium oxide coating	TiO ₂
Galimplant	IPX®	Nanoblast®	Sandblasting + triple etching in an acidic environment	SB+3AE

At the stage of designing the surface layer and selecting the appropriate treatment, it is useful to determine which property improvements will be most desirable. The most important directions for improving properties are given in the Fig. 6 below:



Figure 6. The Surface modification for the implant – bone relations [44]

2.2.2 Selected methods for modifying surface layers

The main methods of physico-chemically modifying the surface layers that are used in manufacturing practice are based on well-known operations from other areas of materials engineering, and when modified appropriately, they are successfully applied. The most important of these are [9,13,44,53–55]:

Abrasive grinding - Grinding with an abrasive of varying grit size. It makes it possible to vary the degree of roughness, but because of the impurities introduced by the abrasive, this method requires a further treatment stage to clean the actual surface. Grinding media of different gradations, i.e. with abrasive grains of different sizes in their matrix, are used.

Shot blasting, sandblasting - High-pressure spraying of Al_2O_3 , TiO_2 or hydroxyapatite grains/particles to produce a porous structure of material usually 10 - 100 μm . This procedure develops the contact surface with the tissue, which promotes faster integration of the deposited cells. The grains collide with the surface, imparting a set amount of kinetic energy to it. This

energy is absorbed by the crystal lattice, causing an increase in the number of lattice defects and surface melting of the material. The defect structure and melting of the material depend on the kinetic energy of the grains [56].

Electrolytic polishing, anodic oxidation - Machining methods that can follow abrasive grinding or blasting to produce a micron (or in some cases even nanoscale) structure. It is the anodic dissolution of metals by means of an applied electrical voltage. A part of the electrical charge is deposited on the surface roughness elevations, which smooths out the irregularities. Electrolytic polishing produces a deformation-free surface without disturbing the crystal structure. The obtained effects increase with increasing homogeneity of the alloy.

Acid etching - A similar effect to anodic oxidation can be achieved by etching the surface layer structure with acid. The less homogeneous the structure, the more effective this process is - different phases dissolve at different rates. Depending on the material to be etched, different reagents and their mixtures are used to carry out the etching. It is also possible to control the etching time and temperature of the process. The most commonly used acids for this type of treatment are: HNO₃, HF, HCl, H₂SO₄, H₃PO₄ [55].

Alkaline etching - Similar to acid etching, alkaline etching is a simple technique for modifying the surface of a material by immersion. The main difference lies in the medium used, a highly concentrated base. Most commonly, concentrated NaOH is used for Lugging. Analogous to pickling, the essential parameters for leaching are the time (often in the order of 24 hours) and the process temperature (in the order of 600°C) . In the case of leaching of titanium alloys, a 1µm-thick Na-Ti gel layer with an irregular structure and open extensive pores can be produced.

Passivation - After etching, anodic oxidation, or through spontaneous processes, a passive layer of oxides or salts forms on the metal surface due to contact with oxygen or another oxidizing gas. For titanium alloys, the resulting passive layer is tight and well bonded to the substrate (high adhesion). The response from tissues at the implant site may vary depending on the chemical composition and alloying elements present. Such responses are summarised in Tab 2 [19,57]

Table 2. Properties of oxides of elements formed on titanium alloys [13]

Element	Most stable oxide	Isoelectric point pH(I)	Solubility at pH 7, [mol/L]	Tissue response

Ti	TiO ₂	3,5 ÷ 6,7	3×10^{-6}	inert
Al	Al ₂ O ₃	8,8 ÷ 69,5	10^{-6}	encystment
Nb	Nb ₂ O ₅	3,4 ÷ 3,8	$\sim 10^{-5}$	inert
V	V ₂ O ₅	1,5 ÷ 2,3	> 1	toxic
Zr	ZrO ₅	10,0 ÷ 11,0	$< 10^{-6}$	inert
Ta	Ta ₂ O ₅	2,7 ÷ 3,0	$\sim 10^{-5}$	inert
Fe	Fe ₂ O ₃	2,2 ÷ 9,0	$< 10^{-6}$	encystment

Pulsed laser deposition and ablation - In this method of surface modification, a laser with pulsed light beam emission is often used because of its ability to achieve high energy density and its ability to achieve ablation, i.e. a state in which the high-energy quanta of the laser radiation are capable of lowering the energy of the bonds between the particles, which consequently makes it possible to remove atoms layer by layer. Pulsed laser deposition (PLD) allows a highly focused, impinging beam of light to be incident on successive areas of the material to be vaporised (target), leading to absorption of the beam energy by the exposed atoms and their vaporisation (ablation). The vaporised atoms are then deposited on the material to be modified (substrate) as a result of the interaction with the laser. This process usually takes place in vacuum because of the need to minimise collisions of air atoms with the atoms of the material being excited (Fig. 7).

This procedure makes it possible to obtain homogeneous single- or multi-layer coatings with good adhesion to the substrate and even nanometric structures. The technique allows the deposition of both borides, carbides, nitrides and their compositions, as well as organic coatings (conductive polymers) or hydroxyapatite layers and almost all allotropic carbon varieties (from diamond to fullerenes).

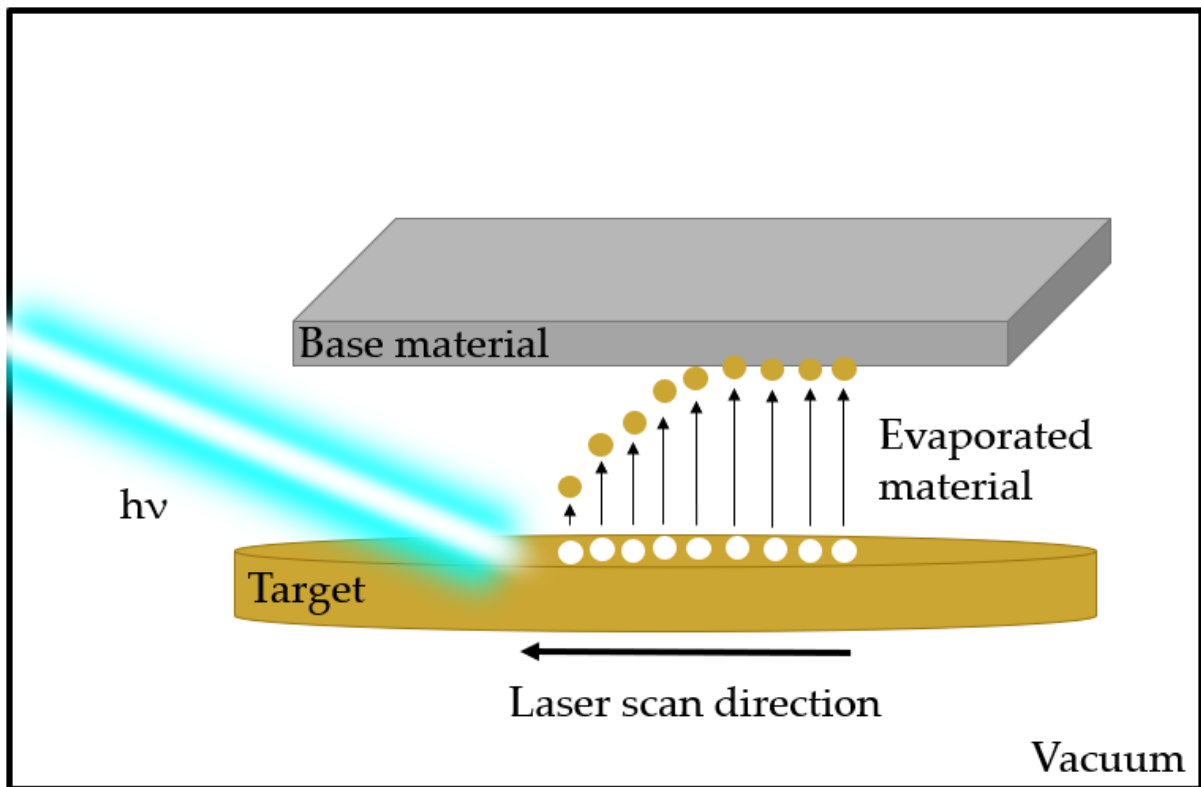


Figure 7. Schematic diagram of laser ablation deposition [54]

PLD can essentially be regarded as one variation of a very diverse group of methods that put elemental ions into a gaseous state:

Physical Vapour Deposition (PVD) of atoms by physical methods in vacuum. All vapour deposition technologies consist of three stages [44,54]:

- evaporation of the target (deposited) material
- transfer of evaporated target material to the surface of the sample (target material)
- deposition of target atoms on the surface - sputtering.

The criterion that distinguishes these methods is how the target material is excited. The most well-known methods are: electron, arc, resistive, inductive, and laser excitation (as previously mentioned).

Due to the large number of methods described in the literature under different names, it is difficult to classify them unambiguously. Despite the abundant variety, only a few methods have found application in the production of medical implants. For the most part, PVD methods

are used to produce coatings characterised by high hardness and tribological resistance, where wear, friction and lubrication properties are the main focus of analysis.

Materials designed for enhanced tribological properties can be divided into:

- hard-coated materials
- solid lubricants

The solid state of the materials means that they can provide lubricating properties in two ways [54]:

- 1) As a result of their high hardness, mainly used to protect surfaces against abrasive and/or erosive wear. It is also possible to use materials with high hardness as diffusion barriers, insulators or thermal conductors, e.g. diamond in electronics
- 2) As a result of a suitable crystalline structure having an easy slip plane, e.g. graphite, or weak interplanar bonds that allow absorption of foreign molecules and consequently easy slip, e.g. MoS₂. Such materials are typically characterised by a hexagonal structure.

LSTO (Laser Surface Texturing Oxidation) - Laser surface texturing oxidation is a widely used technique for improving material properties associated with changes in both roughness and phase composition of the material surface layer. LSTO is a fast and clean process. The absence of the need for large quantities of electrolytes and long heating and cooling times as in conventional annealing of titanium alloys makes laser oxidation environmentally friendly. Laser texturing allows selective processing of the surface layer material by directing the laser beam along a pre-designed path (pattern). This leads to improved wear resistance and the development of the surface (Fig. 8), enables a change in the surface energy of the surface layer being processed. Thanks to the concentrated energy and high density of the laser beam, in addition to vaporising part of the material (ablation), it is possible to carry out laser alloying, i.e. to cause a change in phase composition by producing intermetallic substances [24,58]. All the phenomena produced by the concentrated laser beam also (or even primarily) allow a change in the wetting angle, which is decisive for the designation of a surface as either hydrophobic or hydrophilic [59]. The phenomenon of hydrophobicity and superhydrophobicity itself is used extensively in technology in the production of modern smart materials with 'self-cleaning' potential. The discovery of the hydro-, lipo- or oleophobic potential was prompted by observations of nature, hence the name 'Lotus Effect'. A surface showing a wetting angle >150° is considered superhydrophobic [14,59–61]. Hydrophilicity, on the other hand, is used in

moving machinery equipment to maximise the retention of lubricating substances on its surface that reduce friction and thus extend the life cycle of the component by reducing the coefficient of friction. The texture itself can act as a kind of lubricant reservoir in this application [62].

It is the wetting angle that will determine the inhibition of microbial colonisation, and the type of microbes. Depending on the intended use of the material, the expected value of the wetting angle may range from hydrophilic (favoring osseointegration, better bone-implant contact rate, and osteoblast differentiation) to superhydrophobic (reducing platelet adhesion, resistance to blood flow, activation of the coagulation system, and the risk of embolism). Both of these phenomena in their environment are very important and have a significant impact on implant usability [14,59,60,63,64].

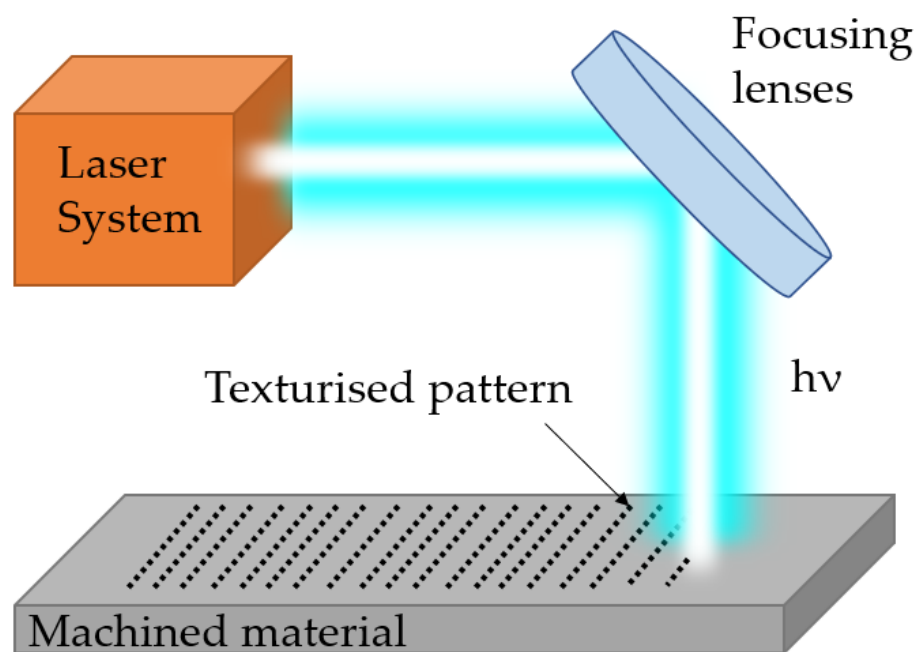


Figure 8. LSTO process scheme.

IBAD (Ion Beam Assisted Deposition) a dual-beam deposition method from the PVD family of methods, the development of which in recent years has ensured that layers composed of several elements can be deposited with good adhesion to the substrate and the presence of a wide interlayer giving the coating a high degree of deformability [65]

Plasma spraying - Temperatures on the order of 10,000°C make it possible to spray a layer of hydroxyapatite with particle sizes on the order of nanocrystals. The method is also used to apply

compounds such as Al_2O_3 or ZrO_2 . The plasma is generated by an arc discharge between a pure tungsten electrode (the cathode) and a water-cooled copper nozzle acting as the anode. In the case of fluorescent methods, an ionised reactive gas with a high concentration of charged particles is used, obtained by passing a current through the gases.

The layers produced by fluorescent techniques (nitriding and fluorescent oxidation), allow the formation of multiphase layers on the titanium surface, which are resistant to corrosion and tribological effects and provide a good barrier against metallosis. In vivo studies showed high cell proliferation and reduced peri-implant capsule area. The absence of alloy components in the surrounding tissues demonstrates the high biocompatibility of the coating. An unquestionable advantage of the above methods is the high control over process parameters, which enables the production of layers with the desired chemical and phase composition, as well as the appropriate topography and microstructure [66].

Ion Implantation - The main advantage of ion implantation technology is the idea of implanting any material, non-metallic or metallic, with any components, solids or gas ions. In addition, the implanted material can be a material with a previously produced coating, or without any coating (most applications). The general principle of ion implantation is based on the incorporation of a foreign atom into a solid by acquiring sufficient kinetic energy (obtained in a strong electric field). The ion initially causes ionisation of the substrate and exchanges electrons with it. Subsequent collisions in the solid are elastic in nature. It is important that the energy of the ions bombarding the implanted surface is chosen so that the implantation process outweighs the ion etching process. With this method, hard and corrosion-resistant coatings can be obtained with little consumption of protective material. [44,47,67].

Sol-gel method - The sol-gel method can be used for the constitution of single- and multi-component and multilayer coatings. The oxide coating formed during the process is characterised by a variety of chemical compositions and microstructures, typically reaching a thickness of approximately 1 μm . Furthermore, one of the advantages of the sol-gel method is that hydroxyapatite can be produced directly on the deposited surfaces through interaction with physiological fluids. The surface after the sol-gel method is rich in ZrO_2 oxides, occurring in three crystallographic varieties, of which the high-temperature configuration has the best properties. The improved mechanical properties provide, high hardness, high bending strength and resistance to fracture. In addition, the coating has significant corrosion resistance, which provides satisfactory biocompatibility [6,68–71].

ALD (Atomic layer deposition) - An atomic layer deposition process is a type of chemical vapour deposition (CVD) technique. CVD techniques involve creating conditions in which a coating layer forms on the surface of a material as a result of the decomposition of chemicals in the gas phase. This process is usually thermally activated, but photon (light) or plasma excitation methods are also often used. The constitution of the coating is controlled by a chemical reaction, which fundamentally distinguishes the CVD method from the previously described PVD techniques. The growth of the film is controllable by a non-equilibrium precursor concentration, which is used as an indicator of the dynamics of the CVD process. The advantage of this approach is that it can be developed both at the laboratory scale and for high-volume material production. This is favoured by the prospect of achieving a very high degree of reproducibility [24,44,67].

When shaping the surface of metallic biomedical materials, the electromagnetic properties of the body must not be neglected. Tissues are electrically conductive centres, influencing the propagation of action potentials in the body and the proper functioning of electrically sensitive components of the body (nervous system, blood components, muscles). Introducing a substance with ferromagnetic properties into such a structure can significantly disrupt the functioning of the above-mentioned elements, causing clots, disruption of the transport of biological mass, disruption of bone growth and all the associated biomechanical consequences [19].

Particular attention should be paid to the electrode potential of the implanted metal or coating, which will act as protection, due to the initiation of thrombosis in particular. Covering the implant with a dielectric coating or a paramagnet with a high specific resistance will contribute greatly to increasing biotolerance. In addition to bioelectronic phenomena, this should also include a reduction in sensitisation and toxicity, as confirmed by numerous empirical studies. Taking into account all the constraints and surface layer fabrication options considered in this chapter, an attempt can be made to select the most optimal method for producing biomedical implants, depending on the application [13,19].

2.3 Laser impact on the solid matter

2.3.1 Physical basis of the laser impact on the solid matter

A laser is a source (generator) of radiation. It transforms the supplied energy - into electromagnetic wave energy using the radiation amplification effect in the laser active medium and resonator feedback. The radiation amplification effect is conditioned by the phenomenon of forced emission caused by occupancy inversion. In a dynamic equilibrium environment emission is described by Boltzmann equation (1)

$$\frac{N_g}{N_d} = \exp\left(\frac{E_g - E_d}{kT}\right) = \exp\left(-\frac{h\nu}{kT}\right) \quad (1)$$

where: N_g, N_d - level occupancy (concentration) E_g, E_d, k - Boltzman's constant ($k = 1.38 \times 10^{-23}$ J.s), T - temperature

Because of the abovementioned statement, the ratio N_g/N_d is always smaller than unity for $E_g > E_d$, and as a result, the occupancy of the state decreases with increasing energy. The situation is inverted in a system with occupancy inversion: the higher state's atom concentration is greater than the lower state's atom concentration. Accordingly, the mechanism in the laser's active medium with an occupancy inversion produced between the E_g and E_d levels is as follows: when radiation with a resonance frequency of $\Delta E/h$ enters this medium, forced emission and absorption processes occur simultaneously. However, the number of forced emission and absorption actions is proportional to the concentration of atoms in the upper E_g and lower E_d states, respectively, even if the probability of both events is equal. Therefore, the number of forced emission acts surpasses the number of absorption acts in a system with inversion of occupancies where $N_g > N_d$, and as a result, the resulting active medium has an amplifying effect. The situation is exactly the reverse in an excited medium with a Boltzman distribution of occupancies; absorption overcomes forced emission, and the resulting medium absorbs radiation.

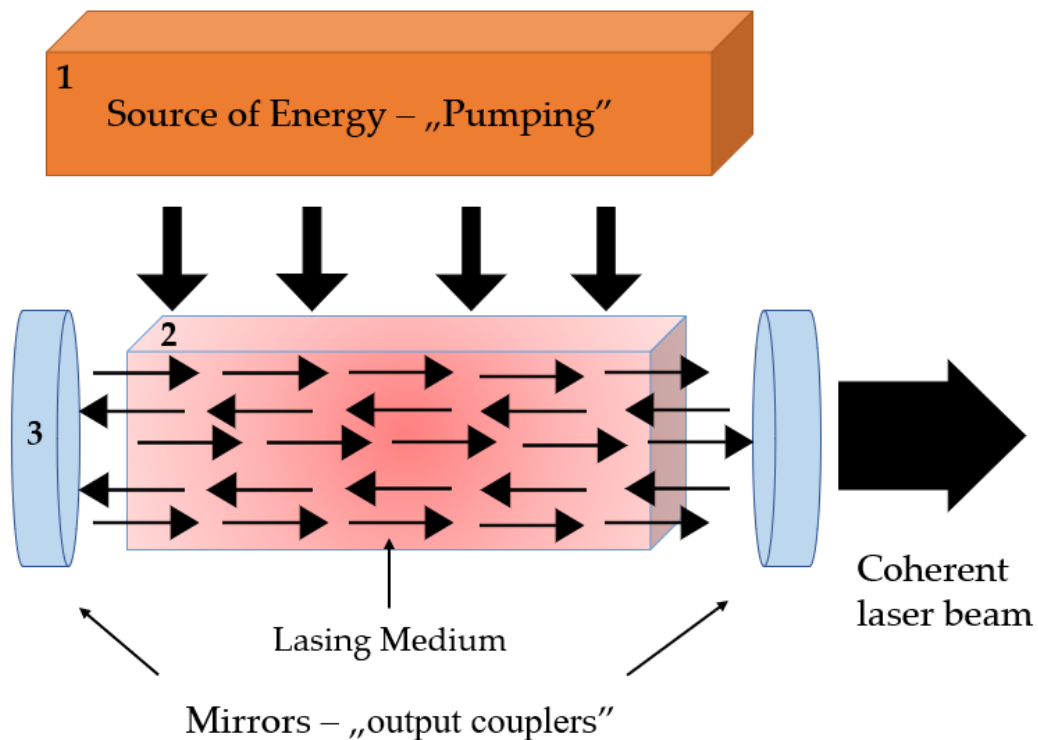


Figure 9. Schematic diagram of laser beam formation.

The three main parts of a laser (Fig. 9) are as follows [72]:

1. A source of energy, often known as a "pump," that can be a chemical reaction, flash bulb, electric current or discharge, or another laser's light.
2. A lasing (or gain) medium, which may be a solid (such as crystals, glasses, or semiconductors), a liquid (such as organic solvents and dyes; "dye lasers"), or a gas. The lasing medium, which is also the primary determinant of the kind of pump used and the wavelength of the generated laser light, is often termed after the kind of laser.
3. An optical resonator, also known as an "output coupler," is a device that, in its most basic form, consists of two parallel mirrors that are both highly reflecting and partially reflective.

2.3.2 Laser melting and alloying

During laser processing, several types of the laser beam impact on solid matter can be distinguished, such as remelting, alloying, fusion, or surfacing. Depending on the parameters effect of the processing it can produce the plasma that is created as the substance evaporates and the surface layer is melted by the laser. While actively engaging with the surface of the liquid material pool by pressurising and stirring the molten material, the plasma protects the surface from further laser heating. A funnel-shaped cavity is created in the pond at the laser beam penetration point, where the hydrostatic pressure of the liquid on the molten material side and the vapour pressure on the beam side impinge on its surface. The ongoing upheaval of this dynamic equilibrium is caused, among other things, by the relative movement of the laser beam and the workpiece. As a result, the cavity moves relative to the melted material in the opposite direction [72,73].

Laser alloying is made by simultaneously melting the substrate and alloying material with a laser beam while rapidly mixing them in a liquid pool, this process is known as laser melting. Depending on how the alloying agent is added to the pool, remelting and melting are distinguished from one another. The alloying process consists of applying an alloying material to a substrate and subsequently melting it together with the surface layer of the substrate material. Painting, coating with adhered pastes or powders (of saturating metals, boron carbides, tungsten carbides, with powdered ferroalloys or titanium), thermal spraying (flame, detonation, plasma spraying), vapour deposition (PVD, CVD), electrolytic deposition, spraying with suspensions, and application of thin films, plates, rods, or wires are all methods used to apply the alloying material to the substrate material. A very thin diffusion zone of 10 μm thickness forms at the solid-liquid interface after cooling when a tiny layer of solid clinging to the material of the pool melts due to heat transfer from the bath, However, in some cases, alloying elements can diffuse to a depth of as much as 200–300 μm . One or more passes of the laser beam are used to do the alloying [54,74,75].

For laser processing of e.g., TiAu, convection plays a major role (due to the high speed of the process, mass exchange is not possible through e.g. diffusion). Convection is the most important factor affecting the pool geometry, including its shape, undercutting and rippling, and can cause defects such as variable penetration, porosity and lack of fusion. Convection is also the main

factor responsible for mixing and hence affects the composition of the melted pool [75]. The schematic of how convection moves inside the melting pool area is presented in the Fig. 10.

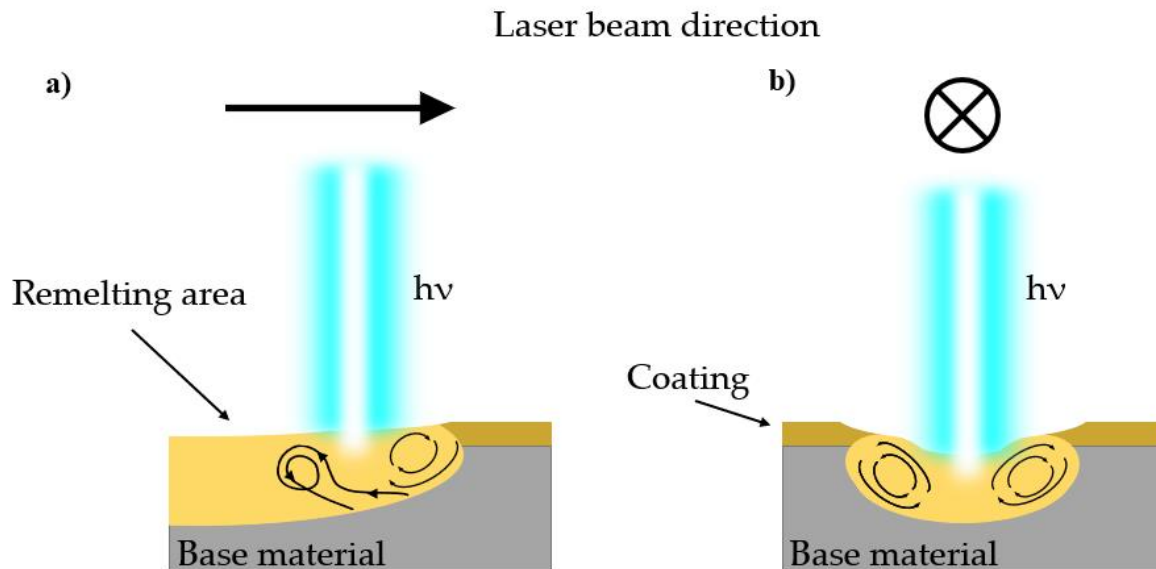


Figure 10. Convection schematic during laser process a) side view, b) front view [76]

After irradiation with the laser beam is completed, the material in the alloy layer solidifies, and the substrate material nearby hardens. The structure, chemical composition, and physicochemical characteristics of this layer are distinct from those of the substrate and the alloying substance.

3. Aim and thesis of the work

The issue of the Ti-Au laser modified system potential for biomedical devices have not yet been fully characterized, the presented literature review shows that a deeper analysis of the use of one of the most biocompatible metals - gold - in the treatment of medical problems. Its unique properties enable for the use of gold in numerous applications as biomaterials in the form of layers, particles and nanomaterials. This is possible due to biocompatibility, non-toxicity, non-immunogenicity, high tolerance without slowing down cellular function. Following the discovery in recent years of a very promising combination of gold and titanium for orthopaedic medicine (Ti_3Au phase to be the hardest metallic compound ever made for

biomedical application) [31] it can be concluded that its full potential has not yet been used. Taking into account increased corrosion resistance [33] of Ti-Au composition in comparison to conventionally used pure titanium and other unique properties of gold (such as prospective ability to control clotting [36]), efforts devoted to the development of laser micro-processing technology seem justified and may lead to increase the so-called percentage time to event release in post-operative cases. The justification diagram is presented in Figure 11.

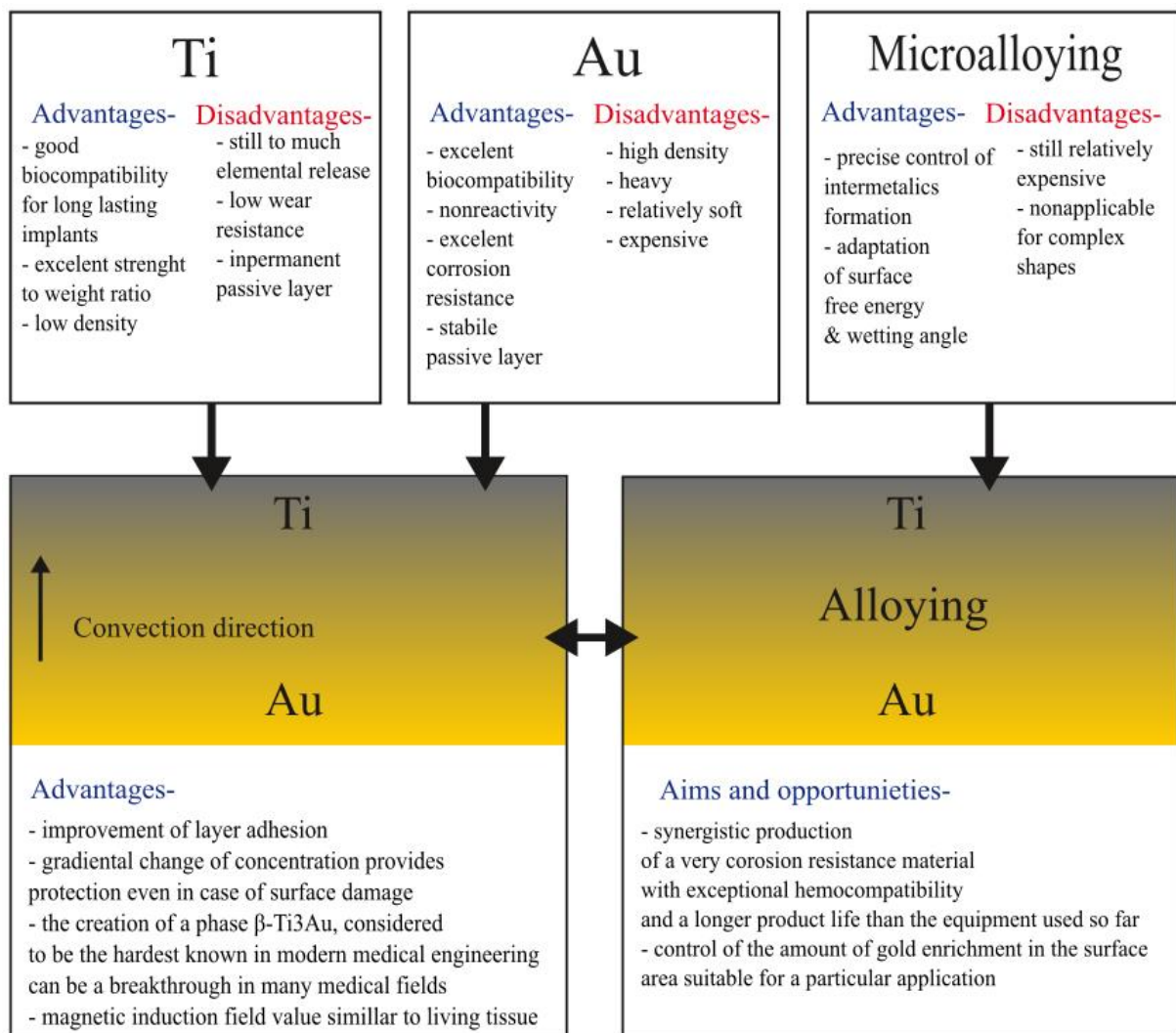


Figure 11. Justification of research diagram

It is anticipated that by determining the impact of the gold-titanium layers made by hybrid treatments consisting of coating application and laser intermetallics formation it is possible to shape and prolong the usage of implanted medical devices and thus improve their so-called

biocompatibility. These issues have not yet been characterized in the subject literature and should be analysed for modern blood contact materials (i.e., housing of Ventricular assist devices (VADs), dacron valves rings, Total Artificial Heart (TAH), aneurysms clips, middle ear prostheses used in stapedotomy, endoprosthesis and many more.

Pioneering nature of the dissertation

The Pioneering nature of the following dissertation consist of the use of modern technique of laser microalloying of the material (Ti and its modern medically used alloy Ti13Zr13Nb) covered by thin electrochemical coating (Au). Gold-enriched titanium surface layers have the potential to perform better than those used in current medical sciences that only contain titanium materials alloyed with Al and V or Zr and Nb throughout their volume, which are in the same comparative group (properties improvers). Additionally, there is a lack of systematized knowledge about the performance of the TiAu system during protein adhesion tests and cytotoxicity assessment, which are basic methods in the early-stage assessment of materials intended for use in a continuous blood flow environment and inside the human body. There is also a lack of studies in the publicly available literature on MRI imaging and the artifacts caused by the presence of such materials (the available studies on the Ti-Pt system are very promising and the Ti-Au pair would be economically preferable). Moreover, there is a lack of detailed research on promising laser alloying of Gold coating on Titanium having a potential for increasing layers adhesion. Therefore, scientific efforts should be made to clarify the TiAu intermetallics composition as the complex interactions between the blood flow and potential clotting system activation. In particular, the following fundamental scientific and research issues still need to be resolved:

- **Characteristics of the conditions necessary for the electrochemical deposition of gold on titanium and its alloys**, so far in industry the common method with nickel interlayer between Ti and Au was seated to make the adhesive strength acceptable [77],

- **Characteristics of the influence of laser alloying on the surface phenomena within the surface layer**, the laser parameters and characteristics should be suited very carefully because of the tendency of Gold to evaporate from the surface instead of being alloyed

- **Characteristics of the obtained materials under the mechanical point of view**, surface conditions of the biomaterial are critical for the destination point of view (body fluids are hostile for materials)

- **Characteristics of the biological response during *in vitro* study**, critical value should be the cytotoxicity and protein adsorption/adhesion during blood flow.

By identifying and solving these problems, the thesis of the following dissertation was: **It is possible, through the application of a hybrid processes of electrochemical deposition and laser microalloying, to produce a multicomponent surface layer on Ti and Ti-based alloys, enriched in gold, which will possess improved functional properties due to the presence of Ti₃Au phase**

4. Experimental section

4.1 Research methodology

4.1.1 Research plan

The research plan includes the use of Ti and Ti₁₃Zr₁₃Nb as the base material. A layer of gold with a thickness of about 2 μm will be applied to the properly prepared surface of each base material in an electrochemical process. The specific details of this process, such as the type of electrolyte and the current density, will need to be determined and optimized to achieve a uniform and adherent gold coating.

After the gold coating has been applied, the coated materials will undergo laser alloying using a series of parameters. The specific parameters and the laser alloying process itself will need to be carefully chosen and controlled to achieve the desired microstructure and properties in the final materials.

The laser processing schemes that will produce materials with the best properties will be selected for further and more detailed analysis. This analysis will include a variety of methods, such as numerical analysis, light microscopy, scanning electron microscopy (SEM), transmission electron microscopy (TEM), energy dispersive spectroscopy (EDS), electron backscatter diffraction (EBSD), X-ray diffraction (XRD), wettability, corrosion resistance, tribological, cytotoxicity, and nanohardness testing.

The results of these tests will be used to compare the properties and performance of the coated and uncoated materials and to understand the effect of the gold coating and laser alloying on the microstructure and properties of the materials.

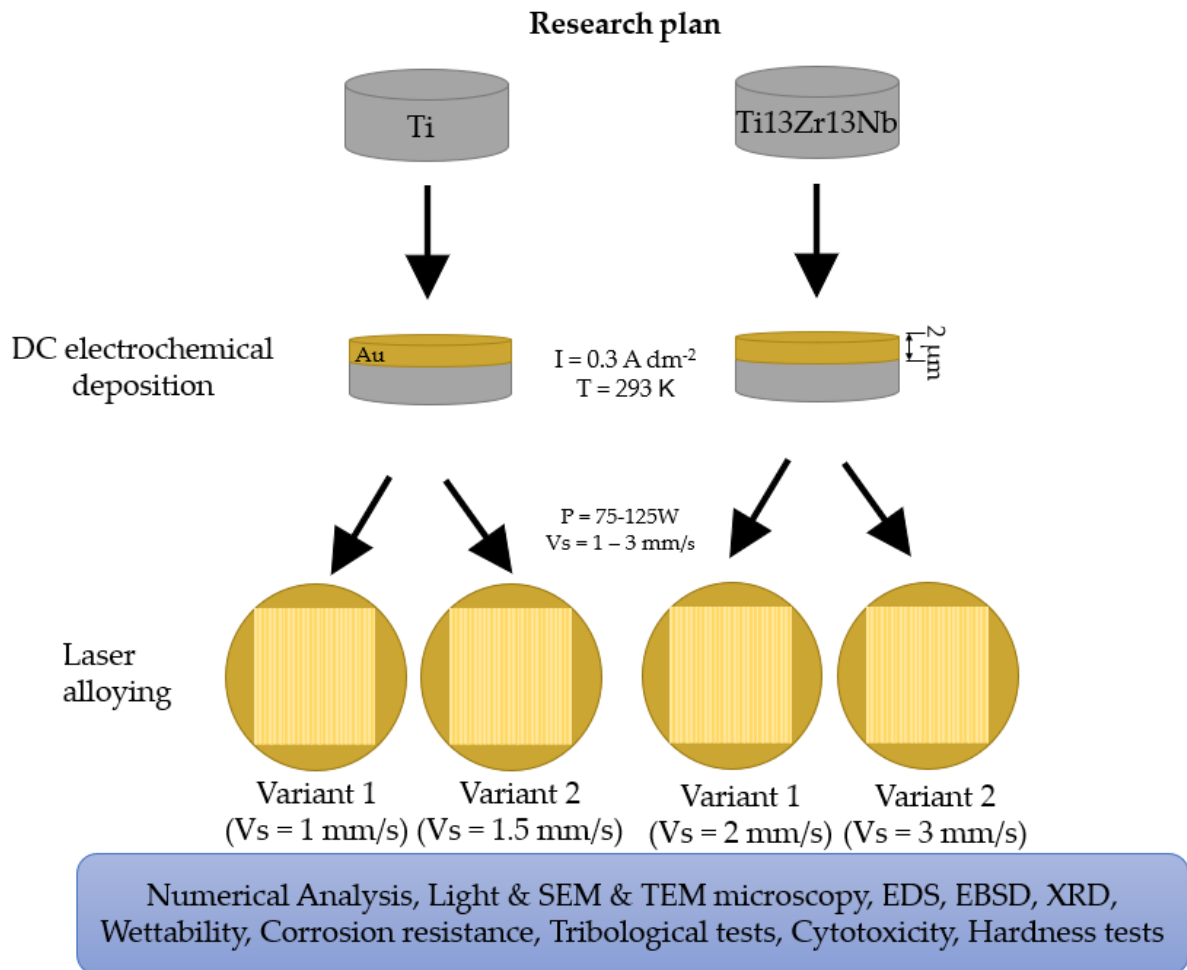


Figure 12. Research plan

4.1.2 Materials

Samples from commercially pure Titanium Grade II (CP Ti), were delivered as $\varnothing 30\text{mm}$ rods (Wolften, Wrocław, Poland), cut into slices on a lathe. The material is characterized by the ASTM B348/B348M standard, with the chemical composition presented in Table 3.

Table 3. Chemical composition of pure titanium grade II used in experiment [78,79]

Elem.	Ti	Fe	O	C	N	H
Wt. %	99.65	0.02	0.18	0.10	0.0096	0.0290

Ti13Zr13Nb samples, were delivered as \varnothing 40mm rod (BimoTech, Wrocław, Poland), cut into slices on a lathe. The chemical composition is presented in Table 4 [80].

Table 4. Chemical composition of Ti13Zr13Nb used in experiment

Elem.	Ti	Zr	Nb	Fe	C	N	O
Wt. %	Balance	13.0	13.0	0.05	0.04	0.019	0.11

The rods were cut into 7 mm thick slices and prepared for electrodeposition. Each sliced sample was prepared according to metallographic procedure: grinding with paper grain size gradation sequentially 220, 800, 1200 in time $t = 4$ min per gradient and mechanical polished using 0.04 μm colloidal silica. The process was performed using the grinding-polishing machine TERGAMIN-30 (Struers, Willich, Germany).

4.1.3 Coating application

Suitably prepared - polished, washed and degreased titanium samples were etched in boiling hydrochloric acid (HCl) solution (50% v/v). Immediately prior to the gold plating process, the etched samples were cathodic polarised for 10 minutes in a 1 mol solution of sulphuric acid (H₂SO₄), in order to completely reduce the titanium oxide present on the sample surface. The gilding process was carried out using a direct current of 0.3 A dm⁻² in a commercial electroplating bath using the KIKUSUI PWR 800H (Kikusui, Yokohama, Japan). Based on literature reports, the thickness of the desired gold layer was set to around 2 μm and a roughness of no more than around 1.04 μm (the samples were polished to a mirror finish before the etching process), as a value identical to the natural vessel of the vessel's wiener [81]. Process scheme is presented in Fig. 13.

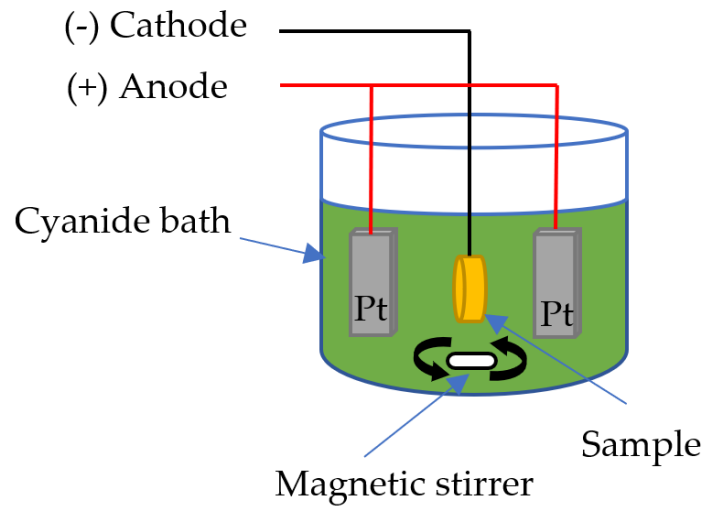


Figure 13. DC electrochemical deposition process scheme.

4.1.4 Laser alloying

The samples were laser processed using the parameters presented in Tab. 5. Alloying was carried out along the line. The experiment was accomplished using Trumph TruDisk 3302 (Trumph, Ditzingen, Germany) based on 1030 nm wavelength continuous laser. Device is powered by neodymium-doped yttrium aluminum garnet; Nd: $Y_3Al_5O_{12}$. The shape of the laser beam was flat-top. The system provided energy that allowed remelting of the material. The maximum energy for the laser acquired was 3.3 kW. The experiments were conducted in an atmosphere of the protective gas – Argon, Ar. In order to obtain a uniformly remelted layer (which requires the melting of both components with different melting points, respectively 1668°C for Ti and 1064°C for Au) with a thickness not exceeding 10 μm , it was planned to use a defocused beam, as suggested by the research carried out by T. Kunimine [82]. The use of a defocused beam changes the heat distribution, and thus also modifies the changes in the microstructure and kinetics of phase transitions. Defocusing makes the sample heat up slower, over a larger area and does not penetrate as deeply as if it were in focus. The use of the variant that delivers the same amount of energy but with the beam in focus (applying lower beam power at a higher photon source feed rate) leads to deeper melting (decrease in near-surface gold concentration) and affect phase formation by increasing the process speed and thus the kinetics of phase formation. During parameter selection, the thickness of one laser line was assessed

and a line-by-line scanning overlap (effective remelting will be selected, covering the heat affected zone where no remelting has been recorded, in order to maximise material surface homogeneity across the cross-section). The fact that convection in crystalline solids characterised by compact space filling is impeded and occurs exclusively in the remelting pool will allow the formation of an Au phases at the desired (controlled by parameters and defocusing of the beam) depth, where at the contact surface with body fluids (blood) the film composition will tend to have higher Au concentration and as one penetrates into the core of the material the Ti concentration will increase gradually. Process parameters used in the course of the experiment has been shown in Tab. 5 below.

Table 5. Parameters of the process in parametrisation.

Material	Laser power (P)	Scan velocity (Vs)	Defocusing of beam focus
Ti + Au	75W	1 mm/s	+ 10 mm
	100W		
	125W		
	75W	1.5 mm/s	
	100W		
	125W		
Ti13Zr13Nb + Au	75W	2 mm/s	+ 10 mm
	100W		
	125W		
	75W	3 mm/s	
	100W		
	125W		

4.2 Methodology for evaluating the material obtained

4.2.1 Numerical analysis

The spatial and temporal fluctuation of temperature occur during laser processing of electrodeposited materials. The temperature of melted material heavily influences the kinetics of interdiffusion and interfacial phase formation. Understanding the temperature change at the Ti-Au contact during laser processing is therefore required. The gold-coated Ti specimen is depicted in Fig. 14a). The top of a Ti cylinder with a base diameter of 35 mm and a height of

7 mm is coated with a thin Au layer, as shown in the schematic sketch of Fig. 14b). The representative volume element (RVE) depicted in Fig. 14a) will be taken into consideration as the computational domain for the finite element analysis since the Ti-Au contact is the region of interest for numerical analysis. A 300 μm x 300 μm x 50 μm cube will be used to represent the Ti base metal, and a thin layer of Au with a thickness of 2 μm will be computationally deposited on top of the cuboid. Part of the Ti-Au samples' phases may melt during laser heating; as a result, the computational domain will include both solid and liquid parts at the same time. The apparent or effective heat capacity-based enthalpy approach is used in the current work to enable the modelling of melting in a Ti-Au sample. The following equation describes the enthalpy of a material (pure Au, pure Ti, or a Ti-Au alloy) at a specific temperature (T) [83].

Equation 1 Enthalpy of the TiAu

$$H_i(T) = \int_0^T \left(\rho_i C_{p,i} + \rho_i L_{f,i} \frac{\partial f}{\partial \tau} \right) d\tau \quad (2)$$

In Eq. 2, the symbols i , $C_{p,i}$ and $L_{f,i}$ are respectively the density, specific heat capacity, and latent heat of fusion of the material i .

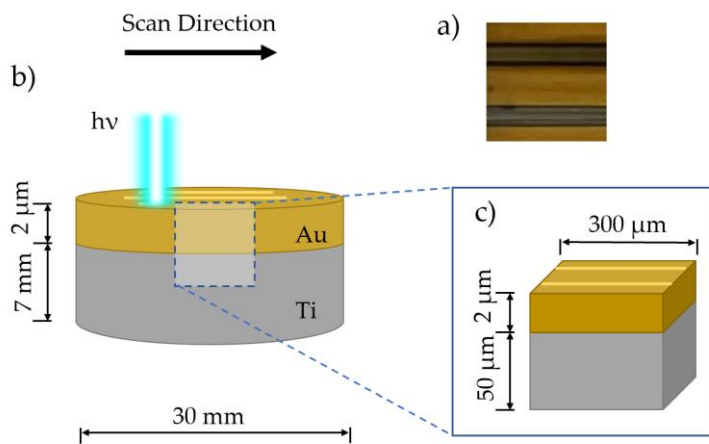


Figure 14. a) View of the Au-Ti sample after processing, b) Scheme of laser processing , c) Representative volumetric element (RVE) of the sample for finite element analysis. Schemes in b and c are not proportional (the vertical axis is greatly stretched compared to the horizontal axis) to allow proper visibility of the coated thin layer.

The thermodynamic CALPHAD database values of Ti-Au system has been obtained from Xiong et al. [84], and the enthalpies of Au (pure) and Ti (pure) are computed as a function of

temperature using OpenCalphad software [85]. The simplified model used for calculation is presented in Fig. 14 b.

A constant laser power of 100 W was being used, and two values of scan speed ($V_s = 1.0$ mm/s and 1.5 mm/s) are employed for the laser system directed onto the electrodeposited Au surface of the Au-Ti system. The computation of temperature variable in the Au-Ti RVE was accomplished using finite element analysis. Fig. 15 displays the computed values of H (T) for Au and Ti. The enthalpy curves in the picture are represented as vertical lines at the melting point of a metal or alloy (1337 K for Au and 1941 K for Ti). The latent heat of fusion is represented by the increase in enthalpy magnitude that is reflected by the length of the vertical line at the melting regime of the H-T curve (L_f). The part of the curve closest to the vertical line on the left represents the solid phase, whereas the part closest to the vertical line on the right represents the liquid phase. Two levels of scan speed ($V_s = 1.0$ mm/s and 1.5 mm/s) are used for the laser system focused onto the electrodeposited Au surface of the Ti-Au system together with a constant laser power of 100 W. Using Elmer Multiphysics software's finite element approach, a coupled set of partial differential equations related to heat transfer and fluid flow are solved to determine the temperature profile in the Ti-Au materials system being heated by a laser. [83,86]. Densities and thermal conductivities of Au and Ti for liquid and solid states are presented in Table 6.

Table 6. Density and thermal conductivity comparison of Ti and Au in the liquid and solid states.

State	$\rho_{Au} [\frac{kg}{m^3}]$	$\rho_{Ti} [\frac{kg}{m^3}]$
Solid (T = 700K)	18817.6	4433.217
Liquid (T = 1950K)	16517.28	4127.93
State	$k_{Au} [\frac{W}{mK}]$	$k_{Ti} [\frac{W}{mK}]$
Solid (T = 700K)	290.4024	17.32635
Liquid (T = 1950K)	153.4242	34.119

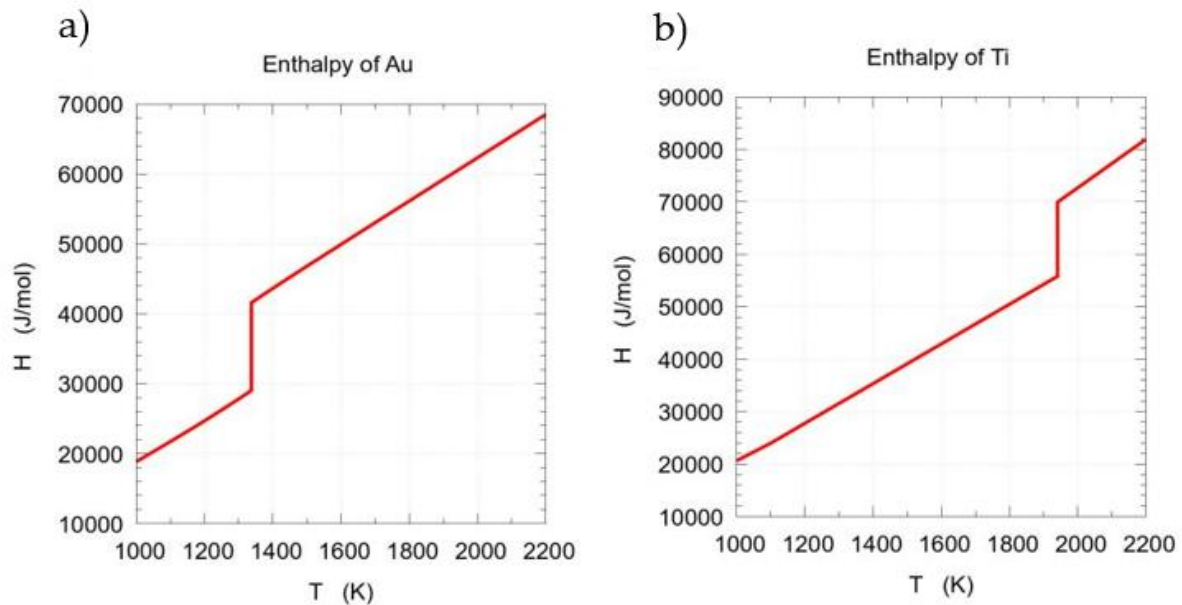


Figure 15. Dependence of the enthalpy of gold a) and titanium b) on temperature. The melting regime of these materials is represented by the projections of the vertical lines of the enthalpy curves on the T axis.

The laser heat source is assigned the flat top heat distribution profile. Temperature dependence of materials properties is considered in the finite element model.

Finite element analysis is used to calculate the temperature variable in the Au-Ti representative volume element (RVE). Fig. 16 depicts the materials system's mesh. Although Fig. 16(a) shows the whole mesh, the inset picture, Fig. 16 b), emphasises the meshing work done in the location where the Au thin film and the basal Ti material meet. In the computational domain, the 3D mesh is represented by tetrahedral mesh components. In order to create a finer mesh in the interface region, sub-meshes are added to the geometric region corresponding to the volume of the thin Au film. There are 29402 nodes and 169505 mesh components in the mesh. Au-Ti system's starting temperature is thought to be 298 K (both Au rich top film and Ti base in the slab are in solid phase). The gold film mostly absorbs the incident heat flux when the top layer of the materials system is exposed to a laser beam with a spot diameter of 245 μm , and heat transfer occurs. The main forms of heat transport in the system are conduction and convection, as will be demonstrated numerically. The partial differential equation (PDE) for heat transfer process in the AuTi computational domain (Fig. 17) undergoing laser processing is given as follow (Eq. 3) [83]:

$$\rho_i C_{app,i} \left(\frac{\partial T}{\partial t} + \vec{u} \cdot \nabla T \right) = k_i \nabla^2 T + Q_{laser} \quad (3)$$

where, $i = \text{Au, Ti}$. In above equation, T is temperature, t is time. The density and thermal conductivity of the material i are respectively denoted as ρ_i and k_i .

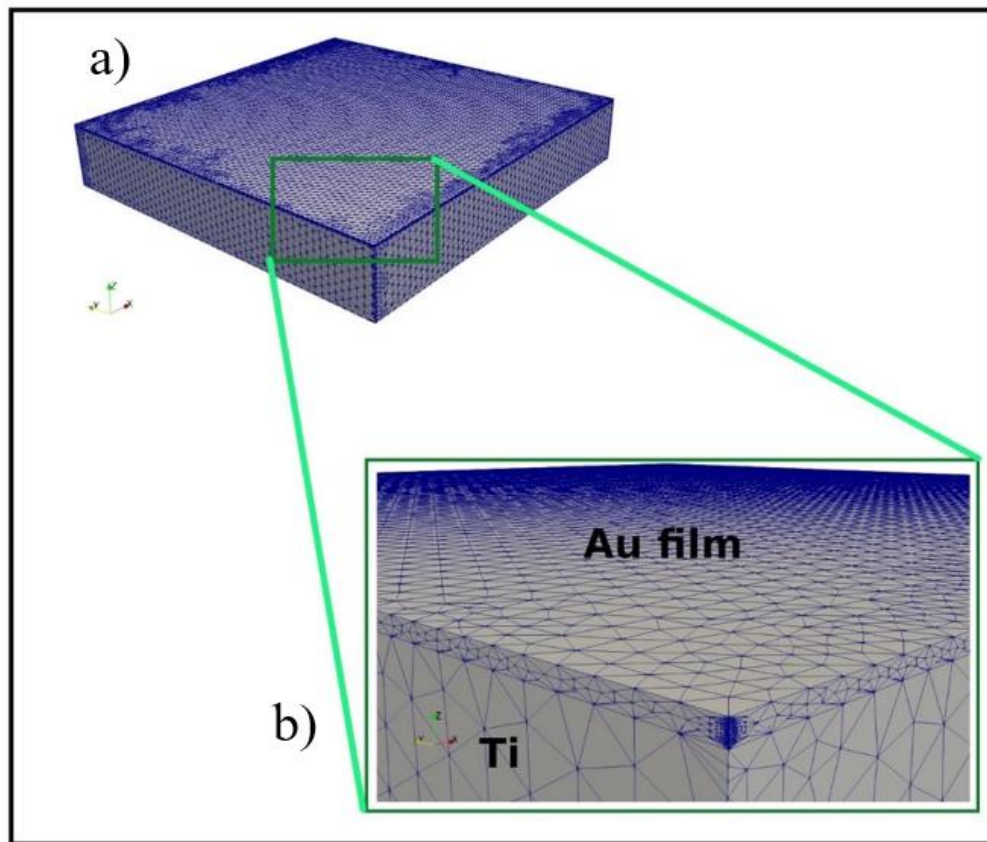


Figure 16. The entire computational domain (volume = $300 \mu\text{m} \times 300 \mu\text{m} \times 52 \mu\text{m}$) with tetrahedral mesh elements a), the inset in b) is an enlarged image of the portion of the domain. As revealed in b) the $50 \mu\text{m}$ thick Ti base has coarse mesh whereas the Au thin film ($2 \mu\text{m}$) is with a relatively finer mesh. The heat from the laser will enter the medium from the top Au surface.

The apparent / effective heat capacity ($C_{app,i}$) of the material is a function of its enthalpy (∂H_i) defined by the following expression (Eq. 4):

$$\rho C_{eff} = \frac{\partial H_i / \partial t}{\partial T / \partial t} \quad (4)$$

Q_{laser} is represented by flat top heat source [74] and is defined by the following expression (Eq. 5):

$$Q_{laser} = \frac{2\alpha P \phi}{\pi r_0^2} U(r_0 - r) e^{-\alpha \delta_z} \quad (5)$$

In Eq. 5, α is the absorption coefficient of Au, and as mentioned in Zhu et al. [87], its value is assumed equal to $8.5E+07 \text{ m}^{-1}$ for the current experiment using particular wavelength of laser. Laser power (P) for the current model is 100 W. ϕ is a function of excitation beam wavelength and fluorescence quantum efficiency. The quantity r_0 is the beam spot radius and it is equal to $122.5 \text{ }\mu\text{m}$. The radial distance of a point (x,y) from the center (x(t), y_0) of a moving laser head is the initial position of the beam center. The scan speed (V_s) of the laser has been defined as $V_s = \frac{dx}{dt} = \frac{x(t) - x_0}{t}$. Two of scan speed values (1 mm/s and 1.5 mm/s) are employed in the model. The quantity $U(r_0 - r)$ will be 0 if $(r_0 - r)$ has a negative value, and 1 if it is positive. δ_z in the expression is the length in the vertical (z direction). On obtaining adequate heat (Q_{laser}) from the laser, the surface material at the vicinity of the laser beam spot can melt and subsequently flow with a flow velocity (\vec{u}) in the melt pool. The two main mechanisms of heat transport in an Au-Ti media heated by a laser beam are conduction and convection, as shown in Eq. 3. The molten regime can extend to a depth that is significantly below the surface for lasers with high power or slow scan rates.

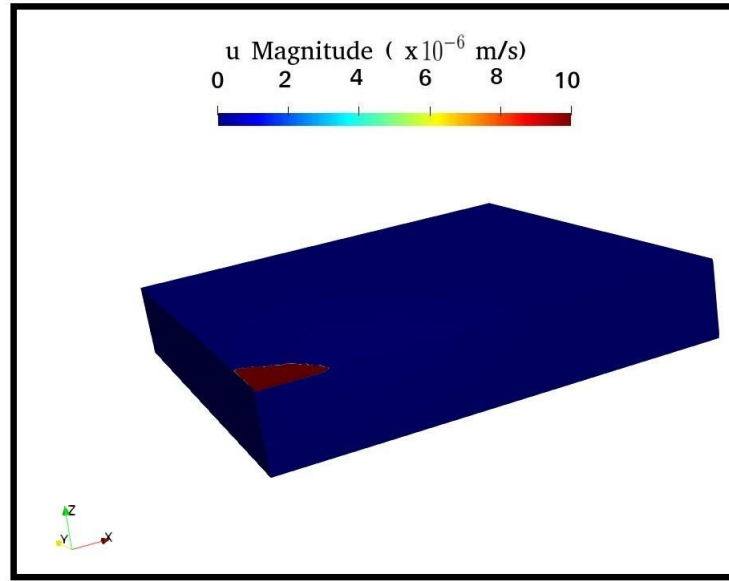


Figure 17. Calculated average velocity at time $t=0.04$ s for a laser with power $P=100$ W and speed $V_s=1.0$ mm/s. Only the area of the Au film that is currently molten is present; the Ti underlying the Au is still solid.

The dynamics of fluid flow in the melt pool is described by the incompressible Navier-Stokes equations:

$$\nabla \vec{u} = 0 \quad (6)$$

$$\rho_i \frac{\partial \vec{u}}{\partial t} + \rho(\vec{u} \cdot \nabla) \vec{u} = \nabla \cdot [-pI + v_i(\nabla \vec{u} + (\nabla \vec{u})^T)] + F_i \quad (7)$$

In the momentum equation (Eq. 7), v_i is the viscosity of liquid material. The expression for Boussinesq approximation is utilized within the F_i term to enable the variation of liquid density only in the vertical direction and thereby ensure the incompressible nature of flow in the melt pool. The simulation figure illustrating the numerically computed average velocity magnitude in the computational domain treated by laser of $P = 100$ W and $V_s = 1.0$ mm/s is presented in Fig. 17. It is important to note that throughout the laser irradiation process, the temperature of the computational domain varies both spatially and temporally. Temperature changes have an impact on qualities including density, thermal conductivity, specific heat capacity, and viscosity. The enthalpy-temperature curves may be used to visualise how heat capacity changes with temperature (Eq. 4). The model takes into account the temperature dependency of the viscosities of liquid and semi-liquid Au and Ti materials and assumes that the viscosities of

liquid Au and liquid Ti are equal to those of other molten metal alloys like Sn-0.7Cu solder. The dynamic viscosity of liquid phases of Au or Ti is represented by the Arrhenius equation [88]. However, for mushy zone, the apparent viscosity is approximated to be equal to the asymptotic viscosity [88]. The solid Au film or Ti block are thought to be made of materials with very high viscosities, so they don't move in a multi-phase system. The input file for ElmerSolver receives the viscosity-temperature and enthalpy-temperature data in tabular data format.

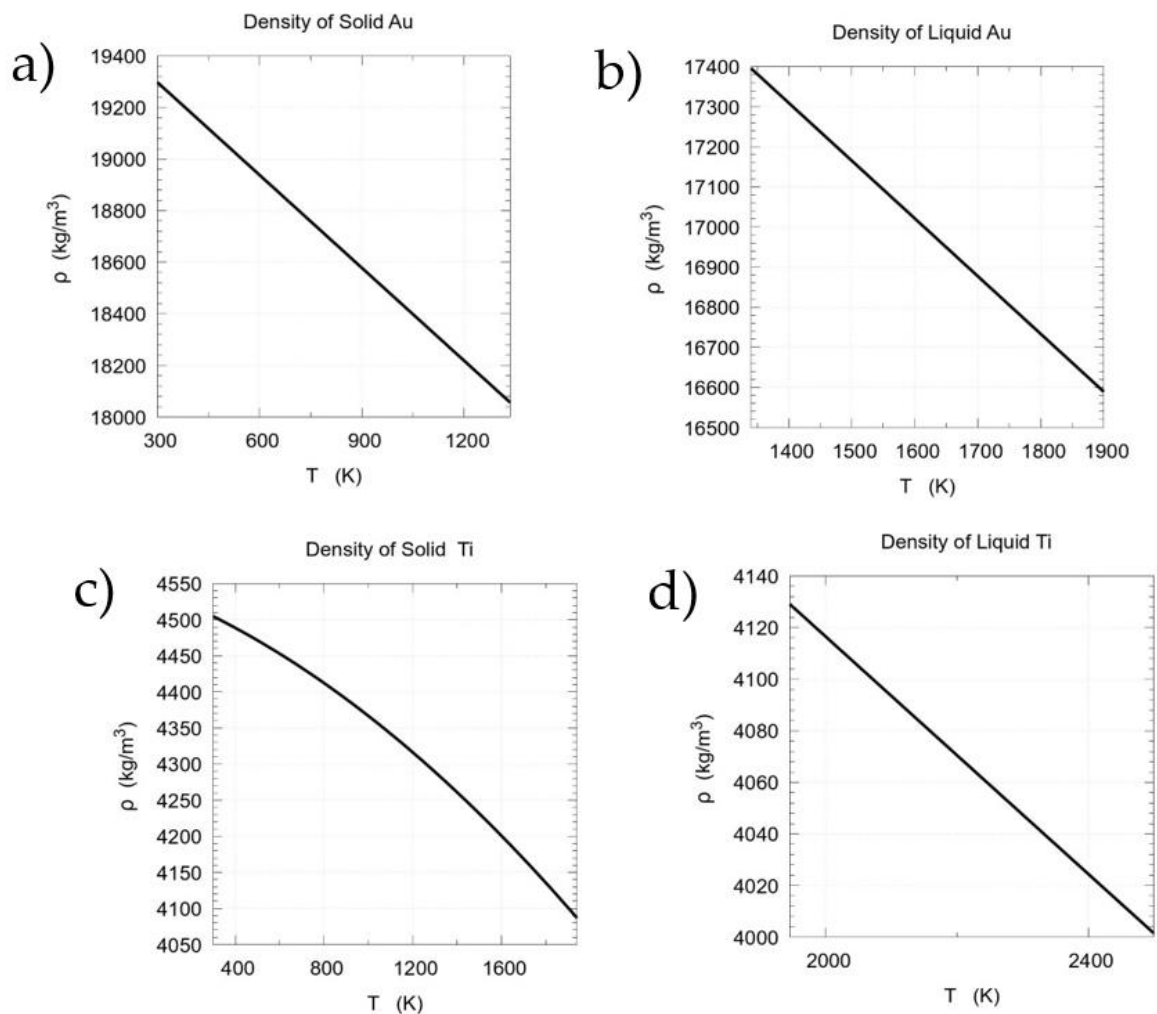


Figure 18. Influence of temperature on the density of Au and Ti (a-d).

The fitted data of density of Au and Ti at both solid and liquid states are plotted graphically against temperature in Fig. 18(a)-(d). The densities of solid Au presented in Fig. 18(a) are derived from the report by Ricci et al. [89]. The values of liquid Au densities as shown in Fig. 18(b) are obtained from the work of Paradis et al. [90]. The values for temperature dependent

density of solid Ti (Fig. 18c) are obtained from the work of Zhang et al. [91] whereas the densities of liquid Ti (Fig. 18d) are obtained from the report by Wang et al. [92]. It can be inferred from the curves that the absolute density of Au is several times larger than that of Ti: $\rho_{Ti(s)} = 4433.22 \frac{kg}{m^3}$ and $\rho_{Ti(lq)} = 4127.93 \frac{kg}{m^3}$ compare to $\rho_{Au(s)} = 18817.6 \frac{kg}{m^3}$ and $\rho_{Au(lq)} = 16517.28 \frac{kg}{m^3}$. With temperature, Au's density drops linearly in both the solid and liquid forms. However, although the density of liquid Ti reduces linearly with temperature, that of solid Ti decreases parabolically. The study of Cook and Van der Meer [93] provided the thermal conductivity measurements for Au in the solid state. The data for liquid state are derived from the work of Petrov et al [94]. The report by Zhang et al [91] is utilized to derive data for thermal conductivity of solid Ti. The thermal conductivity of liquid Ti is derived from the work of Watanabe et al [95]. The k data were fitted against temperature, and graphically presented in Fig. 19a-d. k_{Au} decreases with temperature in solid state (Fig. 19a) whereas increase for liquid state (Fig. 19b). On the other hand, as revealed in Fig. 19c-d, the k_{Ti} increases both for solid and liquid states. The curve of k_{Ti} is non-linear in solid state, whereas it is linearly increasing with T in liquid state. Generally speaking the k_{Ti} is smaller in magnitude than the k_{Au} for a given temperature: $k_{Ti(s)} = 17.33 \frac{W}{mK}$ and $k_{Ti(lq)} = 34.12 \frac{W}{mK}$ compare to $k_{Au(s)} = 290.40 \frac{W}{mK}$ and $k_{Au(lq)} = 153.42 \frac{W}{mK}$. One of the variables in the numerical model is temperature, and the user defined functions (UDFs) that specify how thermal conductivity and density change with temperature are called by the solver during computation.

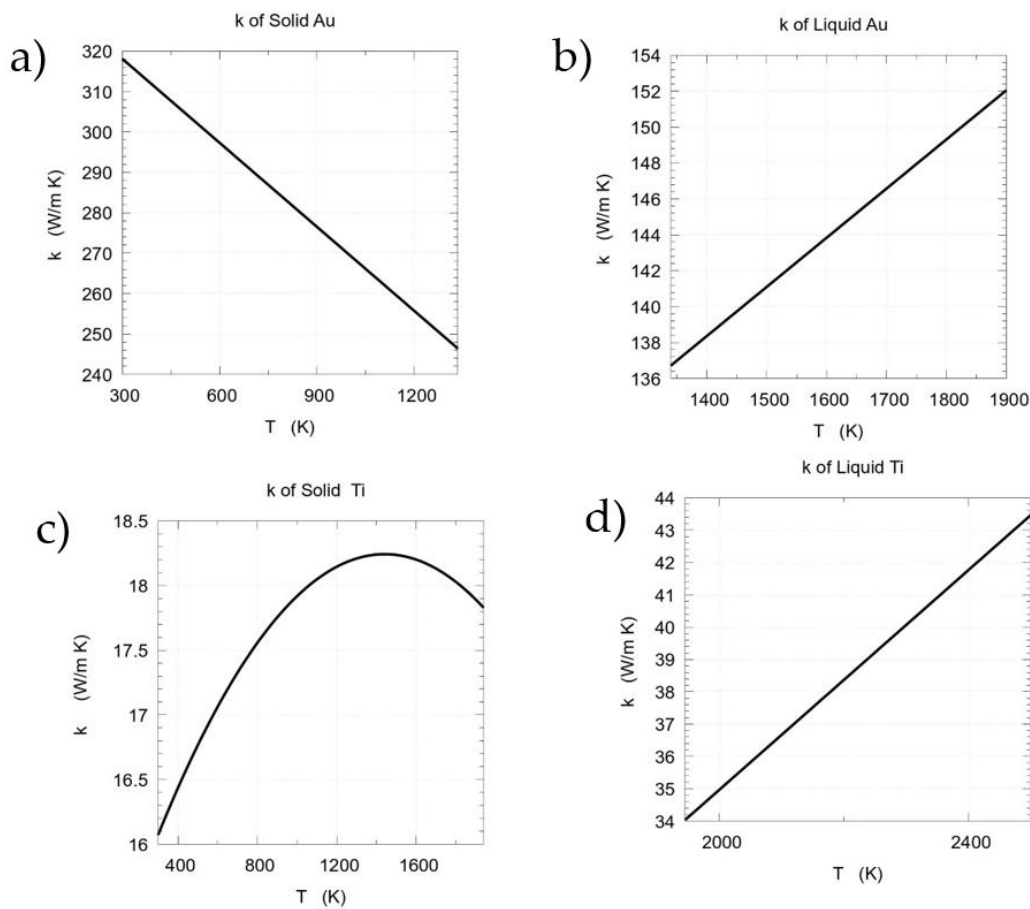


Figure 19. The pictures (a)- (c) show the temperature dependency of the thermal conductivities of Au and Ti (d). The thermal conductivity of (a) solid Au is observed to decrease with temperature, but the kth of (b) liquid Au, (c) solid Au, and (d) liquid Ti rise with temperature.

4.2.2 Hardness assessment by Nanoindentation simulation study

In the case of Ti material, a hexagonal closed pack (HCP) unit cell is initially constructed, and it is subsequently repeated in all directions to create a supercell with 66912 atoms. During replication, a procedure is used to create it as an orthogonal supercell of $l_x = 120.28 \text{ \AA}$, $l_y = 121.96 \text{ \AA}$, and $l_z = 79.17 \text{ \AA}$. It is done by copying the unit cell by n times in x direction, m times in y direction and r times in z direction to form a supercell. A unit cell with a simple cubic structure is duplicated in the Intermetallic Compound (IMC) Ti_3Au in the X , Y , and Z directions to create a supercell: $l_x = l_y = 122.72 \text{ \AA}$, and $l_z = 81.81 \text{ \AA}$. The total number of atoms in the nanoslab of Ti_3Au IMC is 73728 (55296 Ti atoms and 18432 Au atoms). The X , Y , and Z axes in this simulation setup are situated along the $[1\ 0\ 0]$, $[0\ 1\ 0]$, and $[0\ 0\ 1]$ crystallographic

directions, respectively. The top active region, which is being indented, and the bottom fixed region make up the domain of the nanoindentation simulation. The bottom fixed zone offers the rigid support for the nanoindentation process since the atoms there do not move during the duration of the simulation. The fixed region spans from the base of the slab to the upward length $d_{fx} = 40 \text{ \AA}$, and the length of the active nanoindentation region $= l_z - d_{fx}$. The indenter is a virtual one, and is represented by a non-atomic rigid and repulsive sphere of radius $(R) = 30 \text{ \AA}$. The indenter is initially placed so that the distance between its centre and the top surface of the slab exceeds R by a small percentage of 1 \AA .

The indenter upon contact with the atoms of the nanoslabs of Ti or Ti_3Au , exerts the following repulsive force $F(r)$:

$$F(r) = \begin{cases} -K_c(r - R)^2; & r < R \\ 0; & r \geq R \end{cases} \quad (8)$$

In Eq. 8, K_c is the specified force constant of value $1300 \frac{eV}{\text{\AA}^3}$, and r is the distance from the atom to the indenter's center. In order to model the Ti-Ti atomic interactions in the pure Ti slab, Embedded Atom Method (EAM) potential developed by Zhou et al. [96] is utilized. The interactions between Ti-Ti pairs and Au-Au pairs in intermetallic Ti_3Au are modelled using EAM interatomic potentials [96]. Morse potentials have been used to characterise the interactions between the Ti and Au atoms. The MD simulations were performed using the LAMMPS software [97]. Both Ti and IMC materials had the same boundary conditions, timestep size, and loading rate (for indentation motion). Iteration timestep is assumed to be 1 fs. In the X and Y directions, periodic boundary conditions (PBC) are used, whilst non-periodic and shrink-wrapped boundary conditions are used along the Z direction. The periodicity in the plane parallel to the indented surfaces will be ensured by the employment of PBC along the X- and Y-direction [98]. The indenter loading rate of 0.5 \AA/ps is utilized in the models. The visualization of the nanoslabs were done with OVITO software [99].

4.2.3 Roughness tests

Measurements of surface roughness were conducted using the contact method with a Surtronic 25 surface roughness tester by Taylor Hobson (England). The measurements length was 4 mm and the accuracy of the measurements was $\pm 2\%$ of read value. On the basis of the measurement results obtained, the average Ra and Rz parameters were determined. An average of five measurements was determined for each sample.

4.2.4 Light microscopy

Preliminary assessment of the effects of laser micromachining was carried out on an outer section (normal plane) by a metallographic light microscope Axio Observer (Zeiss, Oberkochen, Germany).

4.2.5 Scanning Electron Microscopy (SEM)

SEM studies were performed in a scanning electron microscope SEM EVO MA10 (Zeiss, Oberkochen, Germany), equipped with an Energy Dispersive Spectrometer (EDS) for chemical composition analysis. The aim of these studies was to characterize the morphology and chemical composition of the tested materials, in particular changes in Au content as a function of the distance from the surface.

4.2.6 X Ray Diffraction Analysis

The phase analysis was carried out on an X'Pert PRO X-ray diffractometer (Panalytical, The Netherlands), equipped with an X-ray tube with a cobalt anode ($\lambda_{Co}=1.7909 \text{ \AA}$), powered with a voltage of 40 kV. The heater current was 30mA. The diffractograms were recorded in the Bragg-Brentano geometry. In order to precisely determine the phase composition of the remelted layer and compensate for the influence of the base material, Grazing Incidence Diffraction (GID) geometry was used, dedicated to the precise analysis of a low-thickness material (located near the surface). X'Pert High Score Plus (v. 3.0e) software with a dedicated

Inorganic Crystal Structure Database - ICSD (FIZ, Karlsruhe, Germany) was used to analyse the results.

4.2.7 Electron Backscatter Diffraction (EBSD)

The TiAu and Ti₁₃Zr₁₃NbAu variants were analysed using orientation imaging microscopy (OIM) with electron backscattered diffraction (EBSD) on a Zeiss Supra 35 Scanning Electron Microscope. OIM measures crystal orientations on a regular grid by electron diffraction. Obtained data are used to produce orientation or phase maps of the scanned area on the sample. The grain structure was studied by scanning a 15x15 µm area on the cross section of the remelting zone at a step size of 0.2 µm. The data was cleaned using a level 4 neighbour orientation correlation process and a grain confidence index standardization with a 2 degree grain tolerance angle threshold. Finally, a coincidence index filter of 0.005 was applied to remove any incorrectly indexed points. The quantitative results presented in the tables have been calculated on the basis of averaged values from min. 3 representative areas.

4.2.8 Transmission Electron Microscopy (TEM)

TEM studies were performed using a transmission electron microscope S/TEM TITAN 80-300 by Thermo Fischer Scientific (formerly FEI), equipped with a STEM scanning system, BF, DF and HAADF scanning and transmission detectors, CETCOR Cs condenser aberration corrector from CEOS, Ultrascan camera from Gatan, EDS energy dispersion spectrometer from EDAX and GIF Tridiem energy filter from Gatan. Samples for TEM studies were prepared using the Focused Ion Beam (FIB) technique using the SEM/Ga-FIB Helios NanoLab™ 600i microscope by Thermo Fischer Scientific (formerly FEI). Crystal Maker and Single Crystal software (CrystalMaker Software Limited, version 10.4.1) were used to simulate the crystal structure and electron diffraction.

4.2.9 Atomic Force Microscopy (AFM)

In order to observe the nature of the surface topography and to assess the roughness more accurately, tests were carried out using Atomic Force Microscopy. The XE-100 atomic force microscope was used in non-contact mode for the observation (AFM, Park System, Mannheim Germany). The analyses were taken over a 20 x 20 μm area scan. As a typical parameter determining the surface roughness, the arithmetic mean of the ordinate profile (Ra) was determined. Five measurements were made for each sample.

4.2.10 Wetting Angle measurements

Wettability tests were carried out using the sitting drop method with an Attension Theta Flex optical tensiometer (Biolin Scientific, Darmstadt, Germany) and OneAttension software. Distilled water and diiodomethane were used for testing. A drop of 1.5 mm^3 was applied to the surface. Each test lasted 60 s with a measurement frequency of 1 Hz. Surface free energy SFE was determined using the OWRK method (a.k.a. Owen-Wendt). The measurements were carried out at temperature of approximately 25.0 ± 1.0 °C. Each measurement was repeated 5 times to ensure statistical significance of the measurement.

4.2.11 Corrosion Tests

The Tafel method was used to examine the tested samples' corrosion resistance. The test was conducted using a three-electrode system in a water-jacketed cell with a Pt wire as an auxiliary electrode, a saturated calomel electrode SCE as a reference electrode, and tested samples as a working electrode. The test stand was an Autolab 302 N potentiostat from Metrohm AG in Herisau, Switzerland, controlled by the NOVA software (v. 1.1). After measuring the open circuit potential (E_{OCP}) for each sample for 60 minutes, the potentiodynamic test was initiated from the initial potential ($E_{\text{int}} = E_{\text{OCP}} - 100$ mV) to 278 mV. Each variant was evaluated three times for statistical purposes. One mV per second (mV/s) was the polarization rate. 250 ml of Ringer's solution was used for all the electrochemical assays ($\text{NaCl} - 8.6$ g/cm³, $\text{KCl} - 0.3$ g/cm³, $\text{CaCl}_2 \times 2\text{H}_2\text{O} - 0.33$ g/cm³) at 37 ± 1 °C and pH 7.4.

The third method, electrochemical impedance spectroscopy (EIS), was also used to determine the electrochemical properties. First, the samples were stabilized in the test environment for 5 min without current flow, and then a flow through the AC system fixed at an amplitude of 10 mV and frequencies between 100 kHz and 10 mHz was used to determine the electrochemical properties. Nyquist and Bode graphs were used to display the results. Using the AtlasLab and EC Lab software, numerically produced curves were fitted to the experimental results to create an electrical equivalent circuit (EEC) to replicate the correlations seen in these research. The EEC utilized non-linear CPEs (constant phase elements) in addition to conventional resistors.

4.2.12 Tribological tests

A CSM tribometer (CSM Instruments, Switzerland) was used to perform the wear test using the ball-on-plate technique. A 5.6 mm diameter ZrO₂ ball was utilized as a counter specimen. Tests were performed in Ringer's solution (NaCl - 8.6 g/cm³, KCl - 0.3 g/cm³, CaCl₂ × 2H₂O - 0.33 g/cm³) at room temperature and pH 7.4. The wear test was conducted with an amplitude of 4 mm with load of 2 N and a frequency of 1.25 Hz with 2500 cycles and acquisition rate equal to 4.0 Hz. The value of the coefficient of friction was calculated using the data that were taken during the experiment.

4.2.13 Nanohardness test

Nanohardness tests were conducted in accordance with ISO 14577 on an NHT+Step 300 (Anton Paar, Technolusions, Poland). The instrumented indentation technique (IIT) involves pressing an indenter of known geometry (for this study the diamond Berkovich penetrator has been used as the most used as a tip for nanoindentation standard ISO 13577) into the surface while both penetration depth and normal load are monitored. The indentation hardness and elastic modulus were obtained from the force-displacement curve. In order to facilitate material

comparisons, the same test parameters were used for each sample variant: max load = 100 mN, linear loading/unloading rate: 200 mN/min, pause after test: 10 s. In order to demonstrate and determine the variation in hardness parameters and Young's modulus, hardness tests were carried out on the gold layer deposited on Ti and Ti13Zr13Nb, and then the results obtained were compared to those of the two selected variants for each of the base materials. In total, nanohardness results were obtained for (Au on Ti substrate, Au on Ti13Zr13Nb substrate, TiAu 1 mm/s, TiAu 1.5 mm/s, Ti13Zr13Nb Au 2 mm/s and Ti13Zr13Nb Au 3 mm/s). Five measurements were taken for each variant, of which the two outliers were discarded. The remaining 3 measurements were subjected to calculation of the average and standard deviation.

4.2.14 Cytotoxicity tests

Cell lines and culture conditions

In order to determine the biocompatibility of the tested materials, with modified growth surfaces, cultures of normal cells were performed on them and incubated for several hours. Experiments in an in vitro system were performed on model human cell lines, on normal fibroblasts, NHDF (Neonatal Human Dermal Fibroblasts; CC-2509 LONZA). The cell line selected for the study and the in vitro culture conditions met the requirements for ISO 10993-1:2009I for the biological evaluation of medical materials using standard in vitro assays.

Monolayer cultures of NHDF line cells were grown using standard culture media and supplements in a Heracell™ 150i, Thermo Scientific™ hothouse with a constant CO₂ concentration (5 %), temperature (37 °C) and constant humidity (60 %). Cells were cultured in DMEM:F12 HAM (1:1) medium (Sigma, Germany), enriched with 10 % fetal bovine serum (FBS, fetal bovine serum; EurX, Poland); with the antibiotic [80 µg/ml] gentamicin (Krka, Poland). After obtaining 80 % confluence, cells by trypsinization (digestion with 0.25 % trypsin; Sigma) were transferred from the culture bottles into reaction dishes containing previously prepared UVA-sterilised test materials. Approximately 10x10⁴ cells suspended in 1 ml of fresh culture medium were seeded as controls directly onto the well of the culture plate (Satstedt) or onto the surface of the test materials (numbered 1-8). Incubations were conducted for a further 48 hours, under standard conditions, in an a.i. incubator.

Evaluation of cell growth on material and surface biofilm formation

To evaluate the survival and growth of NHDF fibroblasts on the materials, the LIVE/DEAD™ Viability Kit (Thermo Fisher Scientific) staining method was used for microscopy. After 48 hours of incubation on the test materials, the biological material was labelled in a 20-minute procedure according to the manufacturer's protocol, washed with saline solution and then the cell biofilm was fixed using 70% EtOH solution (Chempur). Prior to fixation, a set of vivo images was taken using a Leica PAULA System camera (Personal AUtomed Lab Assistant), which allowed the number and viability of cells to be assessed in the control panel (directly on the culture plastic) and image acquisition was performed for biofilm assessment. After fixation, staining with DAPI solution (2 µg/ml) was additionally performed on the materials, the slides were covered with 50% glycerol solution (Sigma) and subjected to microscopic evaluation with a bacteria kit using Geimza and May-Grunwad stains (Chempur). Biofilm assessment was presented as % cell surface coverage of the material in contrast to the plastic culture plate (positive control) - signals from cell nuclei of cells fixed on the materials were counted.

Image acquisition from the fixed slides was performed using an Olympus FluoView FV1000 scanning confocal microscope, with a spectral detection system with SIM scanner. By using an inverted microscope, it was possible to visualise and analyse the rapid changes occurring in the biological material scanned on the surface of the specimens. Thanks to its high resolution and performance, the system allowed multidimensional imaging (3D) of cell structures and detection of blue signals for cell nuclei, where genomic DNA is bound by the fluorescent dye DAPI. Images were taken in the blue channel (DAPI) at 400 x magnification, image slopes were saved in .TIFF format (Fig. 75), which were then used for statistical analysis of the cell number signal on the surface.

Signal analysis of microscopic images

Using Matlab R2022a functions, an analysis of the positive signals from the images obtained by confocal microscopy was performed. A conversion from greyscale to binary, i.e. black and white (binarisation) was performed using the `im2bw(I,level)` I-image, level function. Values in the image above the level were converted to white (1) and below to black (0). The

number of pixels in the image with values of 1 and 0 was then counted. The results, obtained, were presented as the ratio of the white signal (from the cell nuclei), to the background signal. The results were normalised to the control population incubated on culture plastic and presented as the summed up signal for the blue channel from the scanned area (Fig. 75), in addition to the percentage change relative to the untreated control (Fig. 74).

5 Results and Discussion

5.1 Numerical Analysis results

The results of finite element analysis are presented in Fig. 20 and 21. For a given laser heating power of 100 W, Fig. 20 mainly highlights the spatial-temporal evolution pattern of T in the dimensional computational domain at two Vs values. At the final simulation time of $t = 0.2$ s, the laser focal point is still somewhere within the computational domain for $V_s = 1.0$ mm/s, whereas this point already reaches the end length of the Au-Ti computation domain at $V_s = 1.50$ mm/s. The intensity distribution of irradiation decreases exponentially with the radial distance from the focal point, and thus the Au surface is exposed to a relatively larger amount of irradiance when the scan speed is less for a given power value. Hence the surface and interface temperature at the vicinity of laser beam focal point reaches a relatively higher value in Fig. 20(a) than as compared to Fig. 20(b). The temporal evolution of T at the interface point located $2 \mu\text{m}$ below the starting corner of the domain is graphically plotted for the two scan speeds in Fig. 21

For $P = 100\text{W}$, $V_s = 1.0$ mm/s, the peak temperature is 2133 K whereas the maximum temperature reached by this interface for laser with $P = 100\text{W}$, $V_s = 1.50$ mm/s, is about 1969 K. It must be highlighted that for a total laser heating duration of 0.2 s, the interface point in the computational domain irradiated by 100 W, 1.0 mm/s remains at a temperature above the melting point of Ti ($T_{m,Ti}$) for 97 ms. However, when using the laser of same power but larger scan speed of 1.5 mm/s, the interface point remains at $T > T_{m,Ti}$ for less than 5 ms. Thus, heating the medium with laser at lower scan speed of 1.0 mm/s accounts for larger convection effects during the interfacial reaction and melt pool evolution.

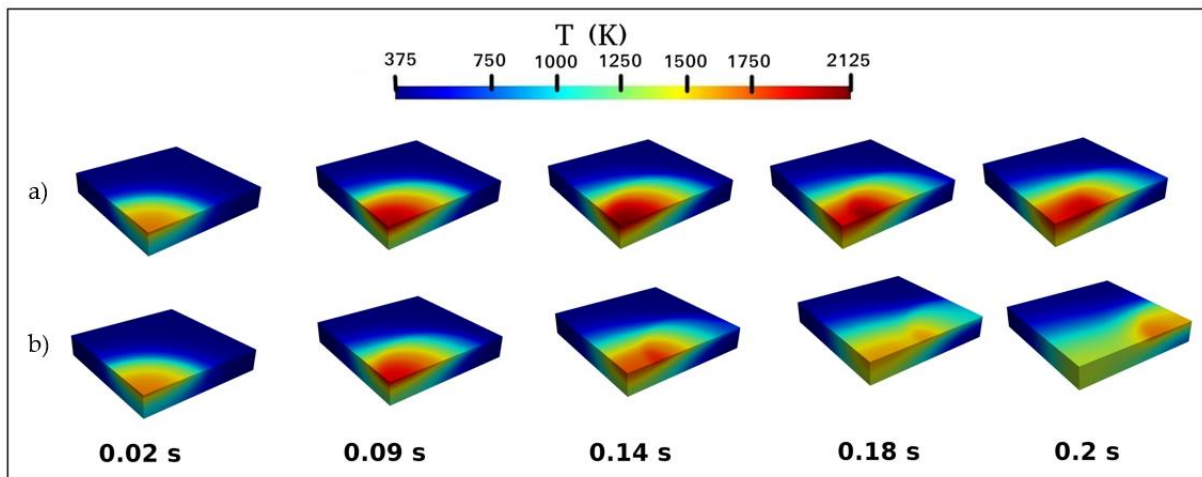


Figure 20. Thermal distribution profiles on the 3D computational domain at different time for heating by the 100 W laser source moving with a scan speed (V_s) = (a) 1.0 mm/s , and (b) 1.5 mm/s.

It is obvious that surface and interface of the Au-Ti system reaches high temperature

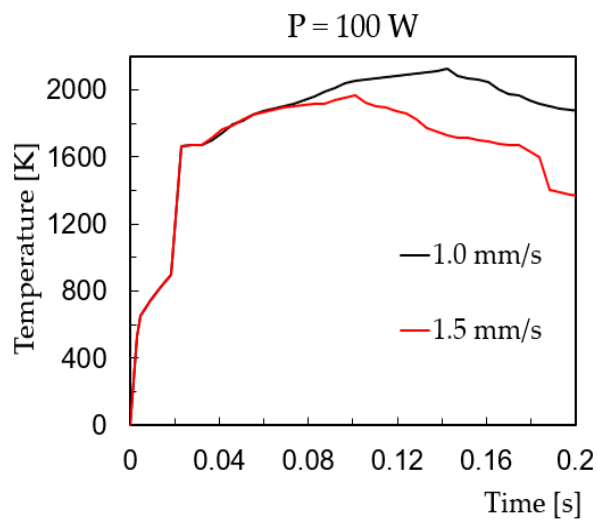


Figure 21. Influence of scan speed of the laser on the temporal evolution pattern of T at the interface point 2 μm below the surface located at starting point of the laser beam.

5.2 Indentation test for understanding the mechanical response of Ti and Ti₃Au slabs at nanoscale

Molecular Dynamics (MD) techniques were used in this study to carry out atomistic simulations of the nanoindentation process of the Ti and Ti₃Au nanostructures. The simulation set up with nanoslab of dimensions $l_x \times l_y \times l_z$ is shown in Fig. 22a. The supercells of Ti and Ti₃Au were constructed using AtomsK software [100].

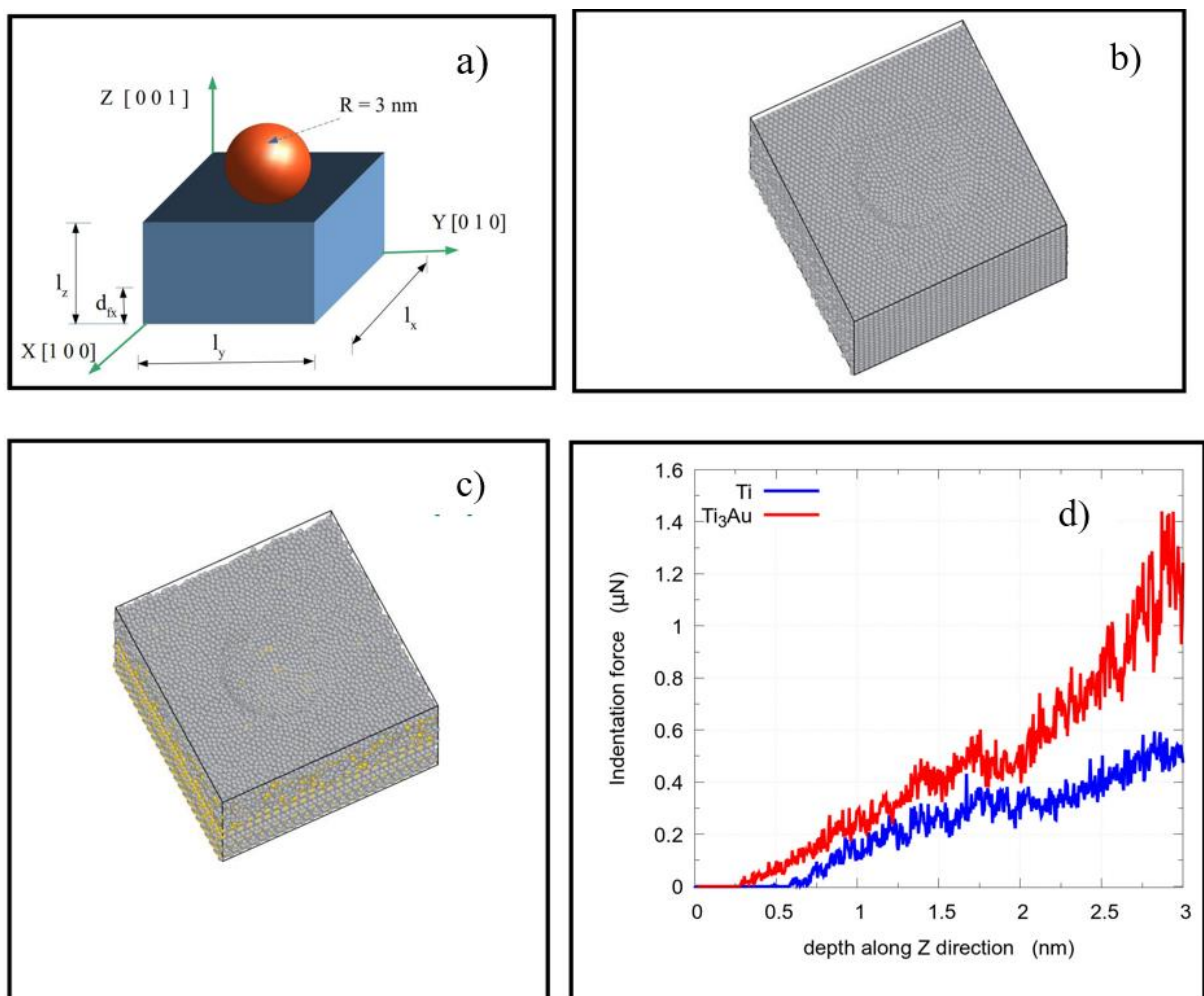


Figure 22. The outcomes of the MD simulations for nanoindentation

The conceptual design for the MD simulation setup for the nanoindentation test. The spherical indenter's radius (R) is 3 nm. The dimensions of the slab corresponding to initial configuration is indicated as $l_x \times l_y \times l_z$. For Ti supercell (constructed in an orthogonal mode for a unit cell of HCP structure), $l_x = 120.28 \text{ \AA}$, $l_y = 121.96 \text{ \AA}$, and $l_z = 79.17 \text{ \AA}$. On the other hand, the dimensions for Ti₃Au supercell (built from simple cubic unit cell) are $l_x = l_y = 122.72 \text{ \AA}$, and l_z

= 81.81 Å. In both of these nanostructures, the atoms within the vertical length of $d_{fx} = 40$ Å from the slab base are kept fixed during the simulation. The simulation results for the timestep when the indenter travels at a depth of 2.5 nm for Ti b) and Ti₃Au c) nanostructures are shown. In these graphics, the gray spheres represent Ti atoms and the yellow spheres represent gold atoms. The curves in d) show how the resultant indentation force varies with the indenter's vertical displacement. The pictures in Fig. 22b and 22c shows indented structures when the indenter has travelled 2.5 nm in depth from its starting location, in both cases the shape of the indentation on the upper side is very clearly visible. It's crucial to take into account the dislocations that are present in the indented nanostructures in addition to the geometry of the indentation. While the dislocations associated with the HCP-structured Ti slab (Fig. 22b) are evenly distributed around the indentation shape's periphery, those associated with Ti₃Au (Fig. 22c) appear to be distributed more unevenly throughout the active regions. The existence of Ti (grey) and Au (yellow) atoms, as well as their initial arrangement in a basic cubic structure, results in a non-uniform distribution of dislocations during processing. The configuration of the dislocation motion trajectories and their reaction to the applied force will undoubtedly have an impact on how the treated material structure behaves mechanically. The propensity of a continuum scale material to experience dislocation depletion [101] following stress is of special relevance because this can have a significant impact on characteristics like hardness.

The load-displacement curves for Ti and IMC material during the nanoindentation test are shown in Fig. 22d. The data are recorded while the indenter has not yet finished indenting the entire active zone as the maximum indentation depth (horizontal axis) is 3 nm. The range of indenter force (in N) values discovered in this work for pure Ti is well in line with the findings of Verkhovtsev et al. [102]. While their study models the Ti-Ti interaction using an empirical Finnis-Sinclair-type potential, this work uses an EAM potential, which can account for the slight differences in the results. Additionally, several potentials are used in their research to illustrate how the Ti atoms and the indenter interact. The fact that the indentation force values for a pure Ti slab in this study were comparable to those in their work verifies the accuracy of used model. From Fig. 22 d) force-distance curves, it is clear that the atoms of IMC Ti₃Au exert more force on the indenter than do those of pure Ti. For an example, at a given indentation depth of 25 Å, the indenter penetrating the pure Ti slab experiences a force of 0.36 µN from the adjacent Ti atoms whereas the indenter surrounded by Ti+Au atoms of IMC slab is associated with a force of 0.82 µN. These curves can be used to make an estimation of the hardness of

these two materials. The ratio of the highest indentation force to the contact area can be used to understand the hardness for a nanoindentation method [103]. The contact area between the two systems at the critical indentation depth for the simulation configuration provided with the same indenter will not be significantly different, and based on these curves, it can be inferred that the IMC Ti_3Au will have a higher hardness value. The work of Svanidze et al. [31] reports experimental evidence of it, that the hardness value of β - Ti_3Au is about 4 times larger than that of pure Ti. This fact therefore supports our hypothesis. The high hardness of the IMC material during indentation in the initial phase influences from the interaction of the Ti and Au atoms, and the dislocation exhaustion as a result of the reconfiguration of the Au atoms within the majority of atoms. The work of Svanidze et al. [31] also reports an improvement in intermetallics' wear characteristics in addition to an increase in hardness and this can also be justified by the enhanced cohesion of the surface atoms, and certainly the presence of two types of atoms in the IMC has a role in it. Such behaviour of IMC makes it a potentially favourable candidate in the design of harder and super biocompatible materials. IMC's behaviour makes it a potentially advantageous candidate for the development of more durable and more biocompatible materials.

5.3 Roughness Tests

Hardness tests were performed on samples immediately after preparation and electrochemical application of the gold layer. For both alloys used (Ti and TiZrNb), the aim was to make a compromise between the need to etch the surface in order to remove the contaminants and uneven oxide layers [104], which forms almost immediately after the sample is exposed to the air and causes delamination of the deposited layer to the substrate, and obtaining a roughness Ra lower than that found in natural tissue (for the purposes of this work, this was a coronary vessel). According to the literature, the Ra value should not exceed 1.04 μm [81]. For samples from the Ti group, the Ra value obtained is the same as the roughness value for the coronary vessel, while in the case of $Ti_{13}Zr_{13}Nb$, it was possible to adjust the etching bath in such a way that the roughness was lower and the adhesion of gold to the substrate was still satisfactory. The hardness test results for the individual groups of samples are presented in Tab. 7 and Tab. 8. For both Ti and $Ti_{13}Zr_{13}Nb$, roughness in the acceptable range of no more than 1.04 μm was achieved. However, it should be noted that the roughness is higher

for the Ti samples, which is statistically significant, and attempts to reduce the roughness by selecting other layer deposition methods should be considered in future studies.

Table 7. Roughness measurements for Ti based sample group

Ti + Au	Sample 1		Sample 2		Sample 3		Sample 4		Sample 5		Total	
Measurement no	Ra [μm]	Rz [μm]	Ra [μm]	Rz [μm]								
1	0.96	5.10	0.94	5.60	1.04	6.20	1.14	8.30	1.12	6.50		
2	0.90	5.40	1.02	6.80	1.12	6.30	0.98	6.00	1.06	7.10		
3	1.02	6.00	1.04	6.30	1.10	6.20	1.02	6.10	1.58	8.20		
4	0.95	5.40	1.00	6.50	0.94	6.40	1.00	6.70	1.14	9.10		
5	0.81	4.90	1.00	5.90	1.14	6.70	1.08	6.80	1.02	5.40		
Average	0.93	5.36	1.00	6.22	1.07	6.36	1.04	6.78	1.18	7.26	1.04	6.40
Standard deviation	0.07	0.37	0.03	0.43	0.07	0.19	0.06	0.82	0.20	1.29	0.13	0.96

Table 8. Roughness measurements for Ti13Zr13Nb based sample group

Ti13Zr13Nb + Au	Sample 1		Sample 2		Sample 3		Sample 4		Sample 5		Total	
Measurement no	Ra [μm]	Rz [μm]	Ra [μm]	Rz [μm]								
1	0.40	2.90	0.45	2.20	0.44	4.10	0.50	3.90	0.44	3.80		
2	0.44	3.40	0.43	2.10	0.46	3.60	0.52	4.90	0.56	3.50		
3	0.56	3.50	0.35	3.00	0.56	5.10	0.55	4.70	0.45	2.20		
4	0.41	2.90	0.40	3.00	0.36	3.10	0.52	4.80	0.35	3.00		
5	0.40	3.00	0.40	3.60	0.42	3.50	0.68	4.90	0.36	3.10		
Average	0.44	3.14	0.41	2.78	0.45	3.88	0.55	4.64	0.43	3.12	0.46	3.51
Standard deviation	0.06	0.26	0.03	0.56	0.07	0.69	0.06	0.38	0.08	0.54	0.08	0.83

5.4 Light microscopy

Images taken using light microscopy for samples both after etching and after gold plating are presented in Fig. 23 below. Both materials after etching are characterised by a rough surface that is difficult to distinguish. In the images after application of the gold layer, we see a homogeneous, intense yellow gold layer with a partially mapped surface roughness. In microscopic images, discontinuities of the coating are not visible.

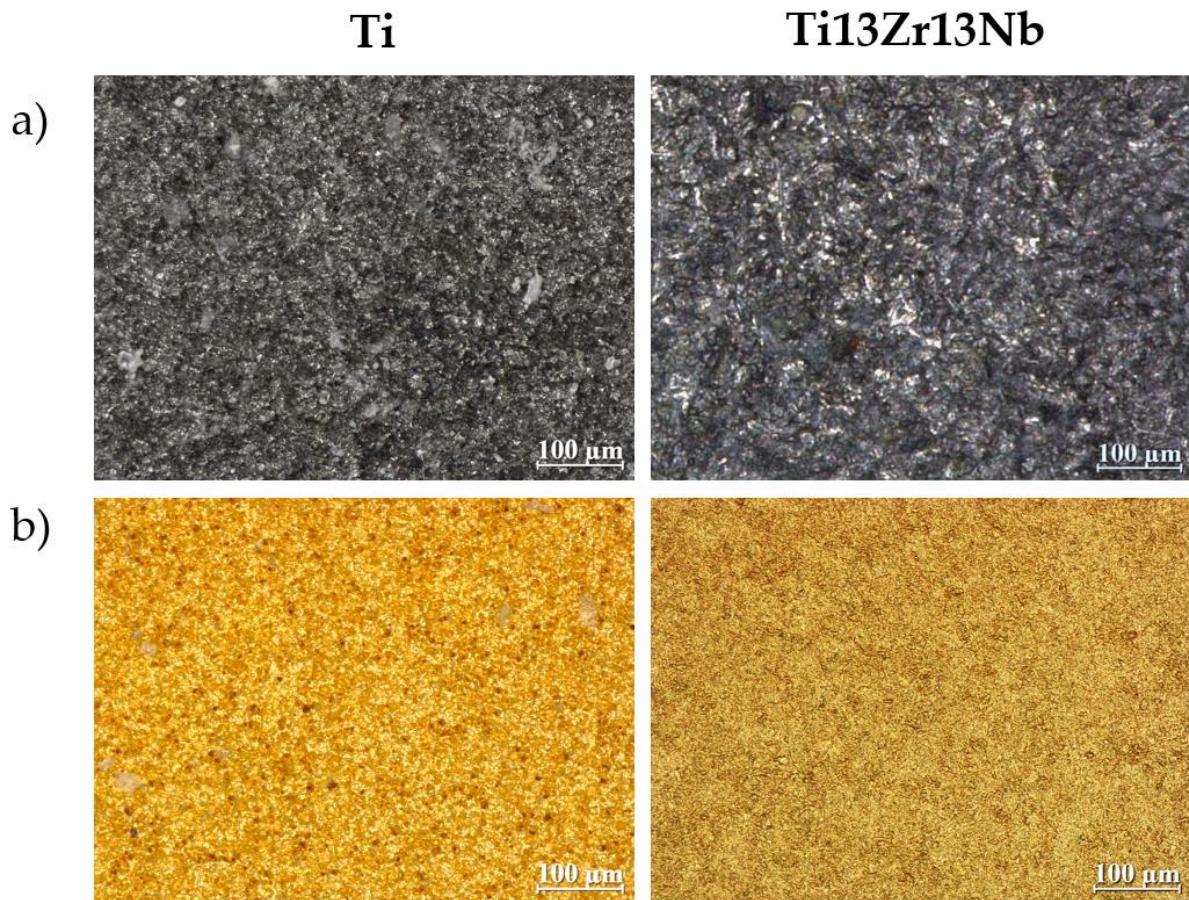


Figure 23. Light microscopy images of (a) pure Ti and Ti13Zr13Nb samples, (b) samples after Au coating

The images from the light microscope (Fig. 24) show the Ti surfaces after laser treatment, using various parameters (scan velocity, laser power). It can be seen that the choice of parameters causes the coating to melt in different proportions with the substrate material. For all variants, a distinction can be made between the heat-affected zone and the actual remelting. In the case of low power (75W), melting can be seen, with characteristic fluctuations indicating that at least one of the system components (Au) is in a liquid state. For variants with $P=100W$, we can distinguish a widening of the heat-affected zone and a metallic colour of the remelting area. The remelting zone is characterised by a high homogeneity with a tendency towards a dendritic structure for the $P=100W$ and $V=1mm/s$ variants. In the case of the variant with the highest applied power ($P=125W$), we can see visible chiaroscuro stresses along the grain boundaries. It was assumed that, due to this microstructure, the resulting coating is not predisposed to useful properties and can be discarded.

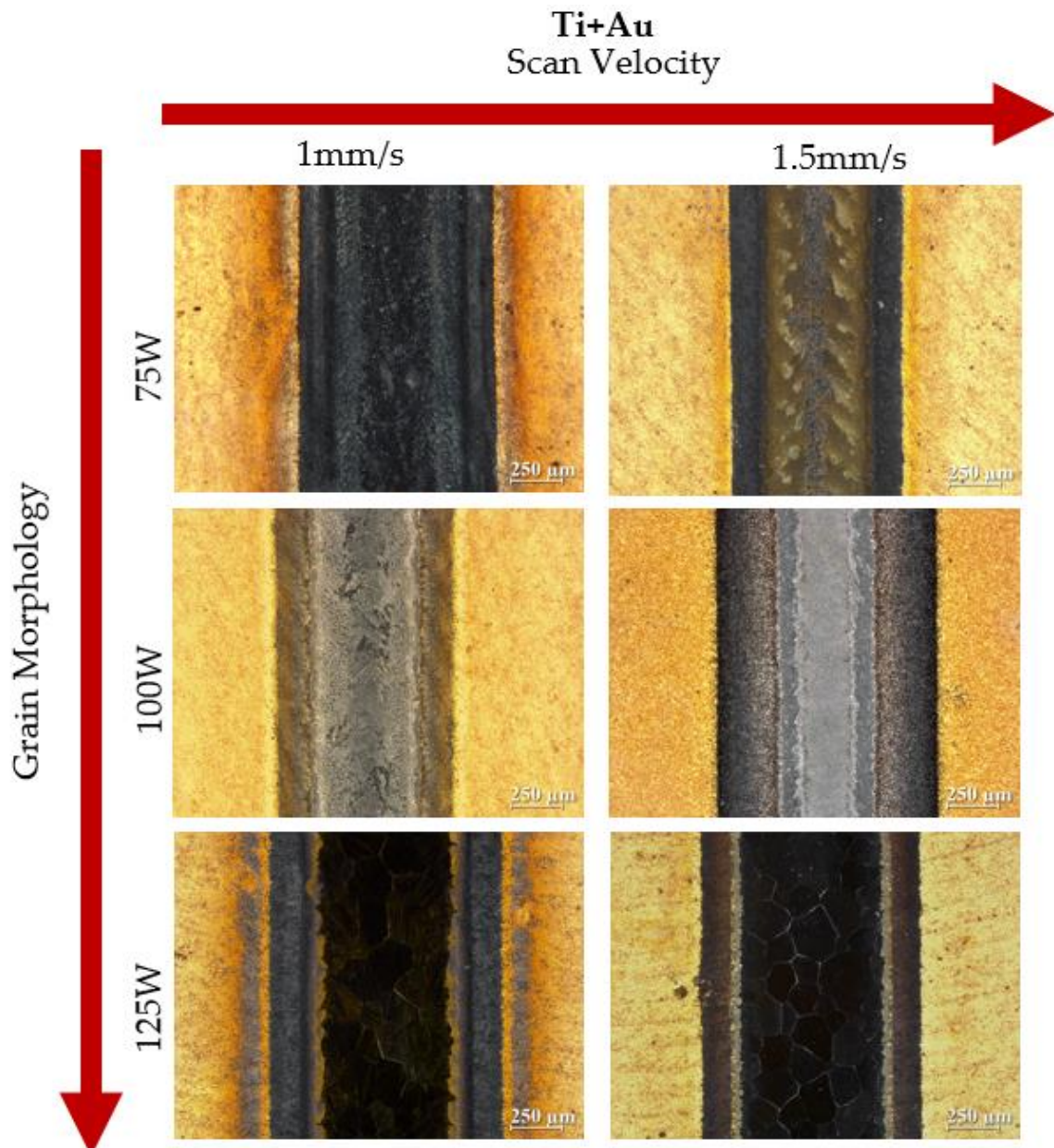


Figure 24. Light microscopy images of the surface after laser treatment in a range of process parameters carried out during process optimisation for Ti based group.

For the group of samples with a Ti13Zr13Nb substrate presented in Fig. 25, due to the different behaviour of the alloy following laser treatment, it was decided to reselect the parameters at higher speeds (2-3 mm/s) of the process parameters and the same power. In the microscopic images, a strongly fluctuating coating surface was visualised for the low-power variants (P=75W). The 100W parameters are again characterised by the highest homogeneity

and metallic shine, indicating a good combination of process parameters in these variants. The highest power used for the Ti13Zr13Nb group (P=125W) resulted in strong remelting with a significant widening of the heat affected zone.

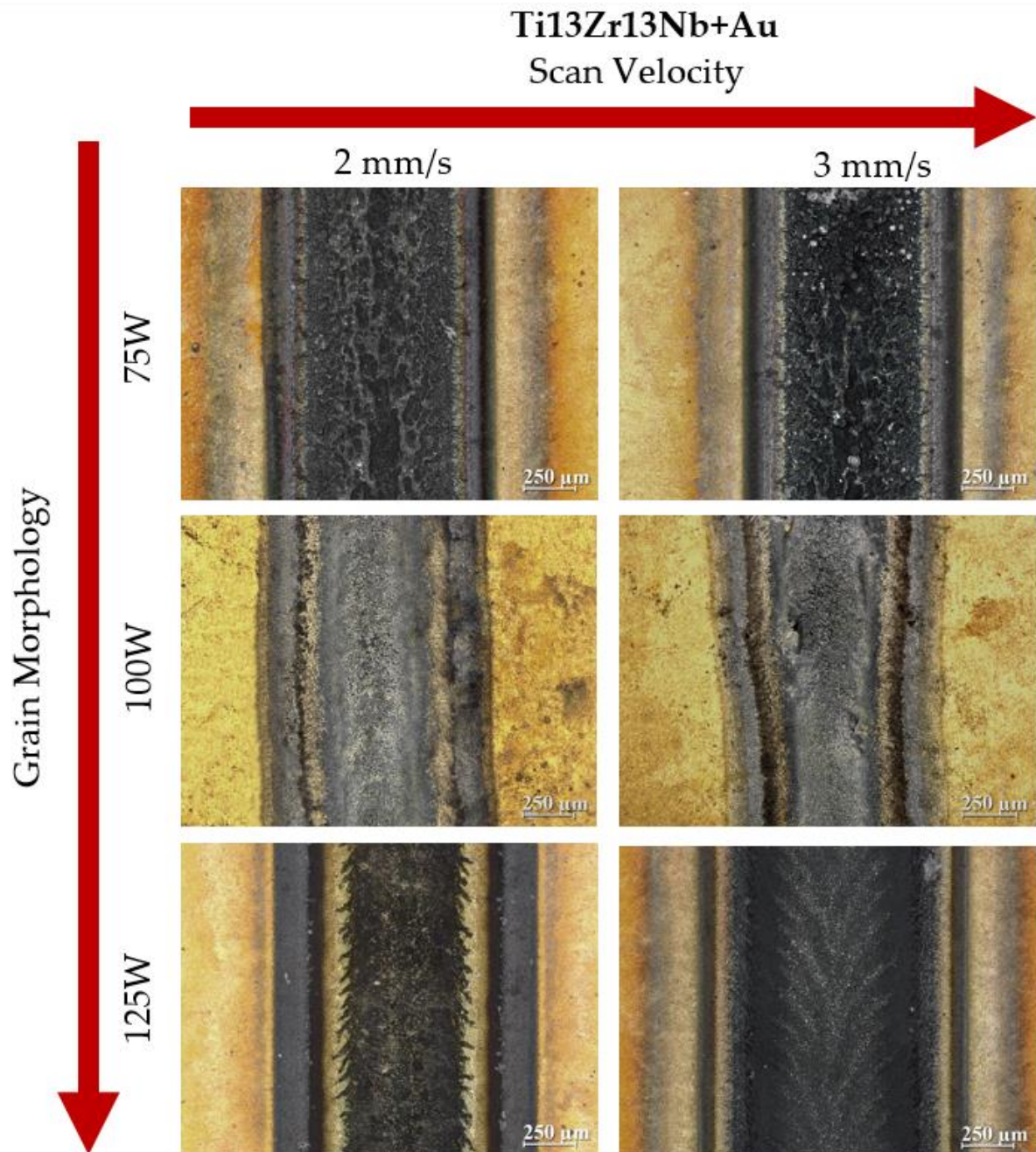


Figure 25. Light microscopy images of the surface after laser treatment in a range of process parameters carried out during process optimisation for Ti13Zr13Nb based group.

5.5 Scanning Electron Microscopy on cross sections

Scanning electron microscopy images of cross-sections for samples immediately after electrochemical deposition of gold are presented in Fig. 26. The higher roughness of the Ti+Au group results in greater unevenness. Very thin areas can be seen in the microscopic image, which allows the conclusion that the gold layer will not be perfectly tight, which, without appropriate laser treatment, will not provide improved corrosion protection (anodic protection). For the Ti₁₃Zr₁₃Nb group, the layer is much more homogeneous, facilitating a noticeable reduction in surface roughness.

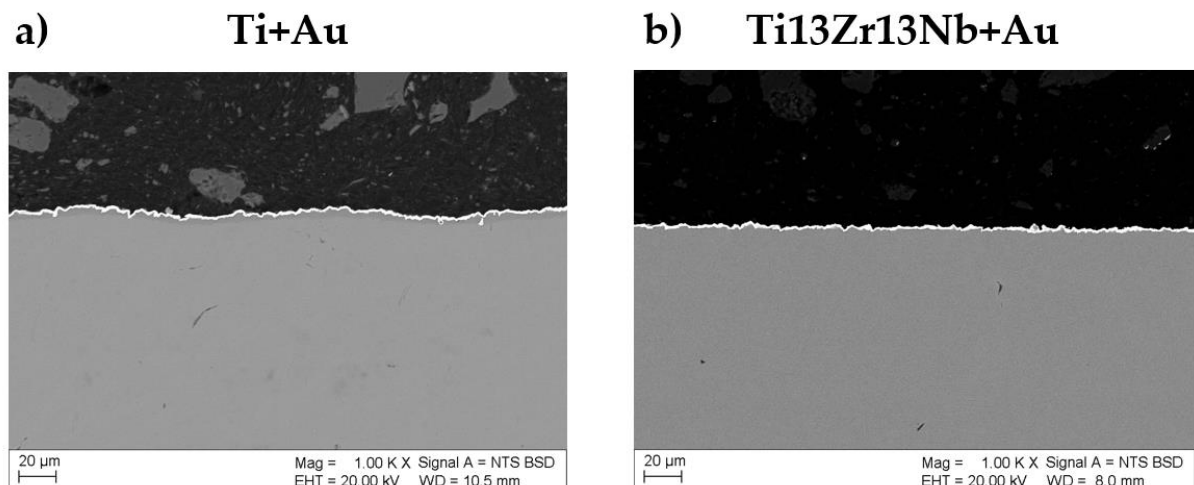


Figure 26. Scanning electron microscopy images of the cross-section of the samples after electrochemical deposition of gold on the a) Ti surface and b) Ti₁₃Zr₁₃Nb.

The cross-sections of the TiAu group samples after laser processing are presented in Fig. 27. The photos were taken using the Backscattered Electron BSE technique. Obtained images are formed by backscattered electrons which are emitted by elastic scattering of the incident (primary) electrons. A BSE images reveal the compositional difference in a specimen (difference in the average atomic number). Therefore, in the images the element with the higher atomic mass (Au) is lighter compared to the lighter one (Ti). For $P = 75\text{W}$ in both speed variants, a large unevenness of remelting zone and low penetration of gold into the Ti matrix can be noticed, which allows for immediate rejection of these process variants. In the case of parameters with the power variant $P = 125\text{W}$, the situation is reversed. Too deep penetration of gold atoms causes too little local concentration of gold atoms, which prevents the stoichiometric ratio of Ti to Au (preferably 3: 1). Therefore, it was decided to reject the 125W variants. In the case of variants with a power of $P = 100\text{ W}$ and a scan speed of $V = 1\text{ mm/s}$ and $V = 1.5\text{ mm/s}$,

the most uniform coatings were obtained. In addition, several distinct zones can be distinguished on the cross-section, indicating the formation of specific phases. The above variants were qualified for further analysis

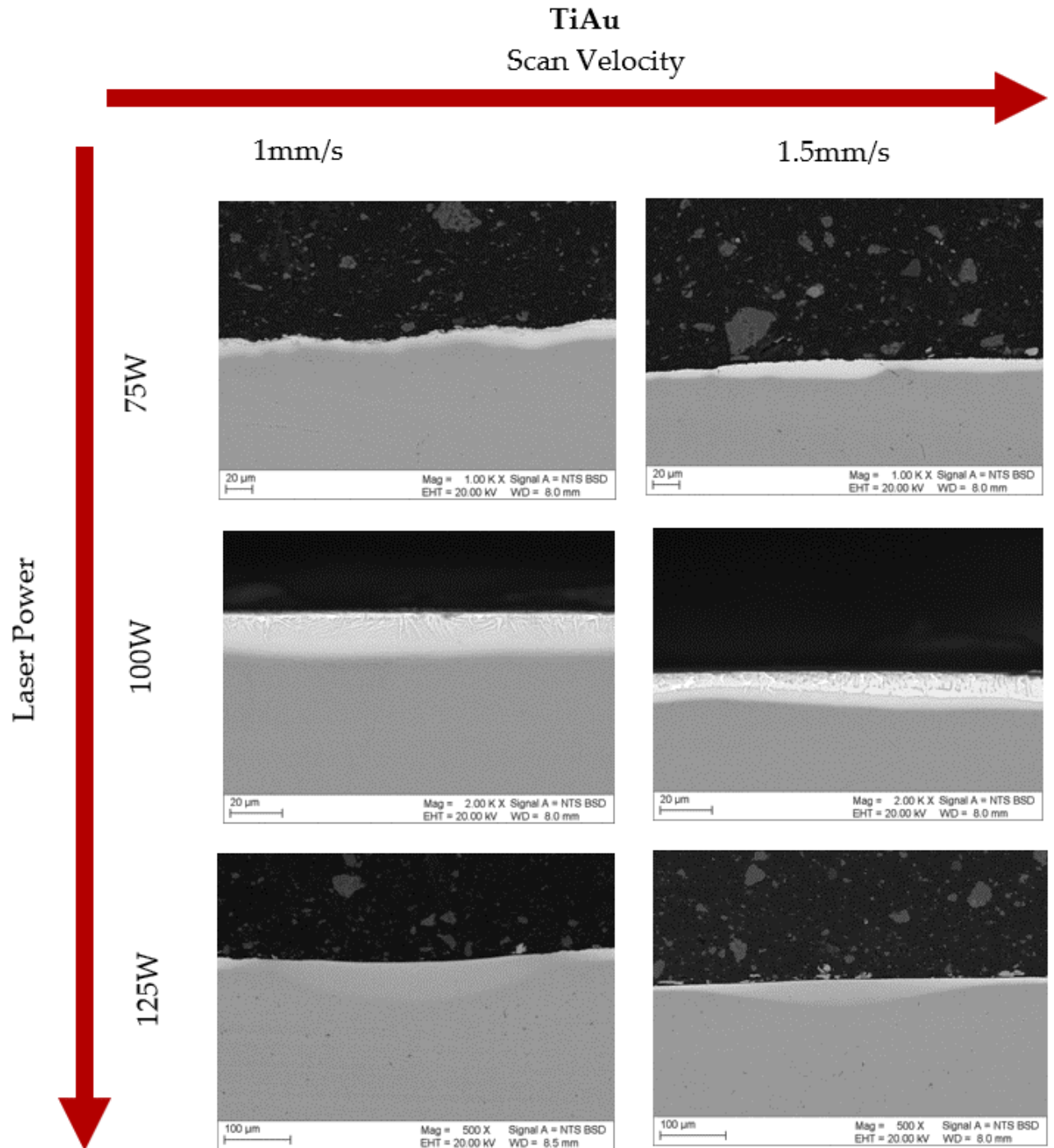


Figure 27. SEM images of the samples cross-section after laser treatment in a range of process parameters carried out during process optimisation for Ti based group.

For Ti₁₃Zr₁₃Nb based-samples, the results of the analysis using scanning electron microscopy are presented in Fig. 28. As for the Ti-substrate samples, the process parameters with the power $P = 75\text{W}$ result in uneven remelting, albeit with an indication of a more uniform remelting behaviour in the case of $V = 3\text{ mm/s}$ than 2 mm/s . In the case of 125 W power, as in the Ti substrate group, the remelting is too deep for a reasonable concentration of gold in the matrix, allowing the Ti₃Au phase to crystallize. In the case of 100W process parameters, both for the velocity $V = 2\text{ mm/s}$ and $V = 3\text{ mm/s}$, quite deep remelting ($> 10\mu\text{m}$) can be noticed and possibly greater gold distribution in the Ti matrix (this is evidenced by the lower Au signal intensity in the BSD image). However, on the surface, a strong, bright signal can be seen. It was decided again to select 100 W process variants for further analysis for the Ti₁₃Zr₁₃Nb substrate group.

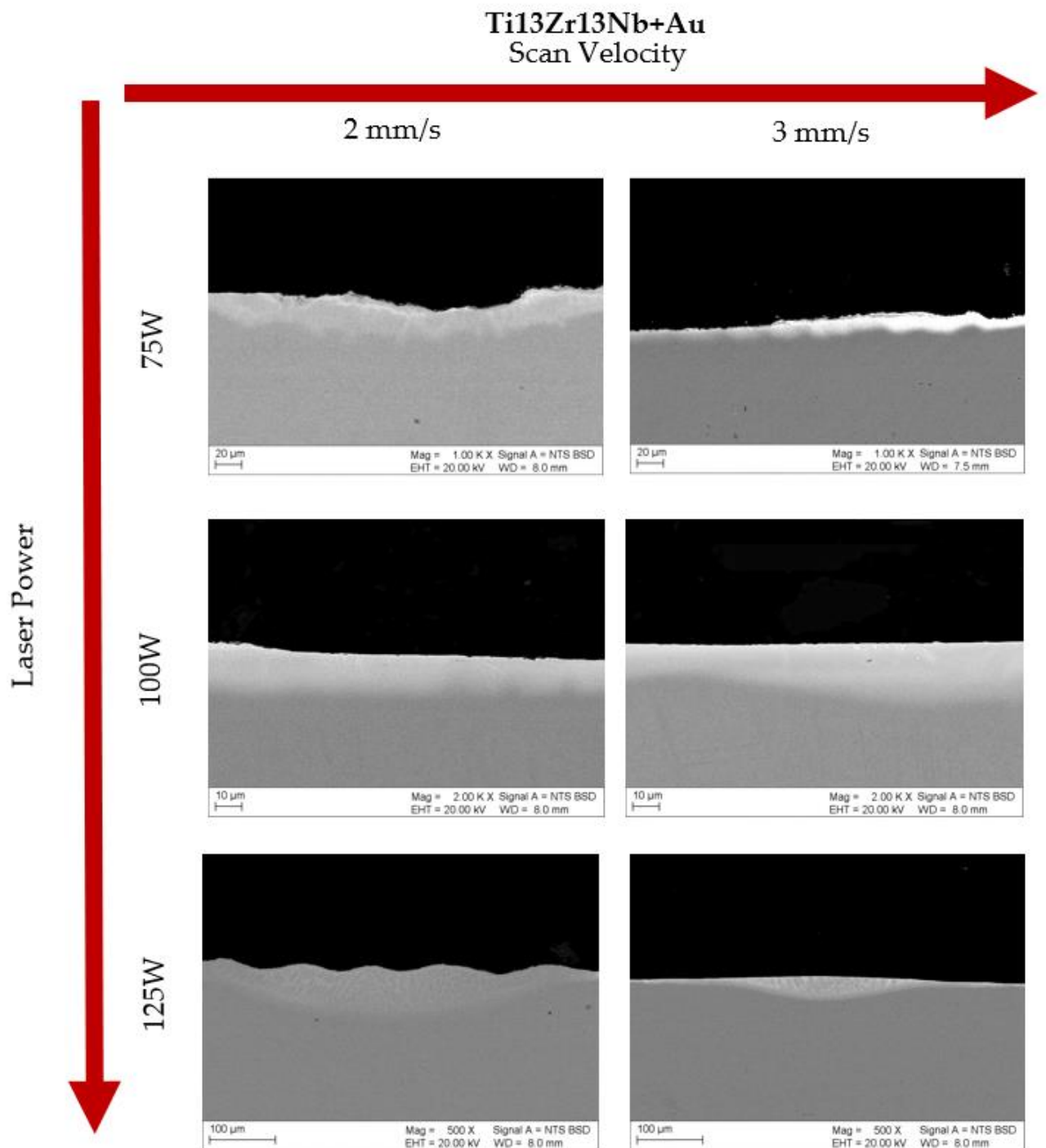


Figure 28. SEM images of the samples cross-section after laser treatment in a range of process parameters carried out during process optimisation for Ti13Zr13Nb based group.

After on-side light microscopy and SEM microscopy analysis of the cross-sections of the samples obtained for the laser power of 75-125W and the beam travel speed in the range of 1-1.5mm/s for the Ti alloy and 2-3mm/s for the Ti13Zr13Nb alloy, samples obtained using a laser

with a beam power of 100W. The selected samples are characterized by the most uniform remelting and the desired depth of not more than 20 μ m.

5.6 Energy Dispersive Spectroscopy

The results of quantitative EDS analyzes confirm changes in the chemical composition (more precisely, the concentration of chemical elements) as a result of remelting the samples TiAu 1 mm/s (Fig. 29), TiAu 1.5 mm/s (Fig. 31), Ti13Zr13NbAu 2 mm/s (Fig. 33) and i13Zr13NbAu 3 mm/s (Fig. 35). Several main areas of concentration changes can be distinguished in the presented images. For the 1 mm/s TiAu sample, there are four areas whose Au content decreases from the maximum value (approx. 21 at%) to 5 at%. In region 1, the ratio of the atomic concentration of Ti to Au is 3 to 1, as shown in Fig. 32. It is therefore the most interesting for the search for the Ti₃Au phase. Similar results were obtained for the TiAu 2 mm/s sample, where four areas with different concentrations of elements are also visible. Again, in region 1, the Ti to Au atomic concentration ratio is close to that expected for the Ti₃Au phase (Fig. 32).

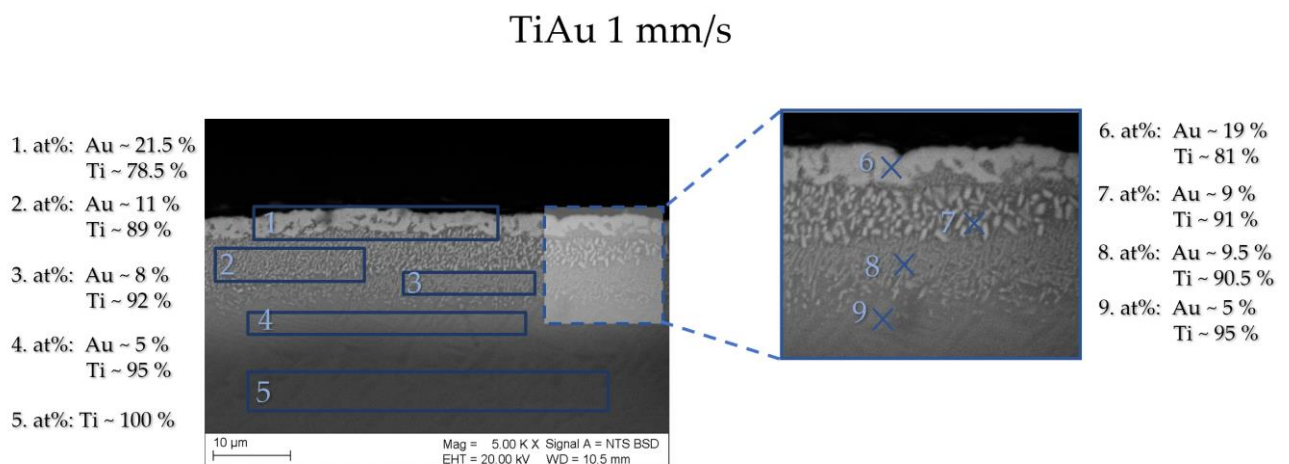


Figure 29. Quantitative EDS analysis results for the sample TiAu 1 mm/s.

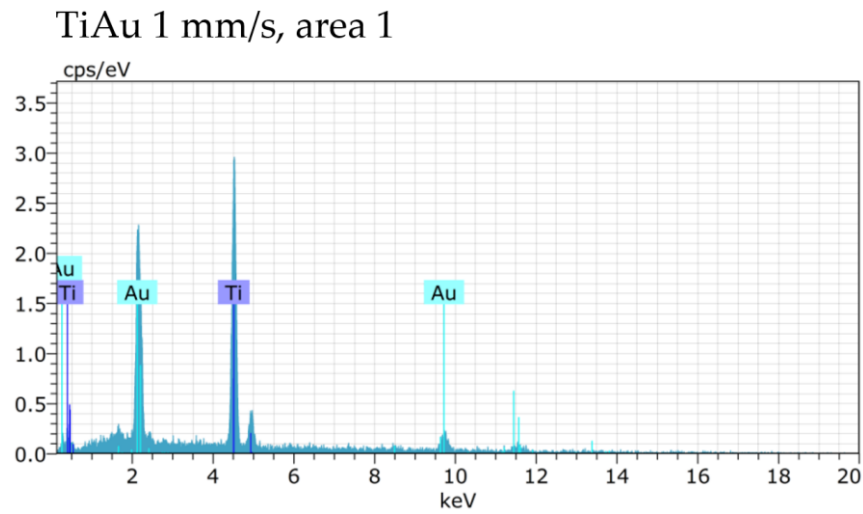


Figure 30. EDS X-ray spectrum from area 1 of Fig. 29.

TiAu 1.5mm/s

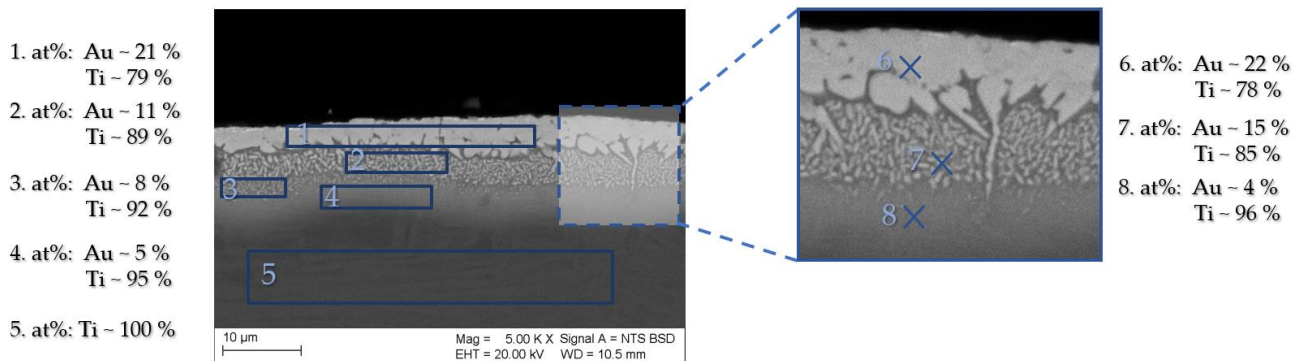


Figure 31. Quantitative EDS analysis results for the sample TiAu 1.5 mm/s.

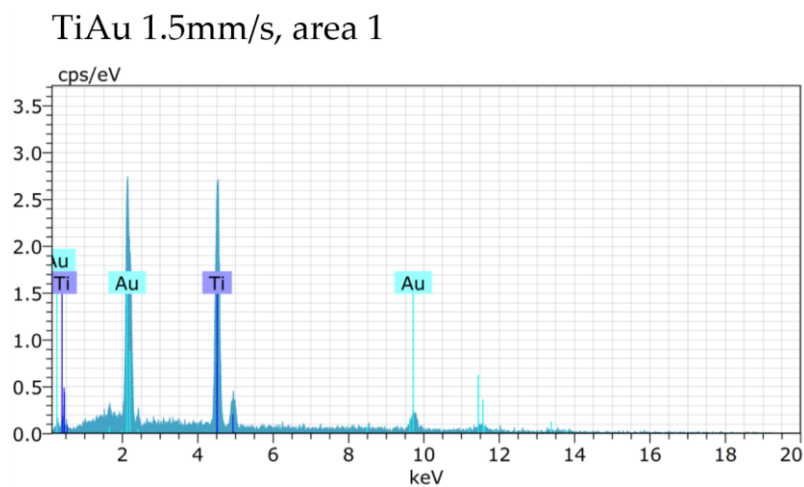


Figure 32. EDS X-ray spectrum from area 1 of Fig. 31.

In the case of a group of samples based on Ti₁₃Zr₁₃Nb, the changes are more heterogeneous, and the areas with a similar concentration of Au are more difficult to determine. For the Ti₁₃Zr₁₃NbAu 2 mm/s sample, there are three areas whose Au content decreases from the maximum value (approx. 14 at%) to 4 at%. Figure 34 shows the EDS spectrum obtained for region 1. For the Ti₁₃Zr₁₃NbAu 3 mm/s sample, there are only two areas. Au content in them is approximately 15 at. % (Fig. 36) and about 7 at. %.

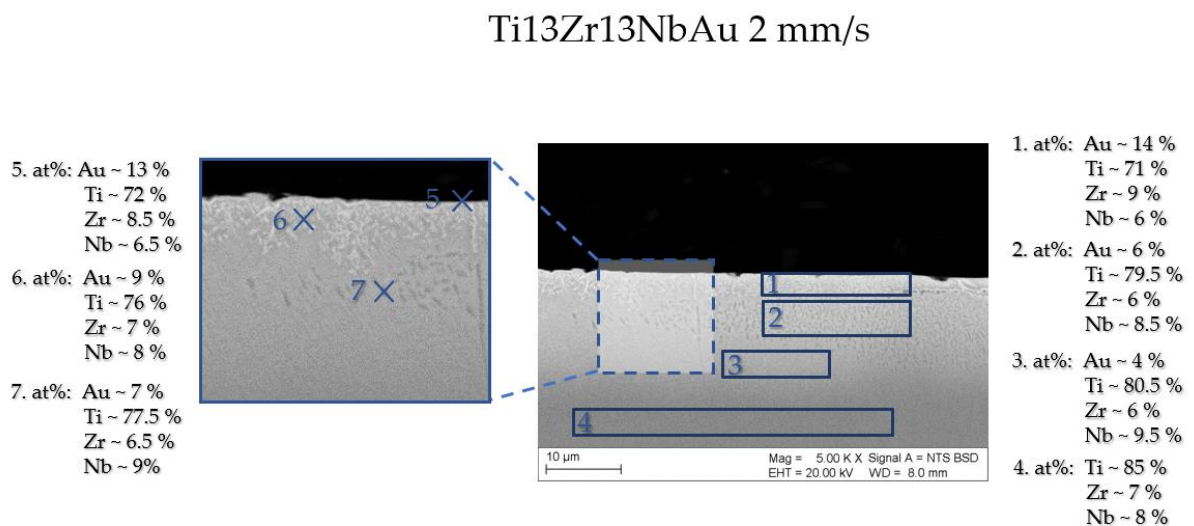


Figure 33. Quantitative EDS analysis results for the sample Ti₁₃Zr₁₃NbAu 2 mm/s.

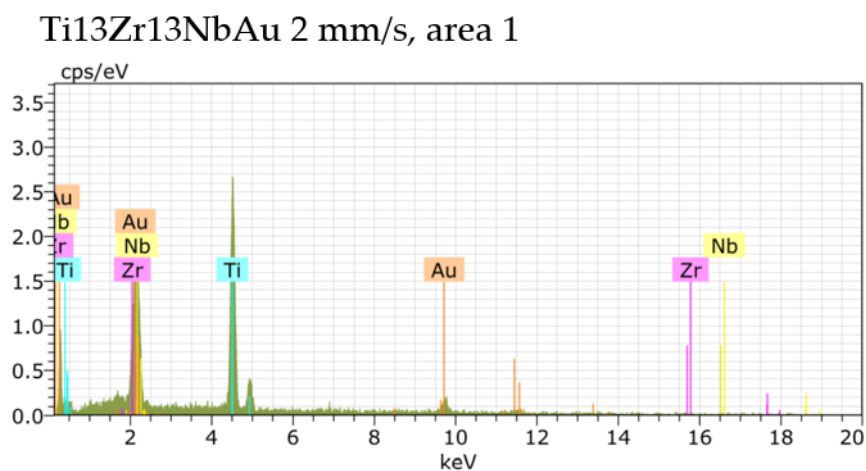


Figure 34. EDS X-ray spectrum from area 1 of Fig. 33.

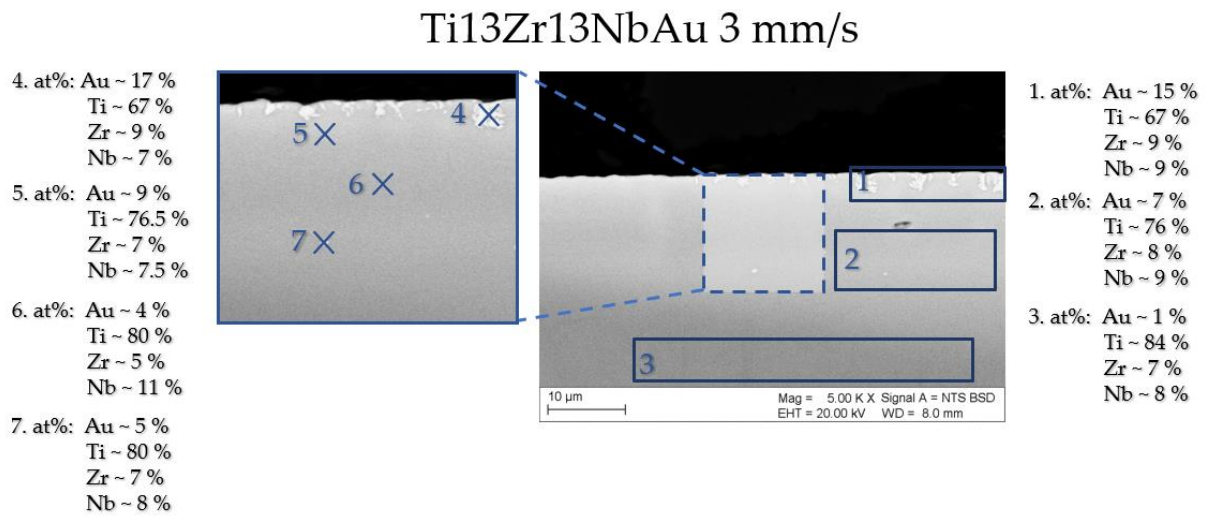


Figure 35. Quantitative EDS analysis results for the sample Ti13Zr13NbAu 3 mm/s.

Ti13Zr13NbAu 3 mm/s, area 1

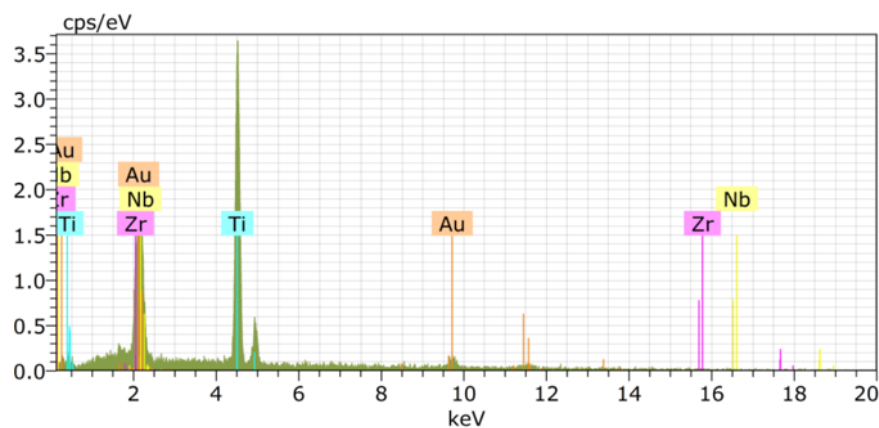
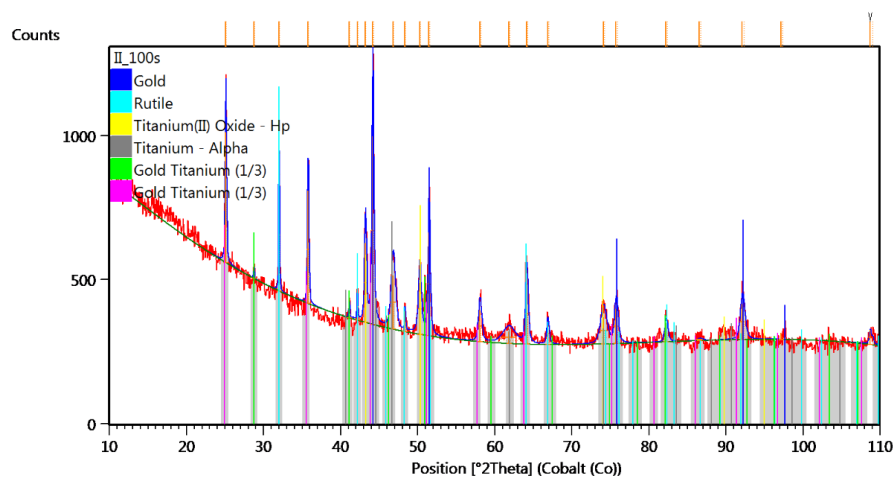


Figure 36. EDS X-ray spectrum from area 1 of Fig. 35.

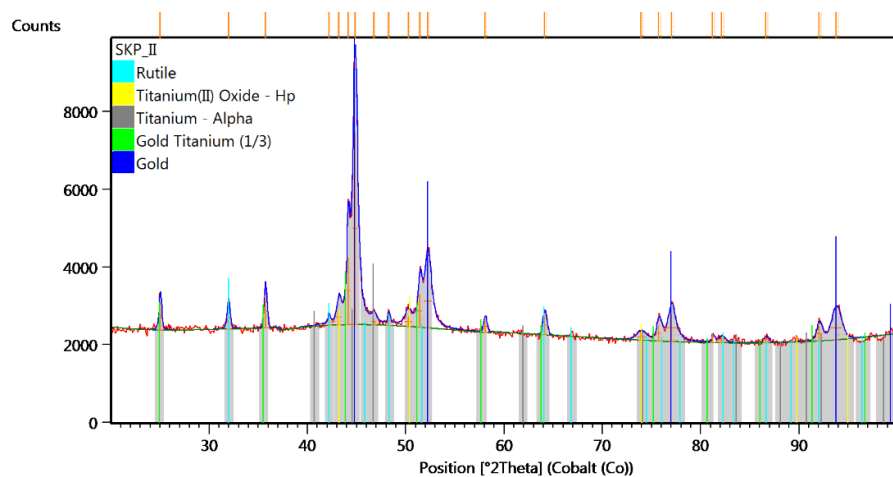
5.7 XRD

XRD analysis were performed for TiAu 1mm/s (Fig. 37) and TiAu 1.5 mm/s (Fig. 38) and for Ti13Zr13NbAu 2mm/s (Fig. 39) and Ti13Zr13NbAu 3m/s (Fig. 40). In each case P = 100W. In order to confirm the presence of the Ti₃Au phase, a qualitative analysis was performed by X-ray diffraction. Measurements made for the 1 mm/s TiAu sample (Fig. 37a, 38a) confirmed the presence of the Au phase (Cubic, space group: Fm -3m), as well as α-Ti (Hexagonal, space group: P63/mmc), titanium (II) oxide (Hexagonal, space group: P-3m1), titanium (IV) oxide -

rutile (Tetragonal, space group: P42/mmm) and the intermetallic phase β -Ti₃Au (Cubic, two space groups: Pm-3m and Pm-3n). The results obtained with GID (Fig. 37b, 38b) did not reveal the presence of the β -Ti₃Au phase (Cubic, space group: Pm-3m), which is due to the limited X-ray penetration in this geometry. This means that the intermetallic phase with the space group Pm-3n crystallizes on the gold side and is therefore identified. The phase with the space group Pm-3m, due to crystallization on the titanium side, is located deeper and has not been identified in the GID geometry.

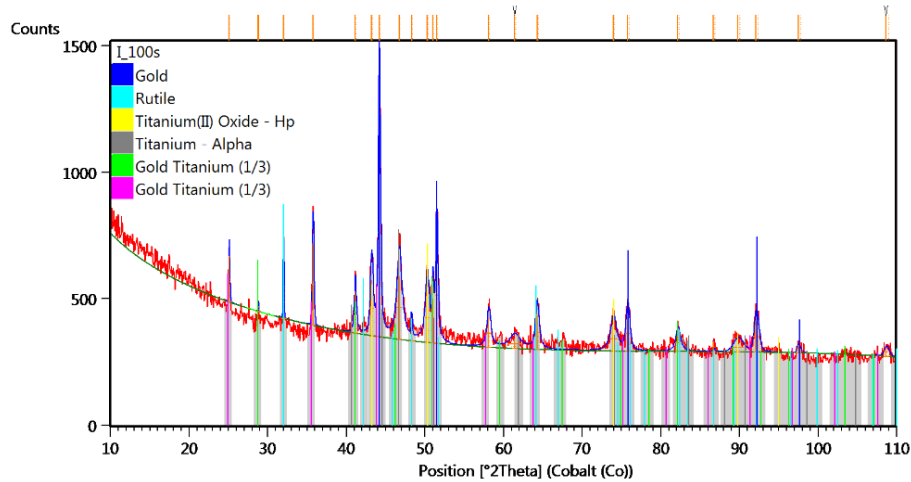


a)

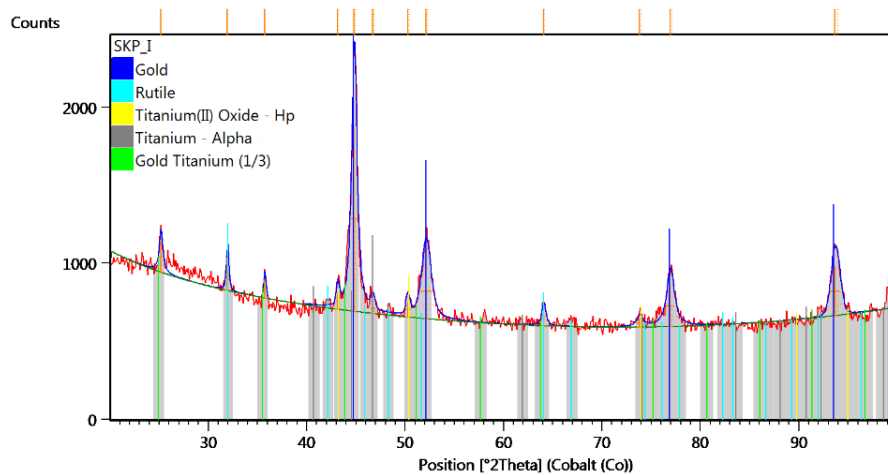


b)

Figure 37. XRD analysis results of sample TiAu 1mm/s: a) 2 θ Bragg-Brentano geometry, b) Grazing Incidence Diffraction (GID) geometry.



a)

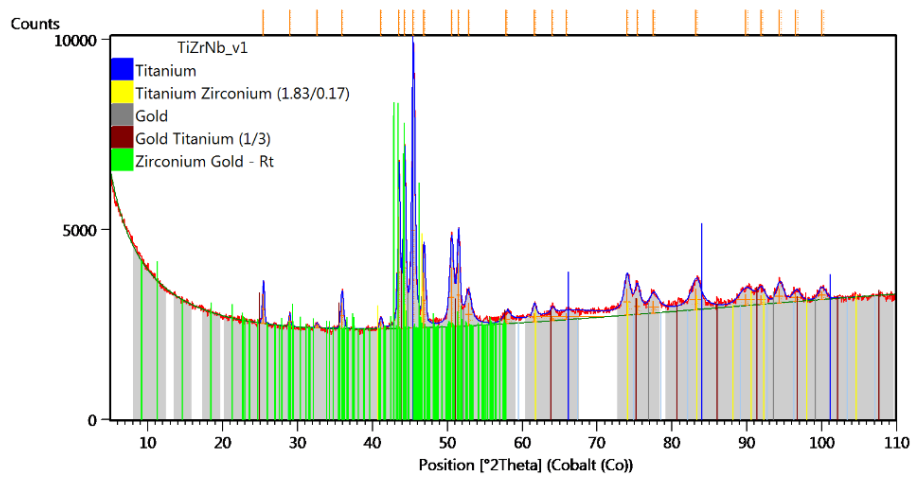


b)

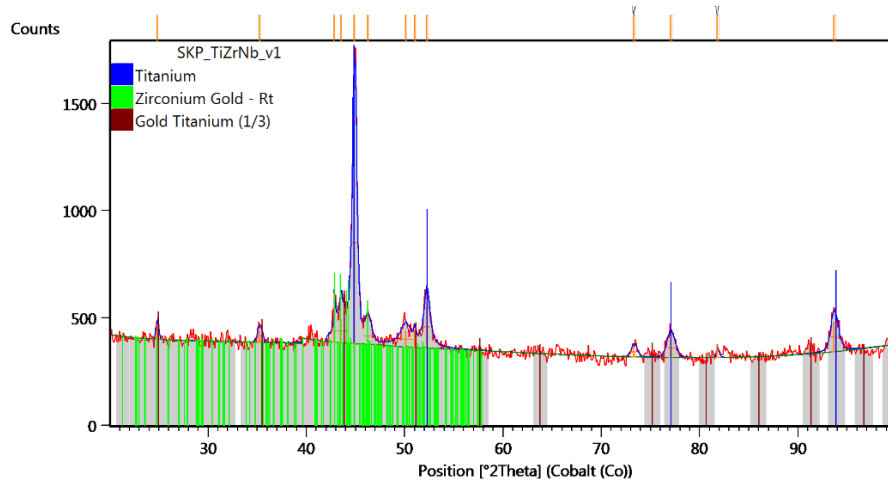
Figure 38. XRD analysis results of sample TiAu 1.5 mm/s: a) 2 θ Bragg-Brentano geometry, b) Grazing Incidence Diffraction (GID) geometry.

Fig. 39 and Fig. 40 show the results of the phase analysis for a group of samples based on Ti₁₃Zr₁₃Nb. XRD measurements confirmed the presence of Au phase (Cubic, space group: Fm-3m), as well as α -Ti (Hexagonal, space group: P63/mmc), Titanium (II) Oxide (Hexagonal, space group: P-3m1), Zirconium Gold (Anorthic, space group: P-1,2), Zirconium Titanate (Orthorhombic, space group: Pbcn) and β -Ti₃Au intermetallic phase crystallized in cubic crystal system (space group: Pm-3m).

The results obtained with the GID geometry (Fig. 39b, 40b) did not reveal the presence of the Zirconium Titanate phase, which is a result of limited X-ray penetration in this measurement geometry. The absence of the Au phase in the GID diffraction patterns is probably due to the greater remelting/deeper penetration of gold atoms into the Ti₁₃Zr₁₃Nb matrix, which is also confirmed by SEM imaging on cross-sections. The presence of Zirconium Titanate for measurements in the Bragg-Brentano geometry is understandable because it is located inside the Ti₁₃Zr₁₃Nb matrix and deeper X-ray penetration is needed to identify it.

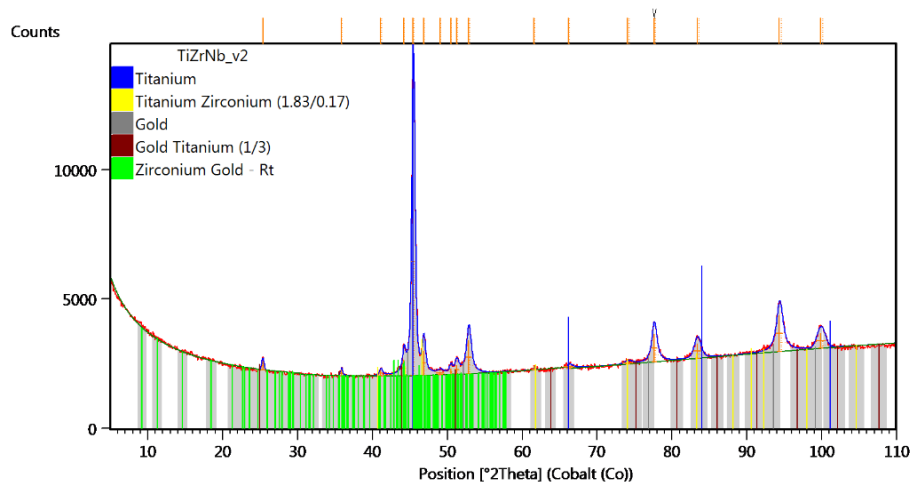


a)

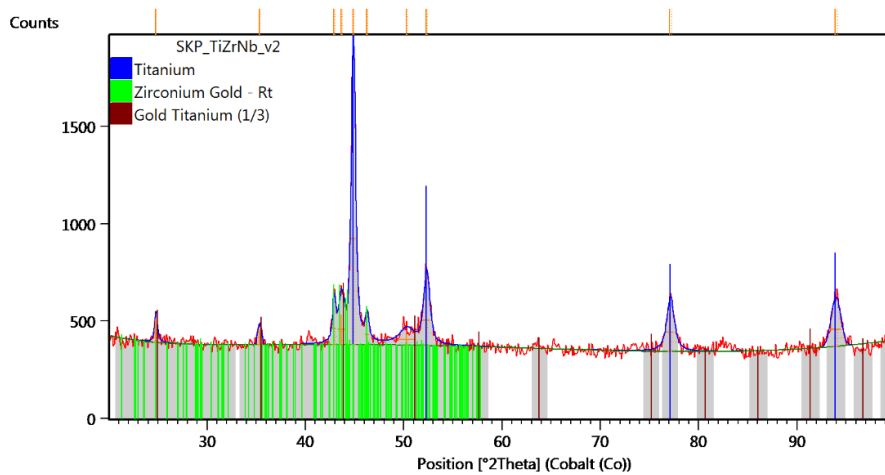


b)

Figure 39. XRD analysis results of sample Ti₁₃Zr₁₃NbAu 2mm/s: a) 2θ Bragg-Brentano geometry, b) Grazing Incidence Diffraction (GID) geometry.



a)



b)

Figure 40. XRD analysis results of sample Ti₁₃Zr₁₃NbAu 3mm/s: a) 2 θ Bragg-Brentano geometry, b) Grazing Incidence Diffraction (GID) geometry.

5.8 EBSD

In order to assess the microstructure, phase composition, grain size and orientation, the samples were subjected to EBSD analysis. Fig. 41 shows Image Quality (IQ) maps and phase maps for TiAu 1 mm/s and TiAu 1.5 mm/s samples. They represent an area of approximately 10 μm x 10 μm . The area for analysis was selected on the basis of the EDS test results, i.e. homogeneous in terms of the concentration of elements and the closest to the stoichiometric

content of the Ti_3Au phase. For TiAu, it was region 1, located near the surface. The EBSD results confirm the presence of large Ti grains and smaller Au grains, which is consistent with the XRD results. In addition, small crystallites of the Ti_3Au phase are visible, located in the vicinity of grain boundaries of the Ti and Au phases.

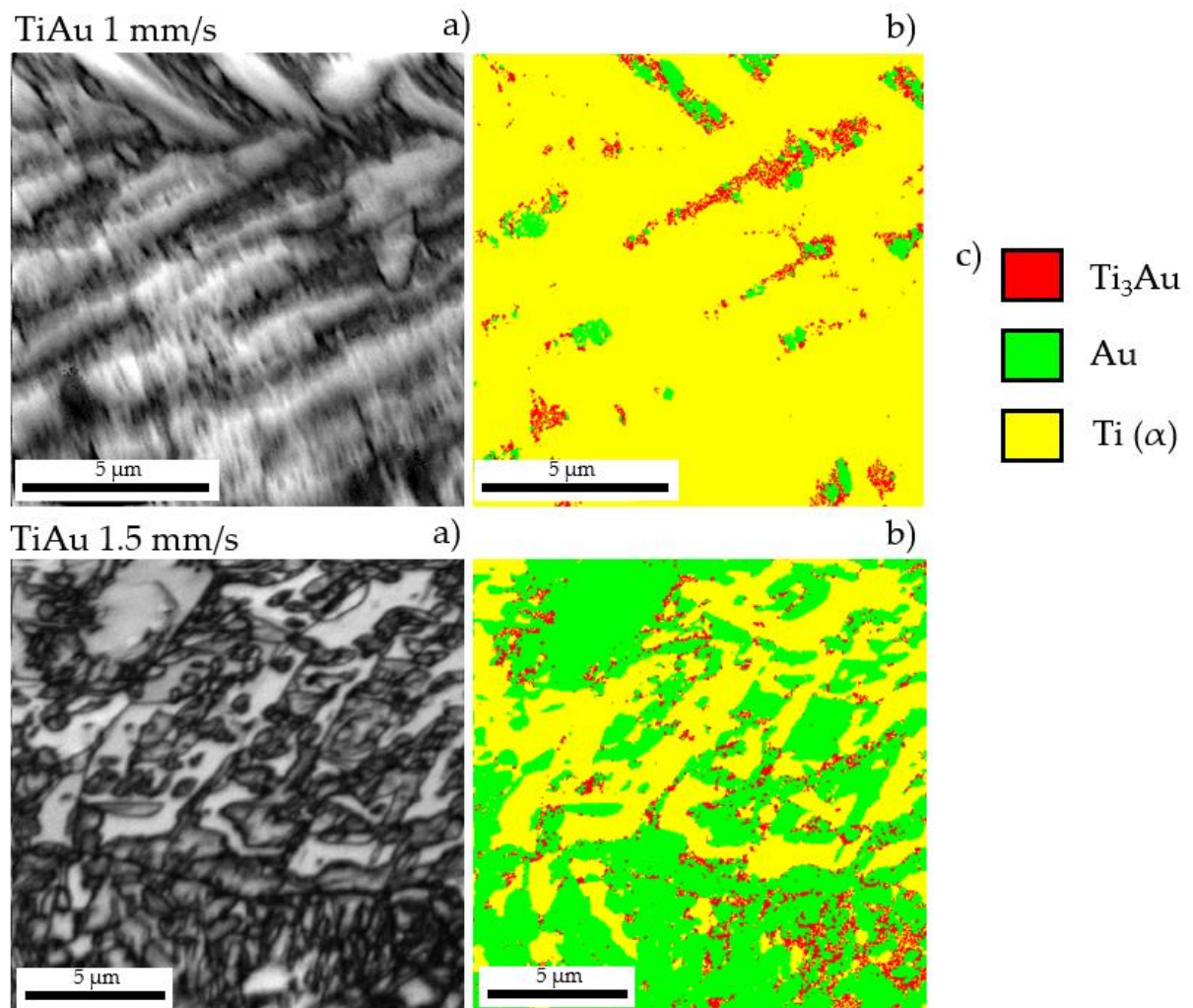


Figure 41. EBSD IQ a) and phase map b) of TiAu 1 mm/s and TiAu 1.5 mm/s

In the analyzed areas of remelting, the share of the Ti_3Au phase was 0.067 for TiAu 1.5 mm/s and 0.042 for TiAu 1 mm/s, respectively. This indicates that the process parameters used for TiAu 1 mm/s have a better effect on obtaining the Ti_3Au phase. The Ti_3Au phase is surrounded by Ti but always close to Au.

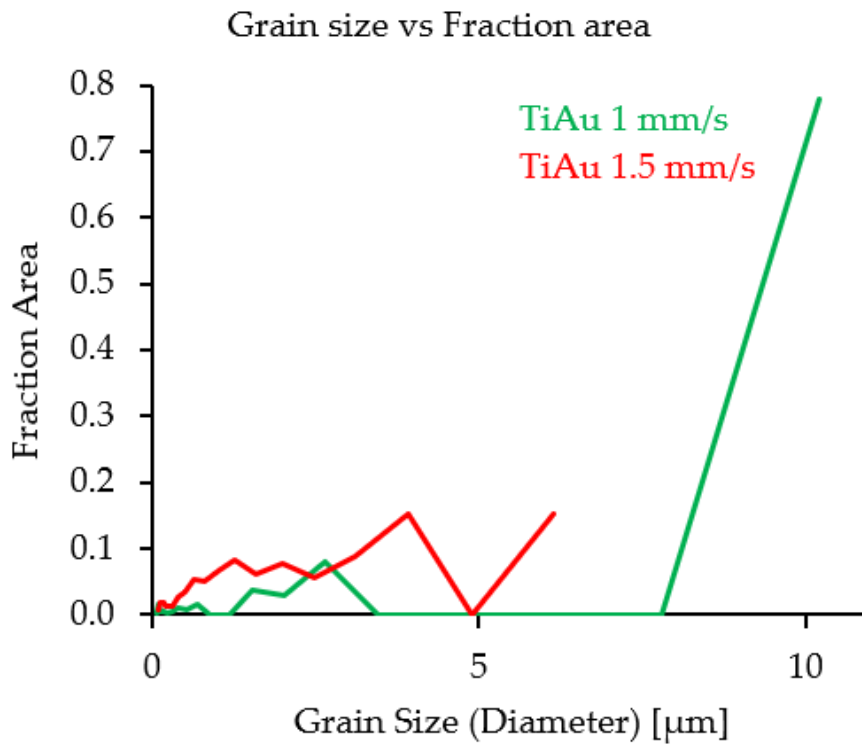


Figure 42. Grain size versus Fraction area diagram for TiAu sample group variants.

For TiAu 1.5 mm/s samples, the grain size was characterised by a smaller grain size, especially in the 1 to 5 micrometre range (Fig. 42).

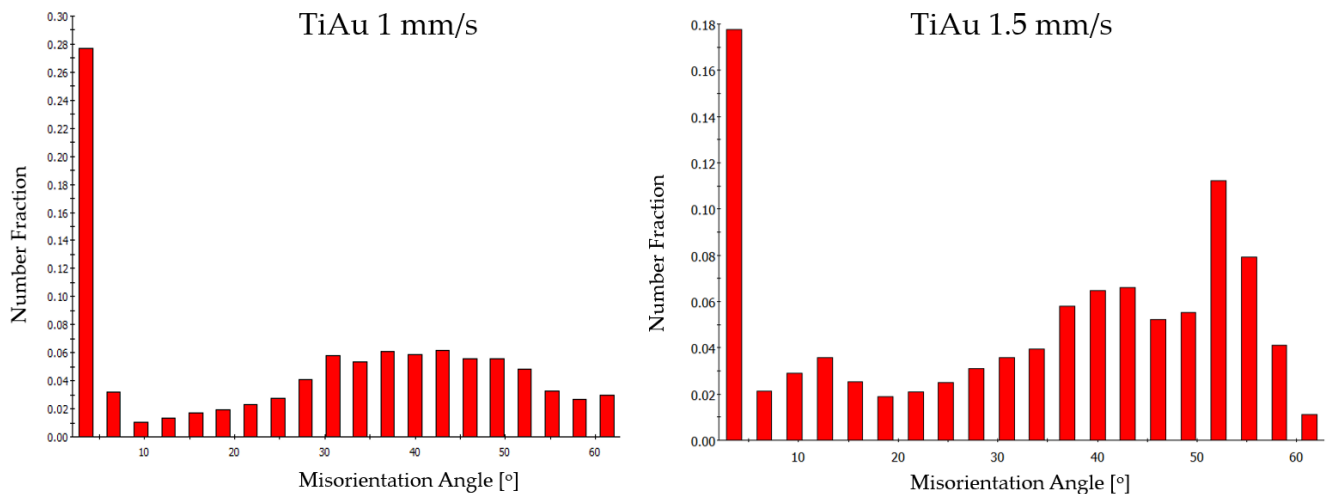


Figure 43. Misorientation Angle distribution for TiAu sample variants.

The average angle of disorientation is greater for the TiAu 1.5 mm/s samples, which is due to the greater number of boundaries in the 49-55 degrees range (Fig. 43).

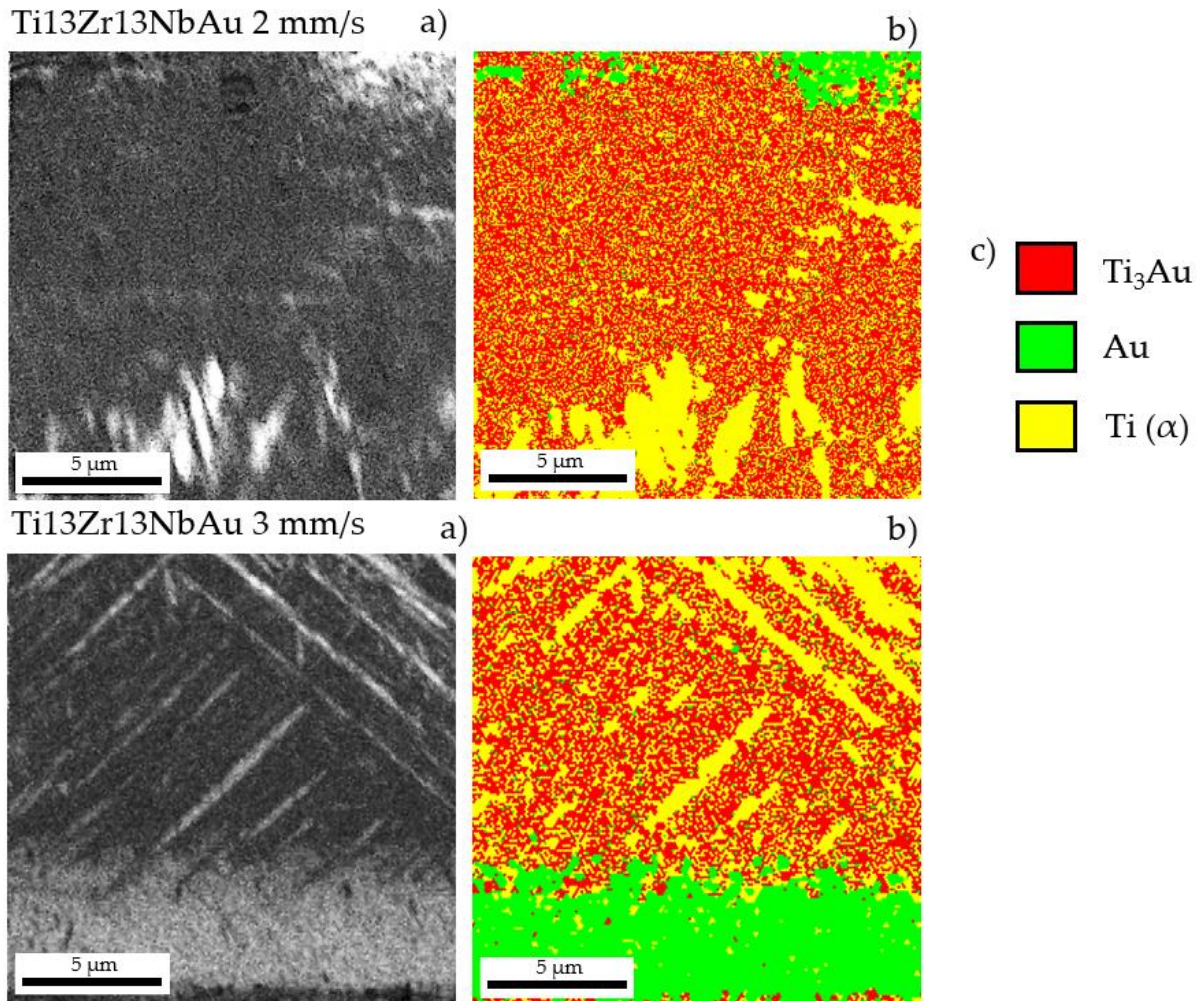


Figure 44. EBSD IQ a) and phase map b) of Ti₁₃Zr₁₃NbAu 2 mm/s and Ti₁₃Zr₁₃NbAu 3 mm/s.

For samples with Ti₁₃Zr₁₃Nb substrates, the Ti₃Au to Ti ratio is higher for the Ti₁₃Zr₁₃NbAu 2mm/s parameter. It should be noted, however, that in the case of samples containing TiZr and Au₄Zr phases (previously revealed by XRD analysis), it is not possible to distinguish between these phases and Ti₃Au on the basis of EBSD detection due to very similar lattice parameters. For cubic Ti₃Au the parameter $a = 5.097 \text{ \AA}$, for orthorhombic Zr₄Au $a = 5.0 \text{ \AA}$, $b = 4.445 \text{ \AA}$ and $c = 14.294 \text{ \AA}$, while for tetragonal TiZr $a, b = 3.11 \text{ \AA}$ and $c = 4.2 \text{ \AA}$. Such parameters do not allow unambiguous indexing of the individual phases, with the result that we are dealing with a mixture of these phases in regions indexed as Ti₃Au (Fig. 44).

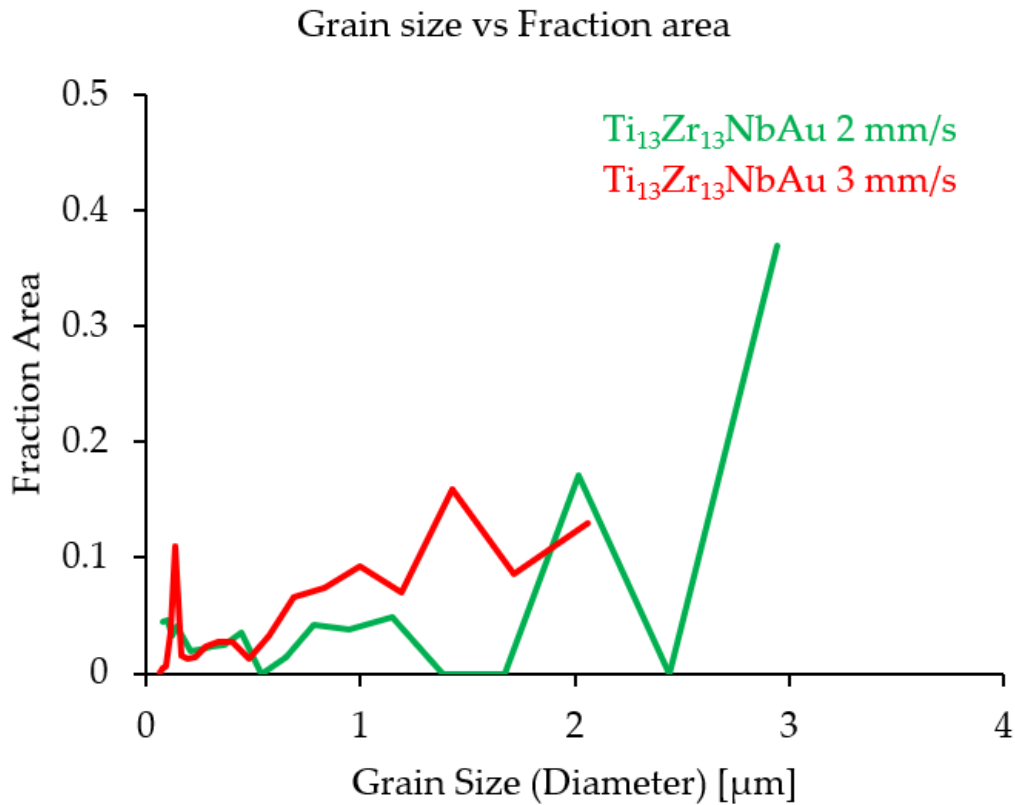


Figure 45. Grain size versus Fraction area diagram for Ti13Zr13NbAu sample group variants.

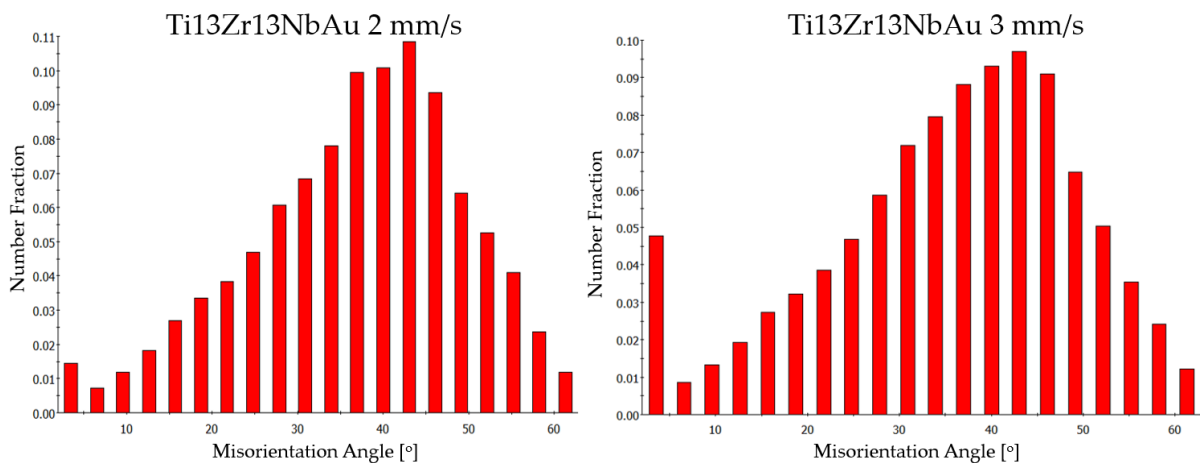


Figure 46. Misorientation Angle distribution for Ti13Zr13NbAu sample variants.

For Ti13Zr13NbAu 2 mm/s there is a significantly lower average grain size: 1.14 to 5.83 for Ti13Zr13NbAu 3 mm/s (Fig. 45). Where the samples are characterised by very similar values of the misorientation angle distributions, it suggests that Ti13Zr13NbAu 2 mm/s should have better performance properties (Fig. 46 and Tab. 10).

Based on the EBSD results, it can be concluded that the tested samples contain Ti_3Au in the case of Ti based sample group, and a mixture of Ti_3Au , $TiZr$, and Au_4Zr phases in the case of $Ti_{13}Zr_{13}Nb$ based sample group. This information can be useful for understanding the microstructure and properties of these materials. Further analysis by TEM techniques was necessary to identify the individual phases.

5.9 TEM

Following the previous investigations, analysis was carried out using transmission electron microscopy. For lamellae taken from TiAu 1 mm/s, TiAu 1.5 mm/s, $Ti_{13}Zr_{13}NbAu$ 2 mm/s and $Ti_{13}Zr_{13}NbAu$ 3 mm/s samples imaging (TEM, STEM), electron diffraction and EDS analysis were performed. TEM images obtained for TiAu 1mm/s sample (Fig. 47) and TiAu 1.5 mm/s sample (Fig. 49) are supplemented by the results of the EDS analysis (Fig. 48 and Fig. 50, respectively). In both cases, fine and uniformly distributed grains containing Au and Ti are surrounded by a Ti matrix. Grains are usually fine and elongated (100-300 nm wide). Larger grains (500-1000 nm) with the same chemical composition are more regular in shape. Grains of pure unmelted gold can also be seen in some places, but the amount of gold suggests its negligible contribution, due to its low melting point (1064 °C). Electron diffraction with the SAED selection aperture was used for phase identification. The results of experimental electron diffraction were compared with the computer simulations of diffraction pattern in determined zone axis. Obtained results confirmed the presence of the intermetallic phase $\beta-Ti_3Au$ (Cubic, space groups: $Pm-3m$ k) (Fig. 51), $\alpha-Ti$ (Hexagonal, space group: $P6_3/mmc$) (Fig. 52) and Au phase (Cubic, space group: $Fm-3m$) (Fig. 53).

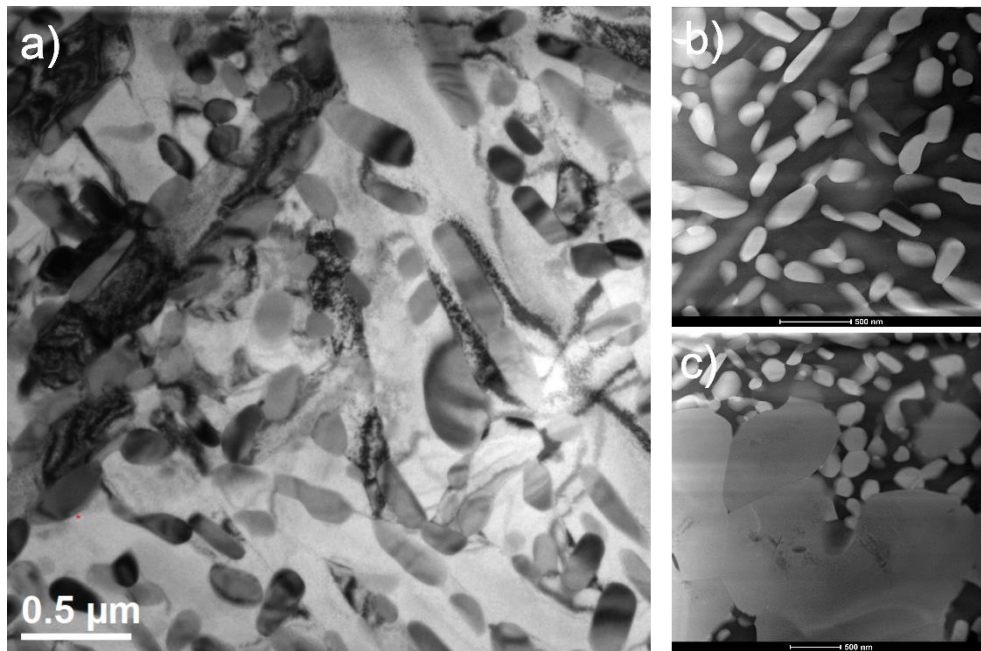


Figure 47. TiAu 1 mm/s sample structure. TEM-BF image a), STEM-HAADF images b), c).

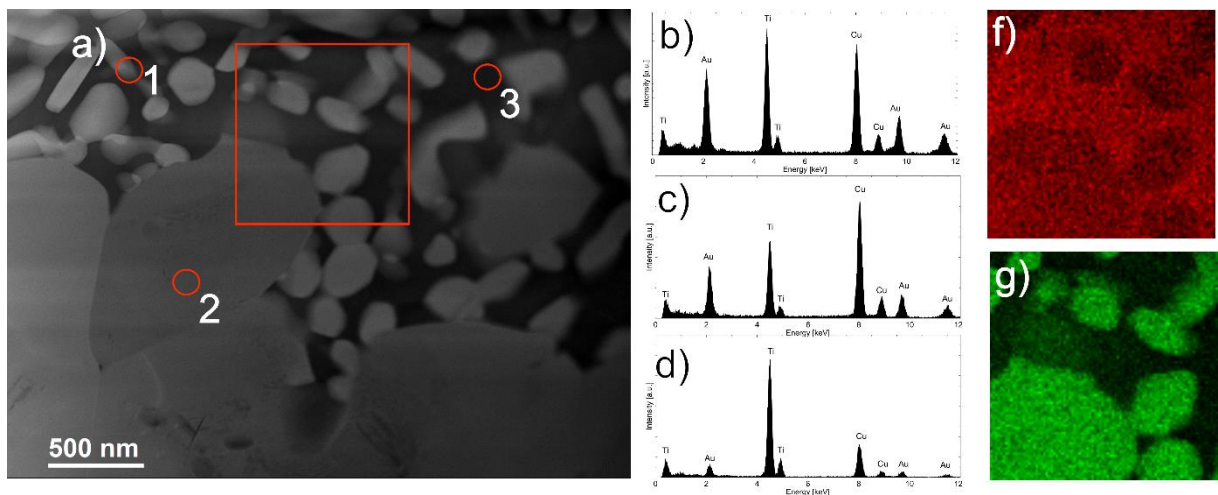


Figure 48. EDS analysis results (TiAu 1 mm/s sample). STEM-HAADF image with mapping area a) marked in red. EDS analysis result taken from area marked as 1 b), 2 c), and 3 d). EDS maps of Ti f) and Au g) taken from the square area marked in a).

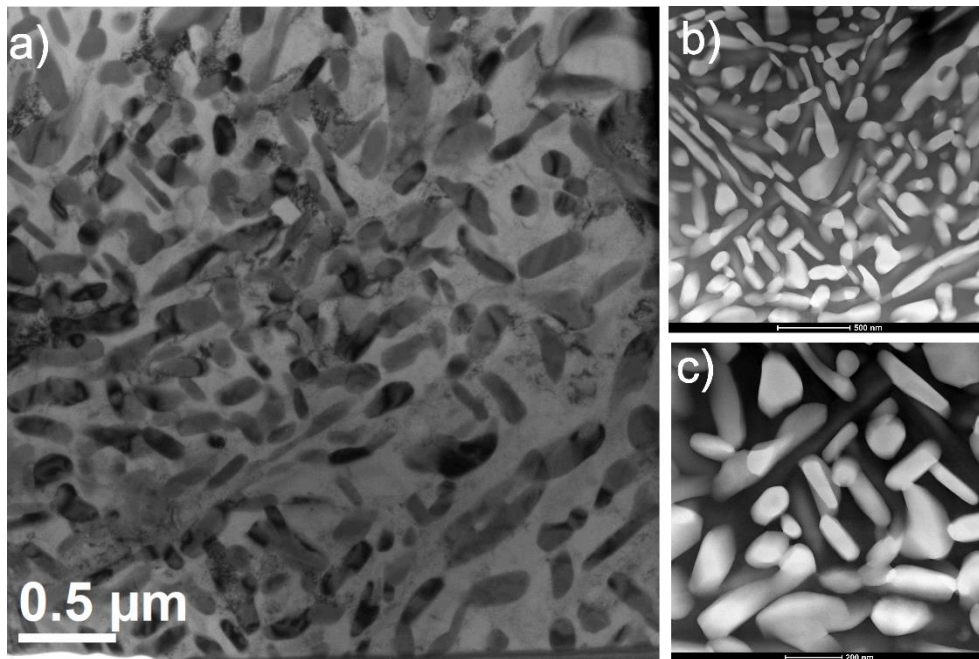


Figure 49. TiAu 1.5 mm/s sample structure. TEM-BF image a). STEM-HAADF images b), c).

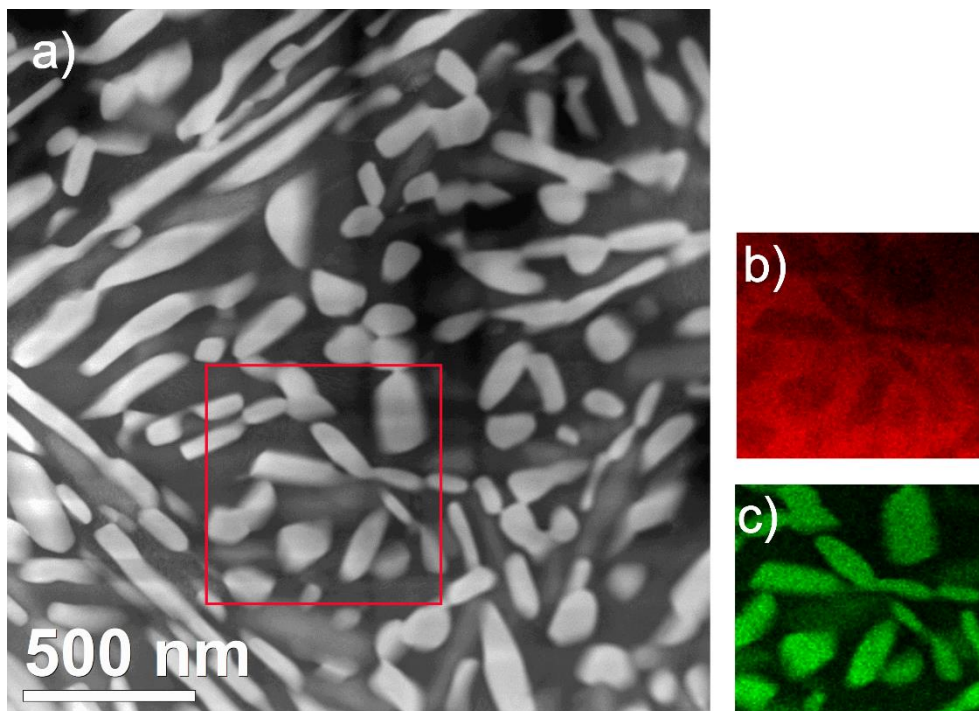


Figure 50. EDS analysis results (TiAu 1.5 mm/s sample). STEM-HAADF image with mapping area (a) marked in red. EDS maps of Ti(b) and Au(c) distribution.

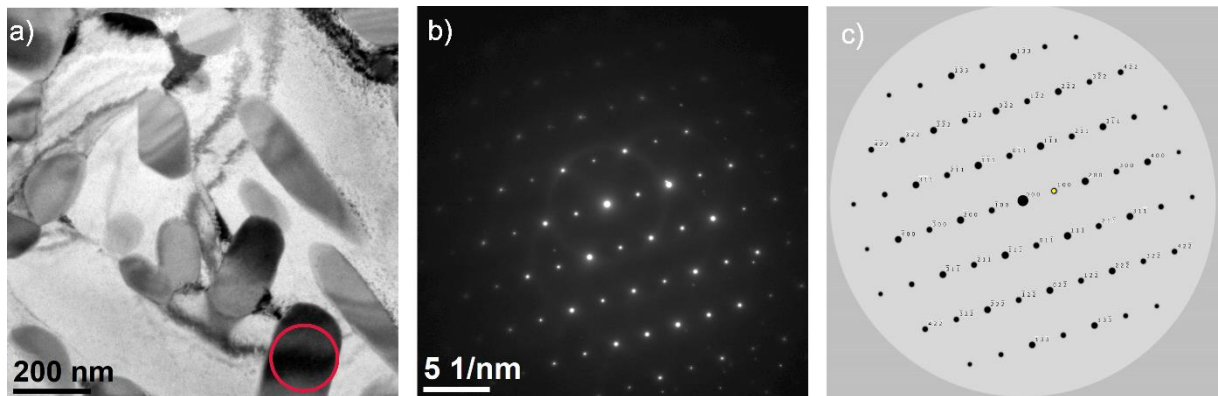


Figure 51. Ti_3Au phase (TiAu 1.5 mm/s sample). TEM-BF image with marked in red selection aperture position (a). SAED electron diffraction from the red indicated area (b). Computer simulation of the cubic Ti_3Au phase (space group $Pm-3m$) in the $[011]$ zone axis (c).

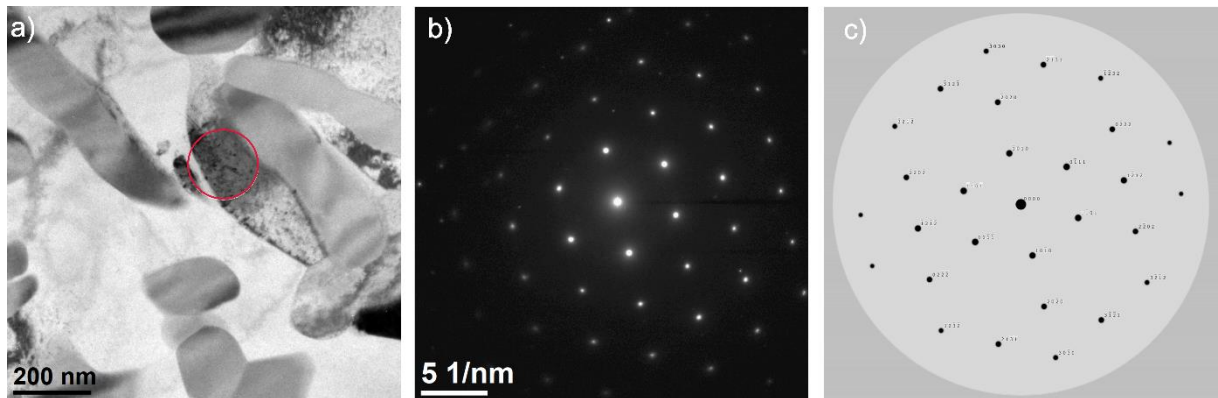


Figure 52. Ti phase (TiAu 1.5 mm/s sample). TEM-BF image with marked in red selection aperture position (a). SAED electron diffraction from the red indicated area (b). Computer simulation of the hexagonal Ti phase (space group $P63/mmc$) in the $[011]$ zone axis.

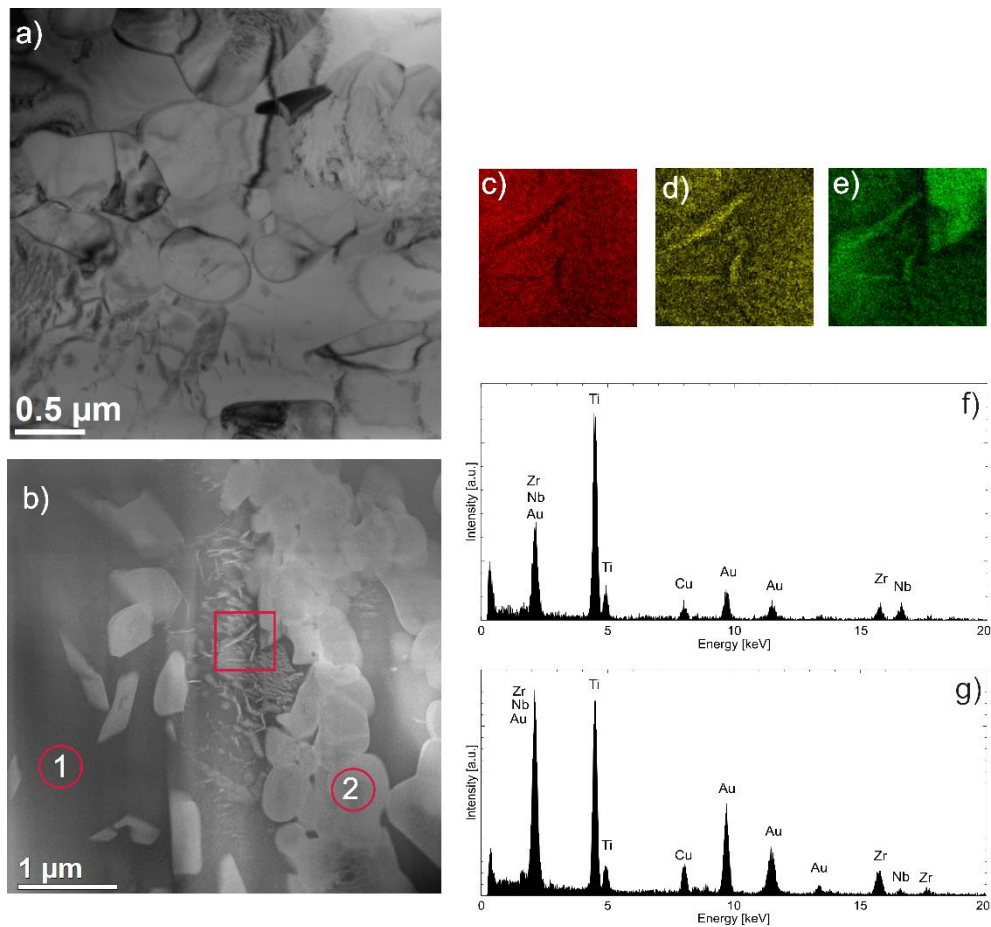


Figure 54. Ti₁₃Zr₁₃NbAu 2 mm/s sample structure. TEM-BF image a). STEM-HAADF images b). EDS maps of Ti c), Zr d) and Au e) taken from the marked square area. EDS analysis result taken from area marked as 1 f) and 2 g) in b).

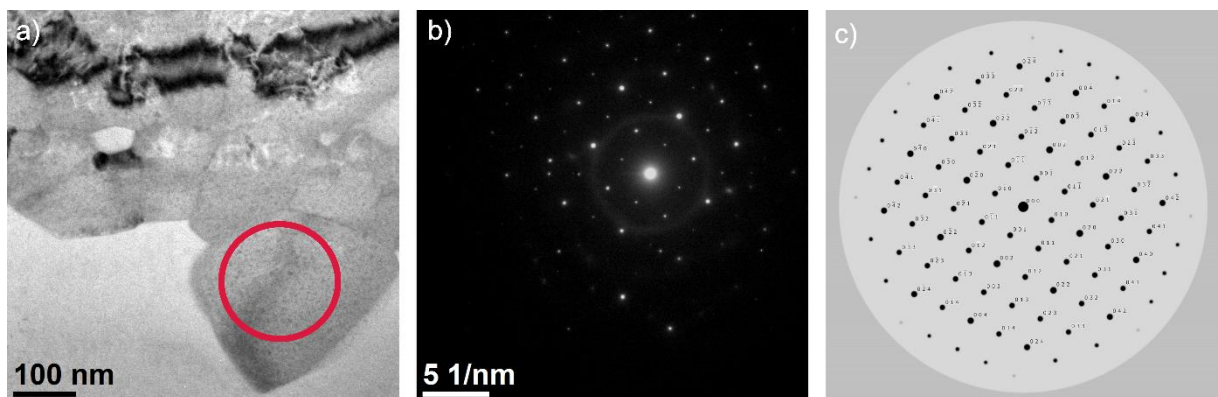


Figure 55. Ti₃Au phase structure in Ti₁₃Zr₁₃NbAu 3 mm/s sample. TEM-BF image where the position of the selection aperture is marked in red a). SAED electron diffraction from the indicated area b). Computer simulation of the Ti₃Au (Cubic, space group: Pm-3m) in [100] zone axis c).

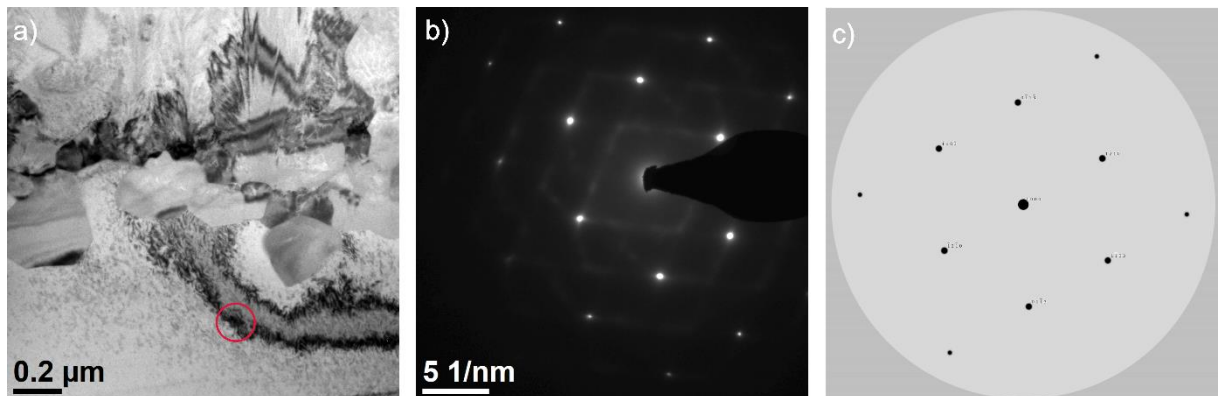


Figure 56. Ti phase structure in Ti₁₃Zr₁₃NbAu 3 mm/s sample. TEM-BF image where the position of the selection aperture is marked in red a). SAED electron diffraction from the indicated area b). Computer simulation of the Ti (hexagonal, space group: P63/mmc) in [-6-31] zone axis c).

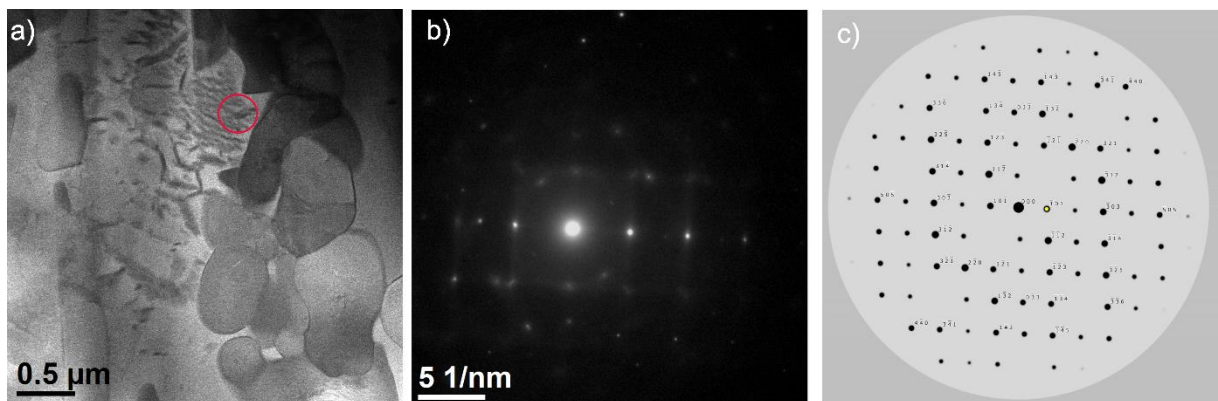


Figure 57. ZrAu₄ phase structure in Ti₁₃Zr₁₃NbAu 2 mm/s sample. STEM-BF image where the position of the selection aperture is marked in red a). SAED electron diffraction from the indicated area b). Computer simulation of the ZrAu₄ phase (Orthorhombic, space group Pnma) in [111] zone axis c).

The structural parameters of the identified phases are presented in Tab. 1

Table 9. Structural parameters of the identified phases

no.	Phase	Crystal system	Space group	Parameters of the unit cell	Reference
1	Ti ₃ Au	Cubic	Pm-3m	4.15; 4.15; 4.15 90; 90; 90	[105]
2	Au ₄ Zr	Orthorhombic	Pnma	5.01; 4.45; 14.29; 90; 90; 90	[106]
3	Ti	Hexagonal	P3/mmc	2.95; 2.95; 4.686 90; 90; 120	[107]
4	Au	Cubic	Fm-3m	4.08; 4.08; 4.08 90; 90; 90	[107]

5.10 AFM

AFM studies were carried out on the samples after etching, immediately before the electrochemical deposition of the gold coating onto the material, as well as after the coating had been applied. Analysis was also carried out for each of the selected laser treatment parameters (presented on Fig. 58, 59). Fig. 60 shows, that for samples with a Ti substrate, a decrease in the average roughness (Ra factor) can be observed respectively after each stage of material fabrication, i.e. from an initial value of Ra = 0.93 μm , after coating application there is a decrease in roughness to approximately Ra = 0.88 μm . Thereafter, both laser treatment variants decrease the Ra values to approximately 0.63 μm . Interestingly, the roughness results for samples with a Ti₁₃Zr₁₃Nb substrate increase from an initial Ra = 0.59 μm after etching to 0.81 μm . After laser treatment, the roughness decreases again to 0.57 μm for Ti₁₃Zr₁₃NbAu 2mm/s and 0.78 μm for Ti₁₃Zr₁₃NbAu 3 mm/s, respectively. With regards to roughness, the most important finding of the analysis is that the samples tested (in no variant and at no stage) exceeded a maximum value of $1.04 \pm 0.45 \mu\text{m}$ [81], corresponding to the natural roughness of the coronary vessel.

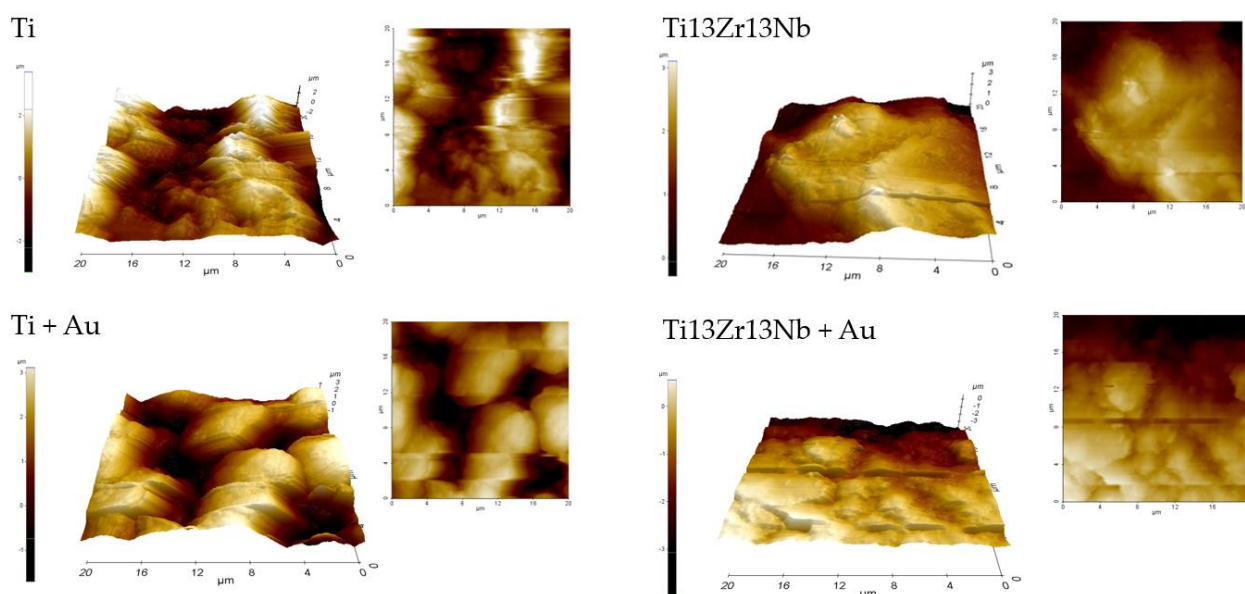


Figure 58. AFM 3D images reconstruction before applying coating (Ti, Ti₁₃Zr₁₃Nb) and after electrochemical process (Ti + Au, Ti₁₃Zr₁₃Nb + Au).

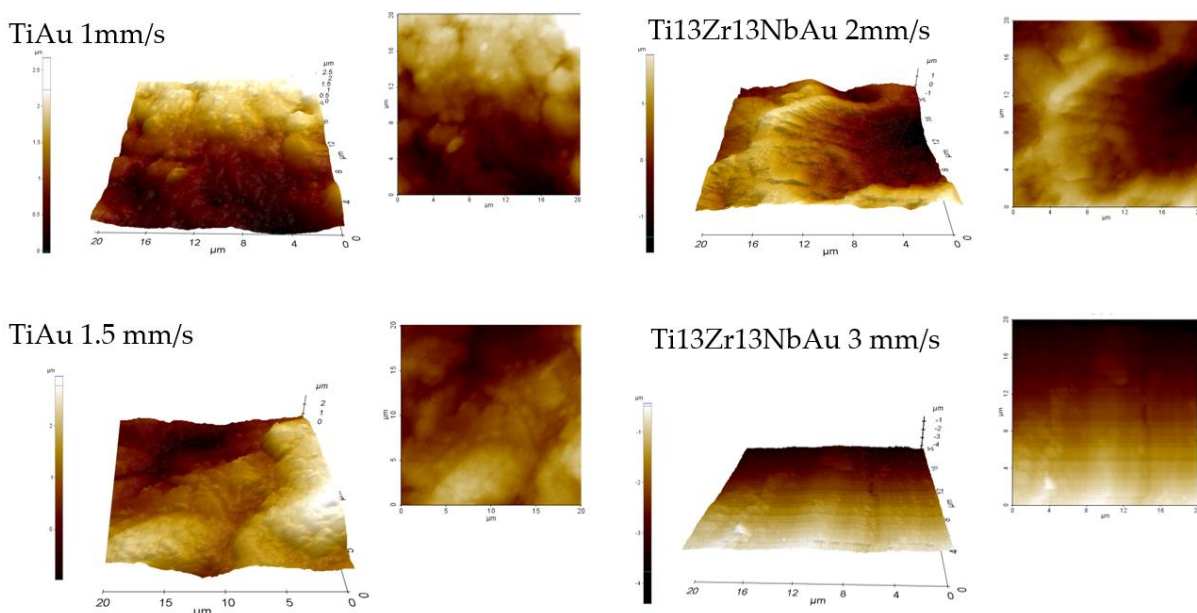


Figure 59. AFM 3D images reconstruction after laser machining for each variant selected for further analysis (TiAu 1 mm/s, TiAu 1.5 mm/s, Ti₁₃Zr₁₃NbAu 2 mm/s, Ti₁₃Zr₁₃NbAu 3 mm/s).

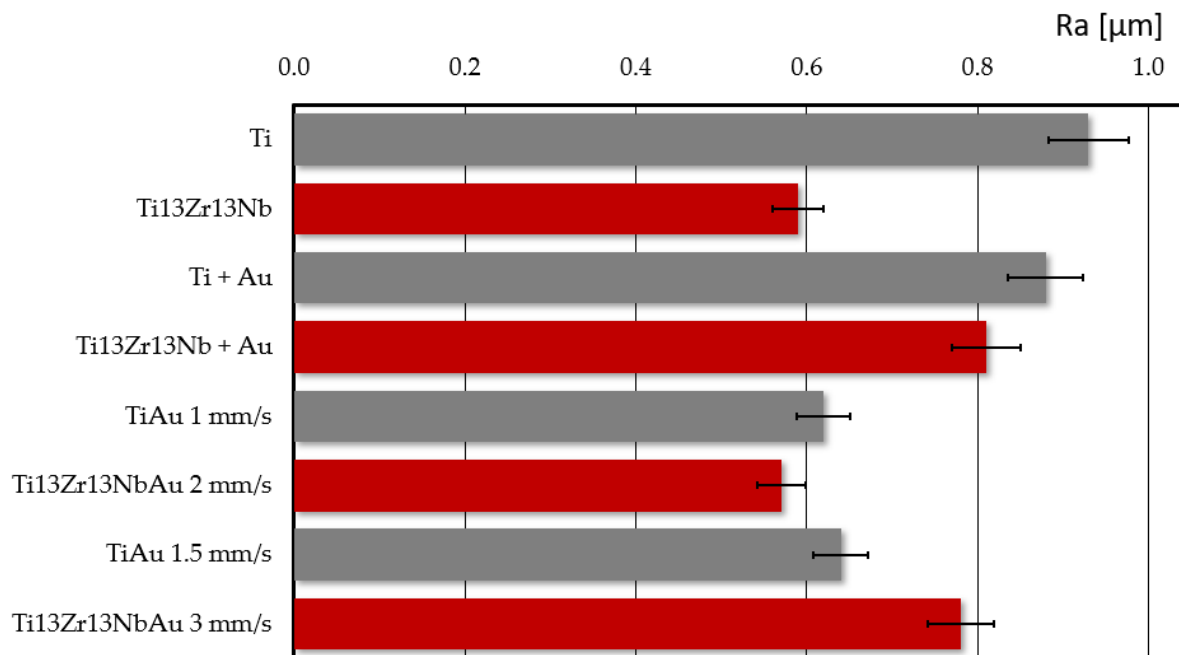


Figure 60. Average roughness test factor Ra for each sample group tested by AFM technique.

5.11 Wetting Angle

The results of the measurements carried out are summarised in Tab. 10 and representative plots of the change in wetting angle and photographs of the droplet shape are summarised in Fig. 61 for Ti-based materials and Fig. 62 for Ti13Zr13Nb - based materials. Each measurement was repeated 5 times to ensure statistical significance of the measurement. The application of gold causes an increase in the wetting angle value and a decrease in the SFE value relative to only etched surfaces for both Ti and Ti13Zr13Nb alloy. The same relationship (increase in angle and decrease in SFE) can be observed after laser treatment of both Ti and Ti13Zr13Nb substrate samples. In the case of gold - coated Ti13Zr13Nb, a laser with a higher velocity causes a decrease in the water wetting angle and an increase in the SFE value. A similar trend for Ti-substrate samples was not apparent. In general, each successive operation (application of gold followed by laser treatment) results in an increase in the wetting angle and a decrease in the SFE, but generally without a change in the nature of the surface to an unambiguously hydrophobic one. The increased wetting angle when gold is applied is due to its hydrophobic nature, as confirmed by the Ricci and Novakovic [89] report. Due to the application of a gold layer of similar thickness, the difference in wetting angle value between Ti + Au and Ti13Zr13Nb + Au is due to the difference in surface roughness [36].

Table 10. Wetting Angle results.

	$\Theta_{\text{water}} [^\circ]$	$\Theta_{\text{dijodometan}} [^\circ]$	$\gamma^d [\text{mN/m}]$	$\gamma^p [\text{mN/m}]$	SFE [mJ/m^2]
Ti	30.17±5.5	77.7±1.2	18.69	43.32	63.01
Ti + Au	53.86±3.4	70.52±4.3	22.55	24.93	47.48
TiAu 1mm	72.25±9.8	60.27±9.1	28.17	9.81	37.98
TiAu 1.5mm	99.01±9.1	69.68±3.3	23.03	1.38	24.42
Ti13Zr13Nb	45.15±4.3	45.15±4.3	29.96	30.95	58.26
Ti13Zr13Nb + Au	69.45±4.7	45.67±5.5	36.55	8.57	45.12
Ti13Zr13NbAu 2mm	80.51±6.6	60.19±2.1	34.46	4.46	38.61
Ti13Zr13NbAu 3mm	71±4.1	39.79±7.2	35.82	7.54	43.36

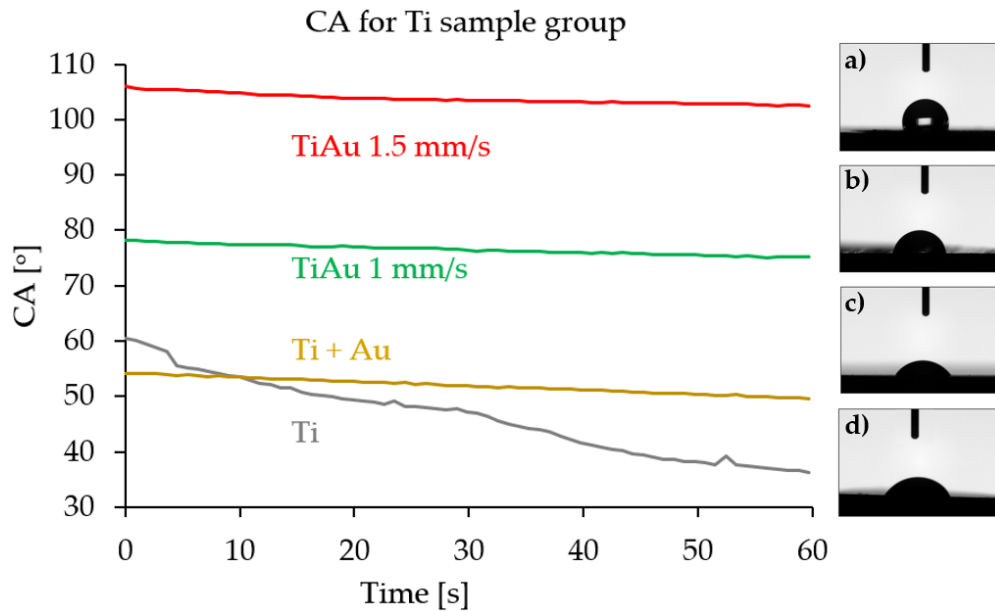


Figure 61. Wetting angle change versus time diagrams and corresponding settle drop images:

a) TiAu 1.5 mm/s, b) TiAu 1 mm/s, c) Ti + Au, - d) Ti, for Ti based sample group.

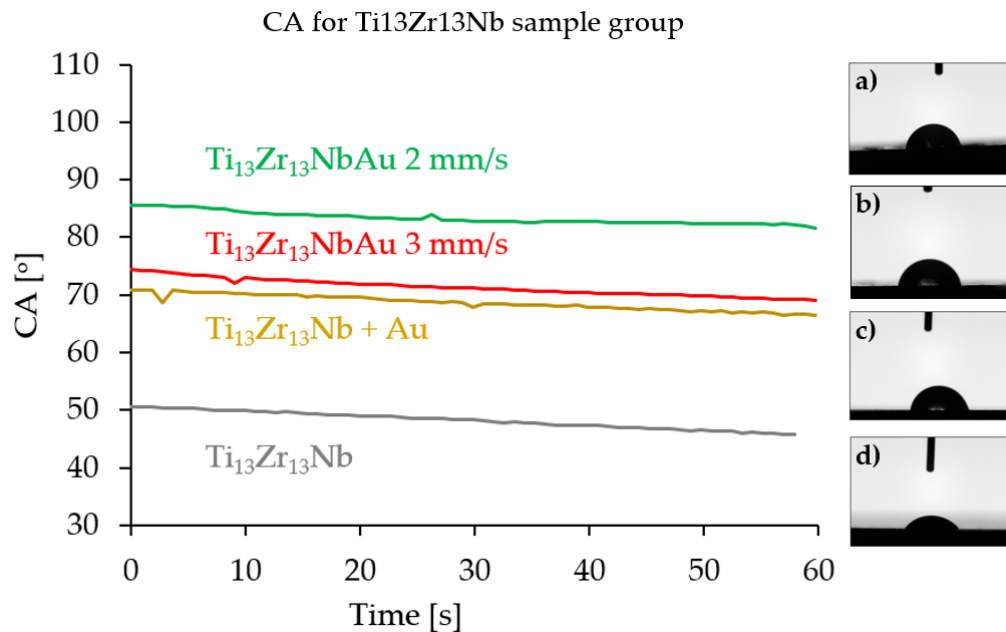


Figure 62. Wetting angle change versus time diagrams and corresponding settle drop images: a) Ti₁₃Zr₁₃NbAu 2 mm/s, b) Ti₁₃Zr₁₃NbAu 3 mm/s, c) Ti₁₃Zr₁₃Nb + Au, - d) Ti₁₃Zr₁₃Nb, for Ti₁₃Zr₁₃Nb based sample group.

5.12 Corrosion

Ti based samples group

Based on tests of the change in open circuit potential as a function of time, positive E_{OCP} values were exhibited by the alloy with the 1.5mm TiAu coating. Slightly lower values were exhibited by the alloy with TiAu 1 mm coating. Au-coated (Tab. 13) titanium was characterised by slightly negative open circuit potential values. As expected, pure titanium showed open circuit potential values most directed towards negative values. In addition, peaks were evident, which are characteristic of the breakthrough of the forming passive layer. The pure gold coating showed the most stable E_{OCP} curve, however, the stability of the open-circuit potential variation as a function of time is closely dependent on the surface quality [108,109]. In the case of the materials tested, polishing could damage the applied coatings.

After an hour-long stabilisation of the E_{OCP} (Fig. 63), polarisation tests were carried out, from which anodic polarization curves were recorded. Based on the Tafel extrapolation of the anodic and cathodic curves (Fig. 64), the corrosion potential and the corrosion current density were determined. Based on the tests, it was found that the TiAu 1.5 mm/s coating had the most

positive E_{corr} potential value (Tab. 11), which is consistent with the obtained open circuit potential value. In addition, TiAu 1.5 mm/s showed the lowest corrosion current density variation. The TiAu 1mm/s coating showed a negative corrosion potential value and a higher corrosion current density value compared to the 1.5 mm/s parameter. Pure titanium was characterised by the most negative E_{corr} and the most positive i_{corr} . On the basis of the electrochemical tests carried out, it can be concluded that the layer with the best corrosion protection is TiAu 1.5 mm/s, while pure titanium proved to be the least resistant of the tested materials.

Table 11. Results of electrochemical test for Ti sample group.

	E_{OCP} [mV]	E_{corr} [mV]	i_{corr} [$\mu\text{A}/\text{cm}^2$]
Ti	-141	$-133,97 \pm 5.03$	$0,64 \pm 0.13$
TiAu 1 mm/s	10	$-12,42 \pm 7.65$	$0,096 \pm 0.04$
TiAu 1.5 mm/s	40	$44,15 \pm 9.39$	$0,046 \pm 0.01$
Ti + Au	-26	$-74,88 \pm 10.45$	$0,440 \pm 0.17$

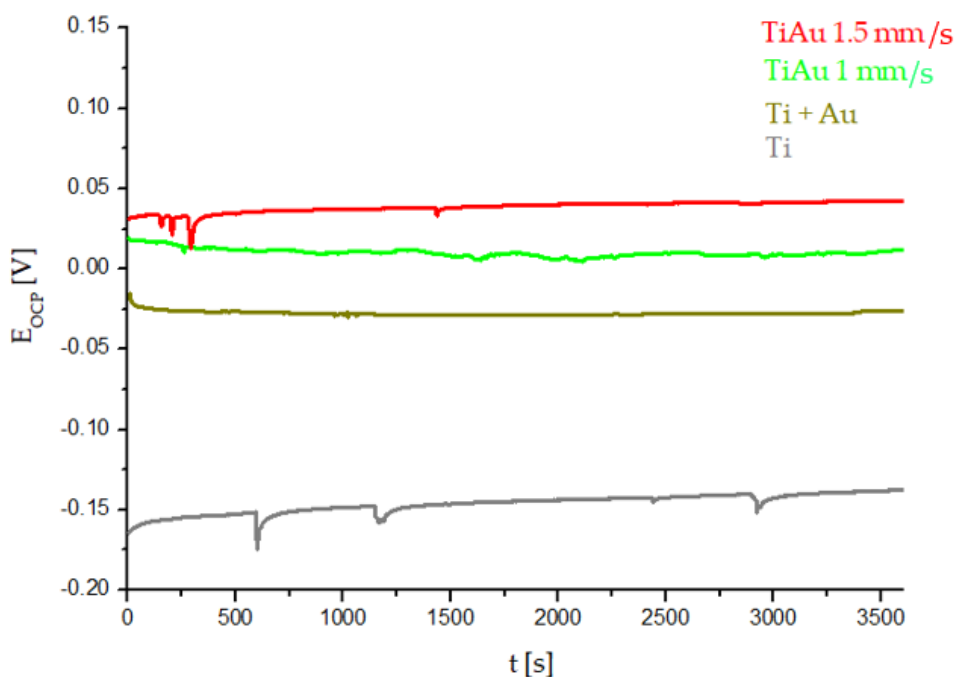


Figure 63. Results of electrochemical test: E_{ocp} , - open circuit potential curves for Ti samples group.

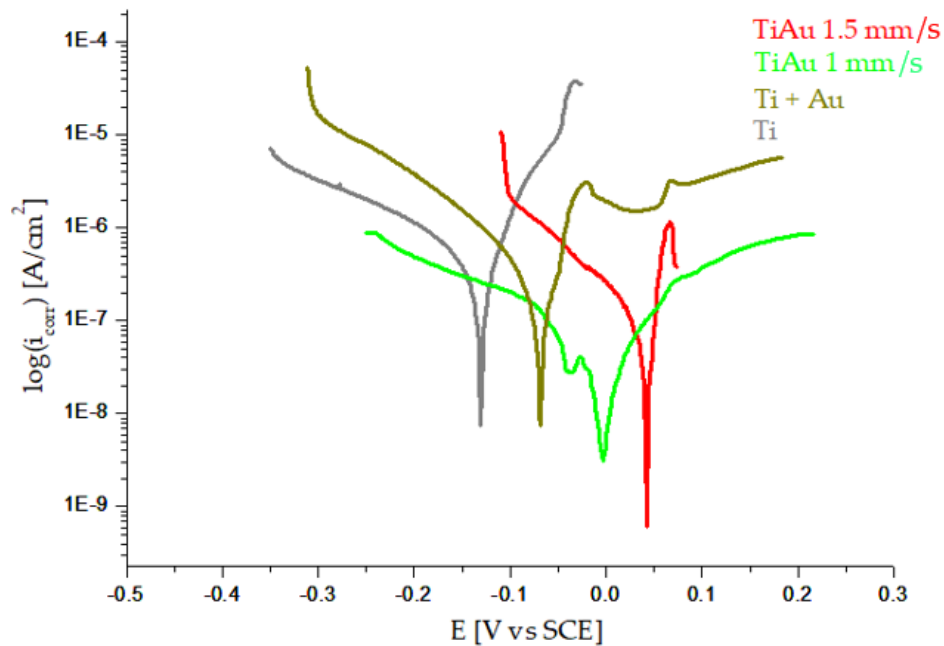


Figure 64. Results of electrochemical test potentiodynamic curves for Ti based samples group.

Ti13Zr13Nb based samples group

Based on the changes in open circuit potential (Fig. 65) as a function of time, the most positive E_{OCP} values were recorded for Ti13Zr13NbAu 3 mm/s, and slightly less for Ti13Zr13NbAu 2 mm/s (Tab. 12). The Au-coated Ti13Zr13Nb alloy initially showed positive potential values, and with increasing time the E_{OCP} values decreased. The characteristics of the gold-coated Ti13Zr13Nb alloy were more positive than those of the uncoated TiZrNb alloy. Based on the polarization curves (Fig. 66), the values of corrosion potential and corrosion current density were determined. According to the measurements, the highest E_{corr} values were characteristic of the Ti13Zr13NbAu 2mm/s coating. The average values of the corrosion potential were similar for TiZrNb and Ti13Zr13Nb + Au, however, the corrosion current density was higher for the gold coating. Ti13Zr13NbAu 3 mm/s was characterized by the most negative E_{corr} values as showed Tab. 12. The discrepancy in the results indicates a difference in the mechanisms of corrosion processes, so it is important to analyze the corrosion products. Based on observations using scanning electron microscopy, it was observed that in the case of

Ti13Zr13NbAu 3 mm/s there are local galvanic micro-cells, which accelerate the corrosion destruction process (Fig. 74).

Table 12. Results of electrochemical test for Ti13Zr13Nb sample group.

	E_{OCP} [mV]	E_{corr} [mV]	i_{corr} [$\mu\text{A}/\text{cm}^2$]
Ti13Zr13Nb	22	-79.84 ± 5.38	0.21 ± 0.004
Ti13Zr13NbAu 2 mm/s	101	-30.99 ± 60	0.02 ± 0.008
Ti13Zr13NbAu 3 mm/s	114	-198 ± 34	0.44 ± 0.3
Ti13Zr13Nb + Au	36	-65.64 ± 1.25	19.24 ± 6.8

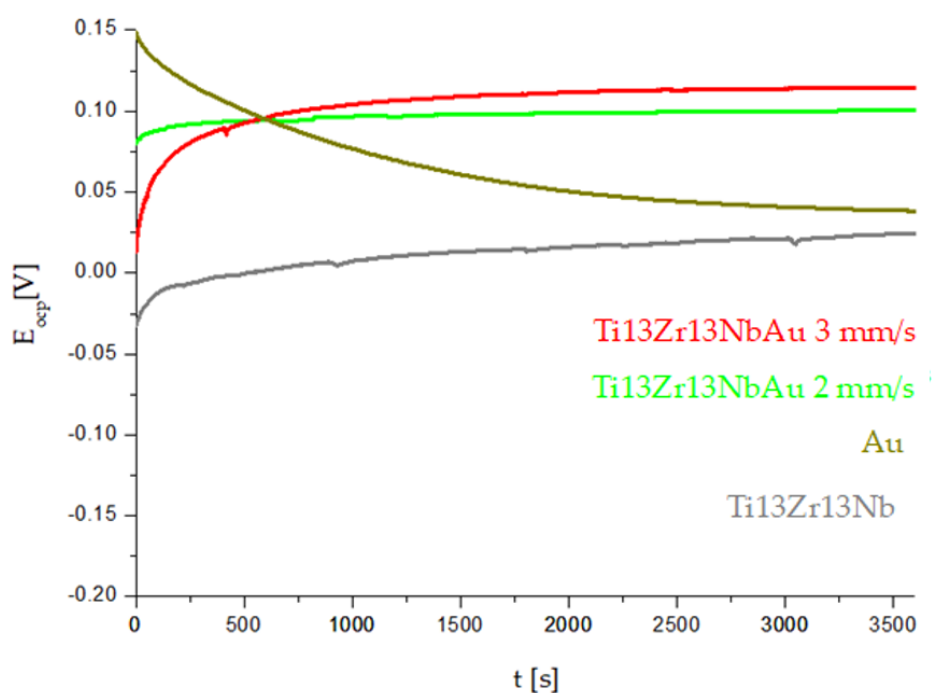


Figure 65. Results of electrochemical test: E_{otp} , - open circuit potential curves for Ti13Zr13Nb samples group.

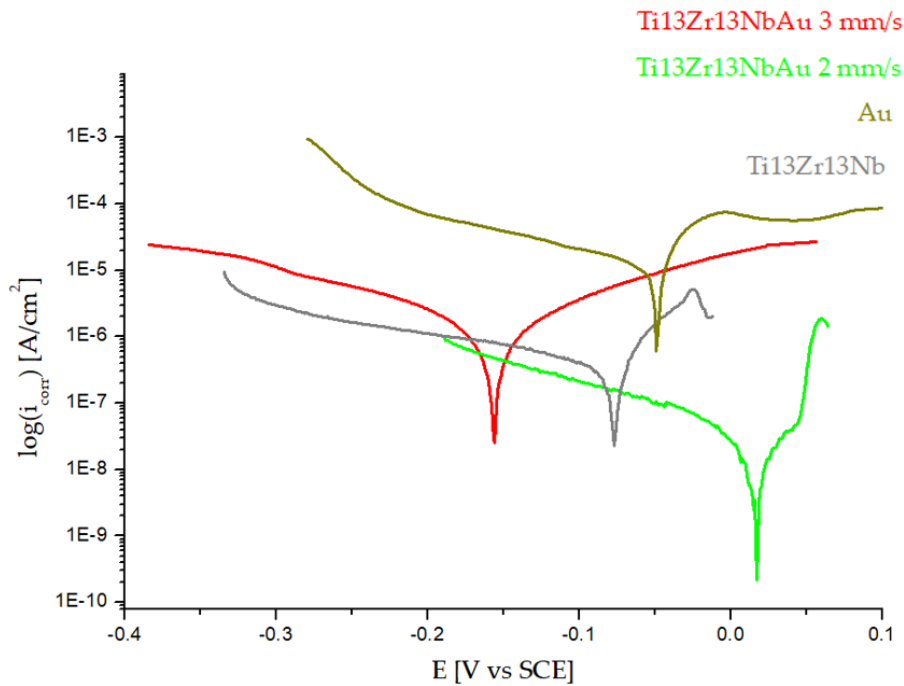


Figure 66. Results of electrochemical test potentiodynamic curves for Ti13Zr13Nb based samples group.

The open circuit potential values for the Ti samples tend to shift towards more electropositive values without stabilizing over the test time. A similar trend was observed for the TiAu 1.5mm/s samples. However, for the Au and TiAu 1 mm/s samples, the open circuit potential values begin to decrease and then gradually stabilize (as shown in Figure 64). The most positive open circuit potential values were obtained for the Au enriched samples - recorded values were more than 7 times higher than those obtained for Ti samples, indicating better corrosion resistance for samples with Au due to the noble nature of Au. The highest values of the open circuit potential in comparison to Titanium were obtained for both groups of TiAu samples (1 mm/s and 1.5 mm/s). In the case of Ti13Zr13Nb based samples the similar tendency has been revealed (Fig. 66). To investigate the effect of Au content on corrosion resistance, a Tafel method was performed. The obtained values of corrosion potential (E_{corr}) confirm the behavior of the open circuit potential (Fig. 67 and Table 12). The recorded values of the current density for Au samples were lower than those recorded for uncoated titanium samples, indicating that the corrosion resistance of the Au enriched samples was better. The lowest values of i_{corr} were observed for the TiAu 1 mm/s and TiAu 1.5 mm/s sample groups, indicating the best corrosion resistance in the tested group. For the TiAu 1mm/s and TiAu 1.5 mm/s samples, i_{corr} decreased from 0.639 (Ti) to 0.096 and 0.046 $\mu\text{A}/\text{cm}^2$, respectively (Fig. 65). In the case of Ti13Zr13Nb

samples group the icorr increased from 0.21 (Ti₁₃Zr₁₃Nb) up to 0.44 and 19.24 $\mu\text{A}/\text{cm}^2$ in Ti₁₃Zr₁₃NbAu 3 mm/s and Ti₁₃Zr₁₃Nb + Au respectively. However, The Ti₁₃Zr₁₃NbAu 2 mm/s icorr value was 0.02 $\mu\text{A}/\text{cm}^2$ as presented in Fig. 67. (It should be noted that the TiAu samples exhibit the Ti₃Au phase, which is prone to preferential dissolution in corrosion environments [110] [111]. Gold is known for its low reactivity and resistance to corrosion. However, when it is deposited on titanium as a thin layer (around 2 μm), it may not be thick enough to protect the base material from corrosion. The solution may be able to penetrate any defects in the gold layer, allowing the titanium to corrode.

Electrochemical Impedance Spectroscopy results

Ti based sample group

The impedance spectra of Ti and Ti-based coatings were presented in figures 67, 68, and 69 in the form of Nyquist plots and Bode diagrams. The Nyquist diagrams showed semi-circles located at the origin of the coordinate system, which were deformed to different degrees for the different samples. It was found that increasing the angle of inclination of the curves for the Au coated material and laser-treated samples indicated increased impedance values and corrosion resistance compared to the Ti samples. The impedance modulus for all samples decreased with increasing frequency of the voltage excitation signal. For low frequencies, the impedance modulus was higher for the modified samples, but at higher frequencies, the situation was reversed. Additionally, the highest values of the phase shift angle, around 80 degrees, in the Bode phase diagram were observed in the laser-treated samples, compared to the non-stable values of 60 degrees at the peak in low frequencies and 40 degrees and high frequencies for the Ti. Large values of the phase shift angle in the high and mid-frequency region indicate the presence of a capacitive double layer between the solution and the substrate material. The impedance spectra of the analyzed corrosion systems were also studied using electrical equivalent circuit, as shown in Fig. 70. It was found that for both groups of samples, an equivalent circuit with two-time constants was used to analyze the EIS data, indicating the presence of two sublayers: a cohesive inner one and a porous outer one, as evidenced by the two-time constants on the plot. The equivalent circuit consists of R_s — electrolyte resistance, R_{pore} — electrical resistance of the electrolyte in the pores, CPE_{pore} — capacity of the double

layer-porous surface, and R_{ct} and CPE_{dl} — resistance and capacity of the twin substratum, respectively (Table 13)[112,113].

Table 13. Results of EIS test for Ti based sample group.

Parameters	Samples				
	Ti	Ti+Au	TiAu 1 mm/s	TiAu 1.5 mm/s	
R_s [$\Omega \times \text{cm}^2$]	6.8	1.394	2	2	
R_{pore} [$\Omega \times \text{cm}^2$]	2 000	5 400	6 500	5 800	
R_{ct} [$\Omega \times \text{cm}^2$]	21 900	21 800	42 000	25 000	
CPE_{pore}	Y_p [$\mu\text{F} \times \text{s}^{n-1}/\text{cm}^2$]	0.80×10^{-3}	100.85×10^{-6}	20.24×10^{-6}	105.2×10^{-6}
	n_p	0.55	0.85	0.82	0.66
CPE_{dl}	Y_{dl} [$\mu\text{F} \times \text{s}^{n-1}/\text{cm}^2$]	0.585×10^{-3}	0.308×10^{-3}	0.135×10^{-3}	0.51×10^{-3}
	n_{dl}	0.83	0.7	0.6	0.65

For all sample variants, the R_{ct} value was greater than the R_{pore} value, indicating that the inner compact layer plays a more significant role in corrosion protection. The best resistance is seen in the TiAu 1 mm/s variant, with an R_{ct} value almost two times higher than that of pure titanium and Ti + Au without laser treatment. The TiAu 1.5 mm/s variant also showed better corrosion resistance of the compact layer than the non-laser-treated samples. In general, the higher the R_{ct} value, the more compact and protective the layer of the sample is [113].

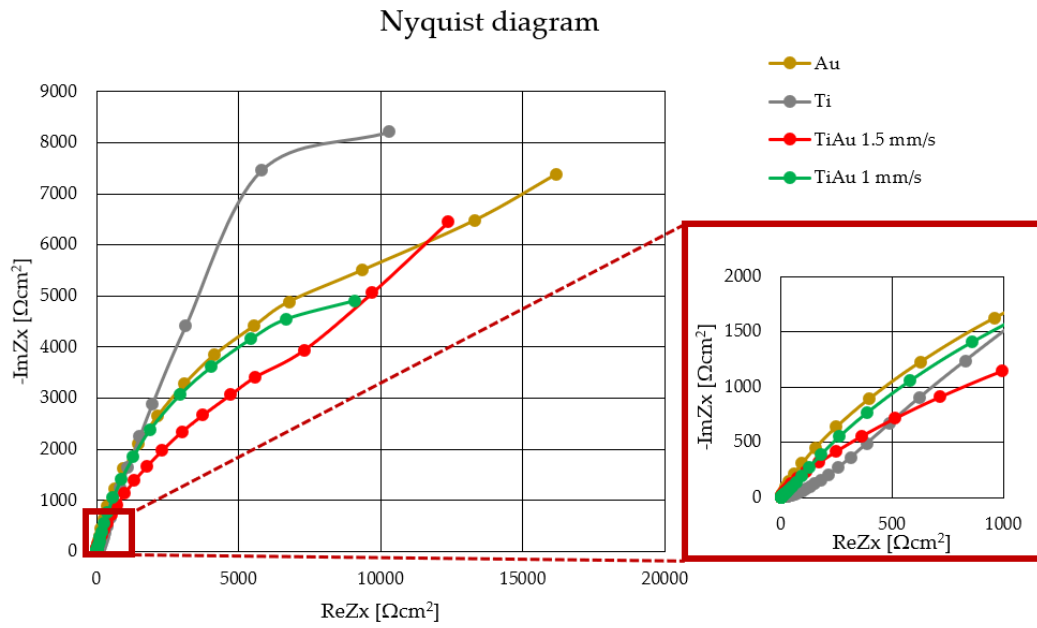


Figure 67. Nyquist diagram for Ti based sample group.

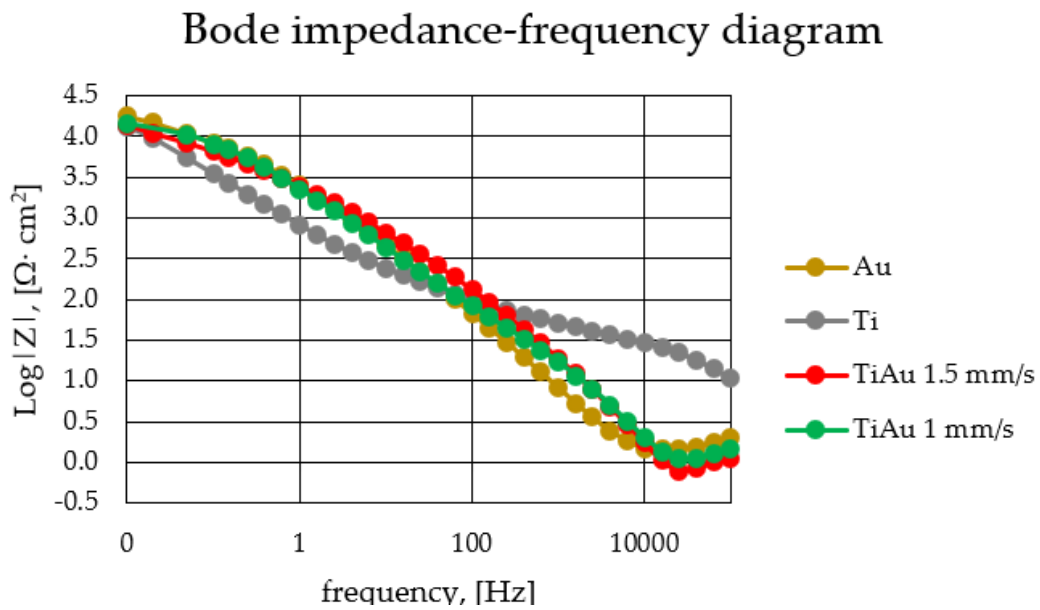


Figure 68. Bode impedance - frequency diagram for Ti based sample group.

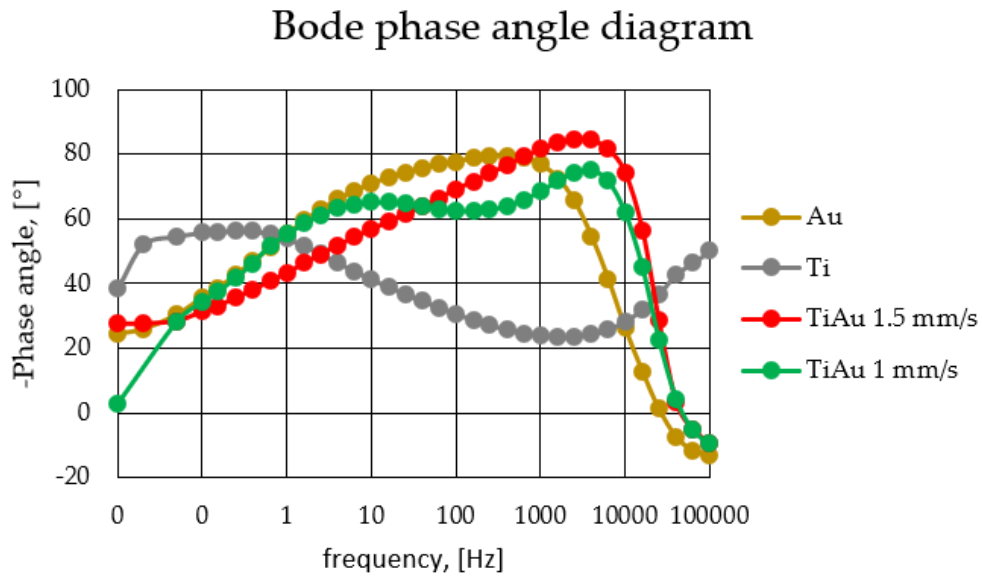


Figure 69. Bode phase angle diagram for Ti based sample group.

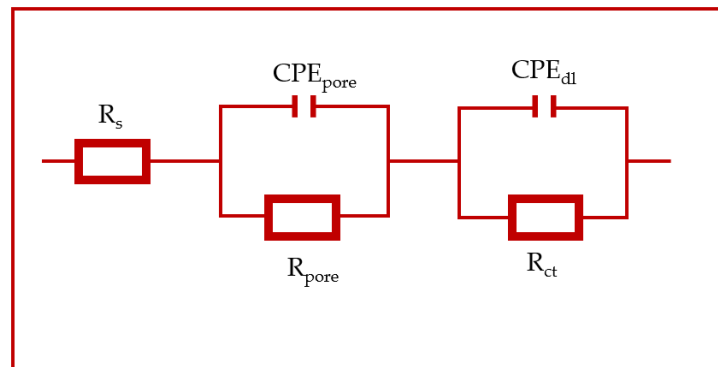


Figure 70. The Electrical Equivalent Circuit (EEC) for the EIS tests.

Ti13Zr13Nb based samples group

The impedance spectra of Ti13Zr13Nb and Ti13Zr13Nb-based coatings are presented in Fig. 71, 72, 73 in the form of Nyquist plots and Bode diagrams. The Nyquist diagrams showed semi-circles located at the origin of the coordinate system, which were deformed to different degrees for the different samples. It was found that increasing the angle of inclination of the curves for the Ti13Zr13NbAu 2mm/s coated material indicated increased impedance values and corrosion resistance compared to Ti13Zr13Nb + Au, Ti13Zr13NbAu 3 mm/s, and Ti13Zr13Nb. The Bode modulus plot showed similar impedance modulus values for all variants over the full range of frequencies. The impedance modulus for all samples decreased with increasing frequency of the voltage excitation signal. For low frequencies, the impedance modulus was higher for the

modified samples, but at higher frequencies, the situation was reversed. Additionally, the highest values of the phase angle displacement in the Bode phase diagram were observed in all tested samples, around 80 degrees. Large values of the phase shift angle in the high and mid-frequency region indicate the presence of a capacitive double layer between the solution and the substrate material. The impedance spectra of the analysed corrosion systems were also studied using alternative electrical circuits, as shown in Fig. 70. Again, for both groups of samples, an electrical equivalent circuit (Fig. 67) with two-time constants was used to analyse the EIS data, indicating the presence of two sublayers: a cohesive inner one and a porous outer one, as evidenced by the two-time constants on the plot. The equivalent circuit consists of R_s — electrolyte resistance, R_{pore} — electrical resistance of the electrolyte in the pores, CPE_{pore} — capacity of the double layer-porous surface, and R_{ct} and CPE_{dl} — resistance and capacity of the twin substratum, respectively (Table 14).

Table 14. Results of EIS test for Ti13Zr13Nb based sample group.

Parameters	Samples				
	Ti13Zr13Nb	Ti13Zr13Nb + Au	Ti13Zr13NbAu 2 mm/s	Ti13Zr13NbAu 3 mm/s	
R_s [$\Omega \times \text{cm}^2$]	1	1	2	2	
R_{pore} [$\Omega \times \text{cm}^2$]	13 400	12 000	39 200	41 500	
R_{ct} [$\Omega \times \text{cm}^2$]	708 800	150 000	14 000	110 000	
CPE_{pore}	Y_p [$\mu\text{F} \times \text{s}^{-n-1}/\text{cm}^2$]	0.123×10^{-3}	90.65×10^{-6}	0.3253×10^{-3}	54.48×10^{-6}
	n_p (a2)	0.677	0.62	0.7619	0.828
CPE_{dl}	Y_{dl} [$\mu\text{F} \times \text{s}^{-n-1}/\text{cm}^2$]	0.5×10^{-3}	0.121×10^{-3}	53.5×10^{-6}	0.1425×10^{-3}
	n_{dl}	0.762	0.75	0.6893	0.809

For specimens with Ti13Zr13Nb based material, the R_{ct} coefficient suggesting the contribution of the inner compact layer to corrosion protection is higher for the non-laser-treated variants (Ti13Zr13Nb, and Ti13Zr13Nb + Au) and for the Ti13Zr13Nb Au 3 mm/s parameter. For the Ti13Zr13NbAu 2 mm/s variant, the porous layer takes a decisive part in the corrosion protection. The highest R-value is characterised by Ti13Zr13Nb + Au, which is indicative of a good tight gold coating of the samples (anodic protection). However, the laser-treated variants relative to the native material Ti13Zr13Nb are characterised by an R_{pore} value 3 times higher for Ti13Zr13NbAu 3 mm/s, and 2.9 times higher for Ti13Zr13NbAu 2 mm/s.

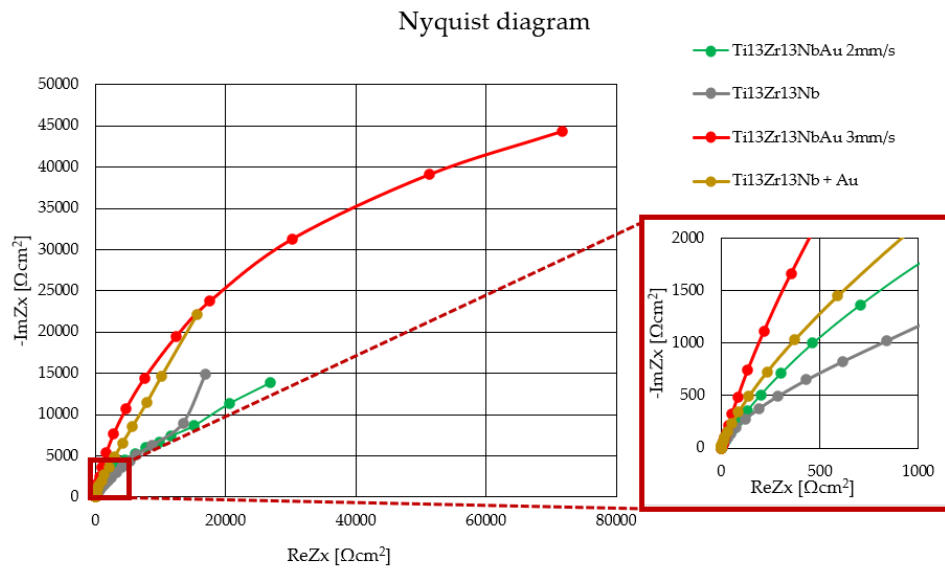


Figure 71. Nyquist diagram for Ti13Zr13Nb sample group.

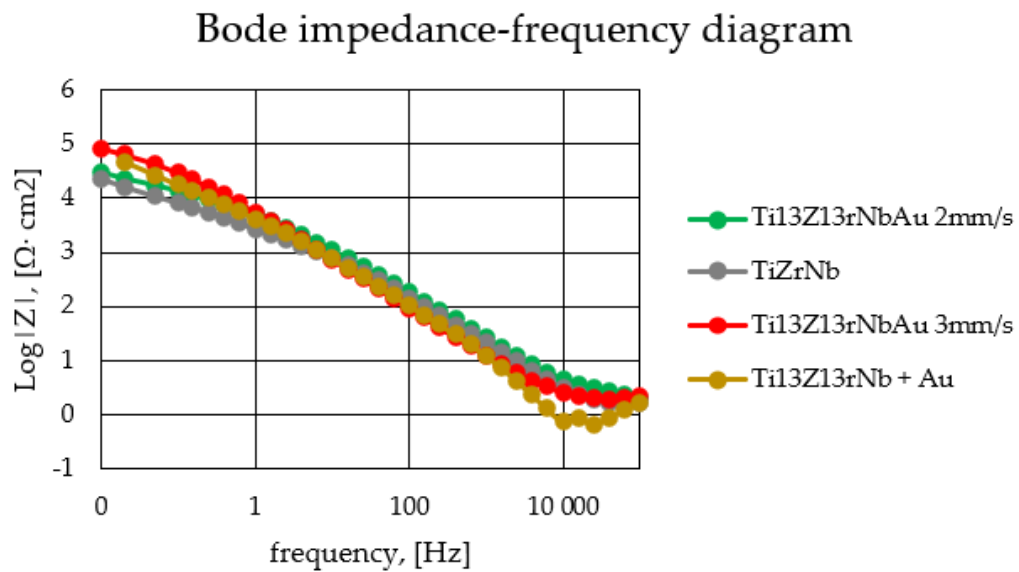


Figure 72. Bode impedance-frequency diagram Ti13Zr13Nb sample group.

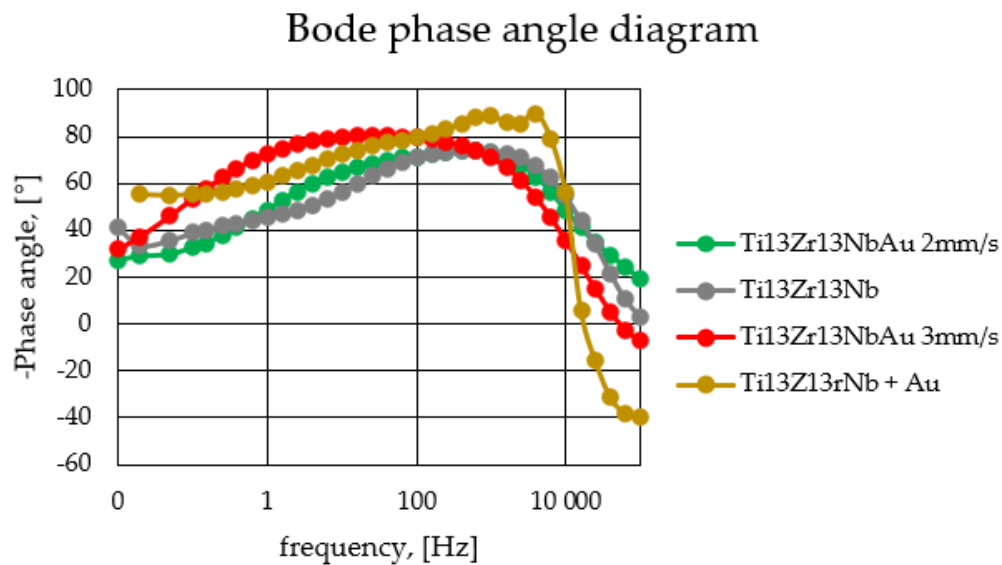


Figure 73. Bode phase angle diagram Ti13Zr13Nb sample group.

After the corrosion test, it is possible to observe the changes that occurred in the sample's microstructure using a high-resolution imaging technique SEM. In the case of Ti and Ti13Zr13Nb, the sample's surface may show the presence of pits and dissolutions, which are indicative of corrosion damage. Pits are small cavities or holes in the surface of the material, while dissolutions are the loss of material from the surface due to chemical reactions with the environment. The formation of pits and dissolutions can weaken the material and reduce its lifespan. In the case of Ti13Zr13NbAu 3mm/s, the sample's surface may also exhibit microgalvanic cells, which are small regions where corrosion is more severe due to the combined effects of chemical and electrochemical reactions. These cells can occur when different materials in the sample interact with each other and the environment during corrosion. The images are presented in the Fig. 74.

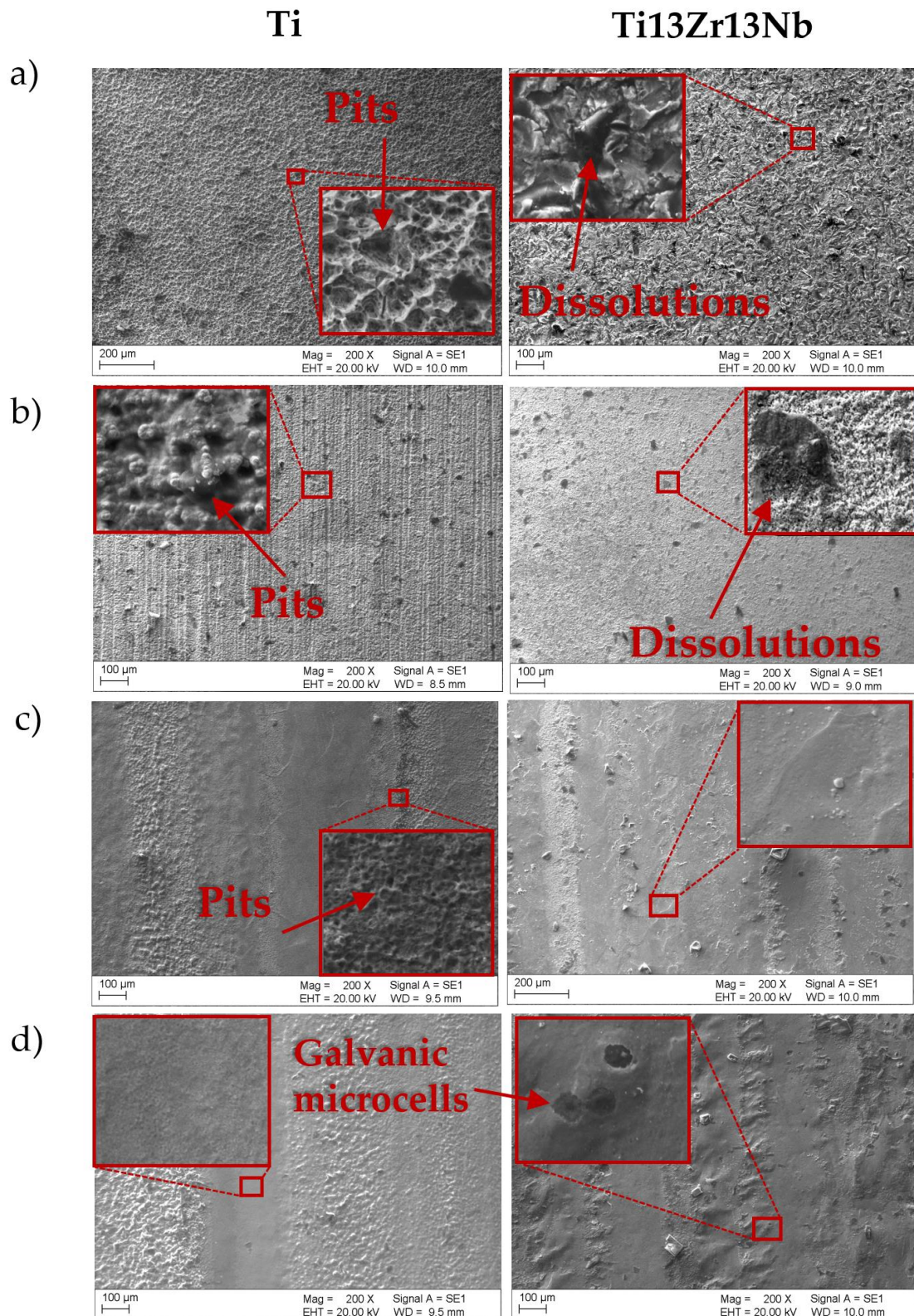


Figure 74. SEM images of samples after corrosion testing a) pure Ti and Ti13Zr13Nb, b) samples after Au coating, c) Ti variant 1 mm/s, Ti13Zr13NbAu 2 mm/s, d) Ti 1.5 mm/s, Ti13Zr13NbAu 3 mm/s.

Corrosion resistance studies have shown that adding Au and laser treating the surface layer can increase corrosion resistance. However, in some cases, due to local chemical changes in the Au content caused by insufficient control of the process, the corrosion resistance may be slightly decreased. Despite this, the overall corrosion resistance of samples with added Au and laser treatment is better than that of the base materials (Ti and Ti13Zr13Nb) without these modifications or only coated with gold through Electrochemical process. This increased corrosion resistance is crucial for biomedical applications, where the material must be able to withstand the harsh conditions of the human body without corroding or degrading. By improving the corrosion resistance of these materials, it is possible to ensure their safe and effective use in medical devices and implants.

5.13 Tribological tests

For titanium alloys used in biomedical implants, poor tribological performance and low surface hardness have typically been documented [114,115]. Their tribological behaviour is thought to have negative impacts such as high coefficients of friction (COF), severe adhesive wear, and low abrasion resistance. By disturbing the protective oxide layer, mechanical sliding between titanium alloys (or a titanium alloy and another material) can cause wear damage to the surface, especially when a third body is present at the interface. Due to the high reactivity of titanium alloys, the oxide surface layer quickly changes to an oxidative environment, which may result in removal during the sliding of the two contacting surfaces. The results of a study performed by De Viteri and Fuentes [116] showed that the protective oxide layer can be removed from the surface of metals. This phenomenon occurs by applying contact loads which allows metals to have interaction with the surrounding environment (or the adjacent material). It can cause adverse effects including high friction and corrosion, and also premature failure of implants [116,117]. The wear resistance of Ti-6Al-4V is poorer than that of 316L stainless steel and Co-Cr-Mo alloy, according to Geetha et al. [118] Additionally, when compared to the Co-Cr alloy and stainless-steel prostheses, larger metal concentrations were found in the tissue that was taken from the area around the Ti-alloy prosthesis. In view of the above, the need to improve the tribological properties of titanium-based biomaterials is eminent. Tests carried out under physiological walk conditions and in the environment of ringer solution similarly to the work of the Svanidze et al. [31]. The tribological test results for Ti-based materials are shown

in Fig. 75. The quantitative values of the results are shown in Tab. 15. Similarly, the results for Ti13Zr13Nb-based materials are shown in Figure 76.

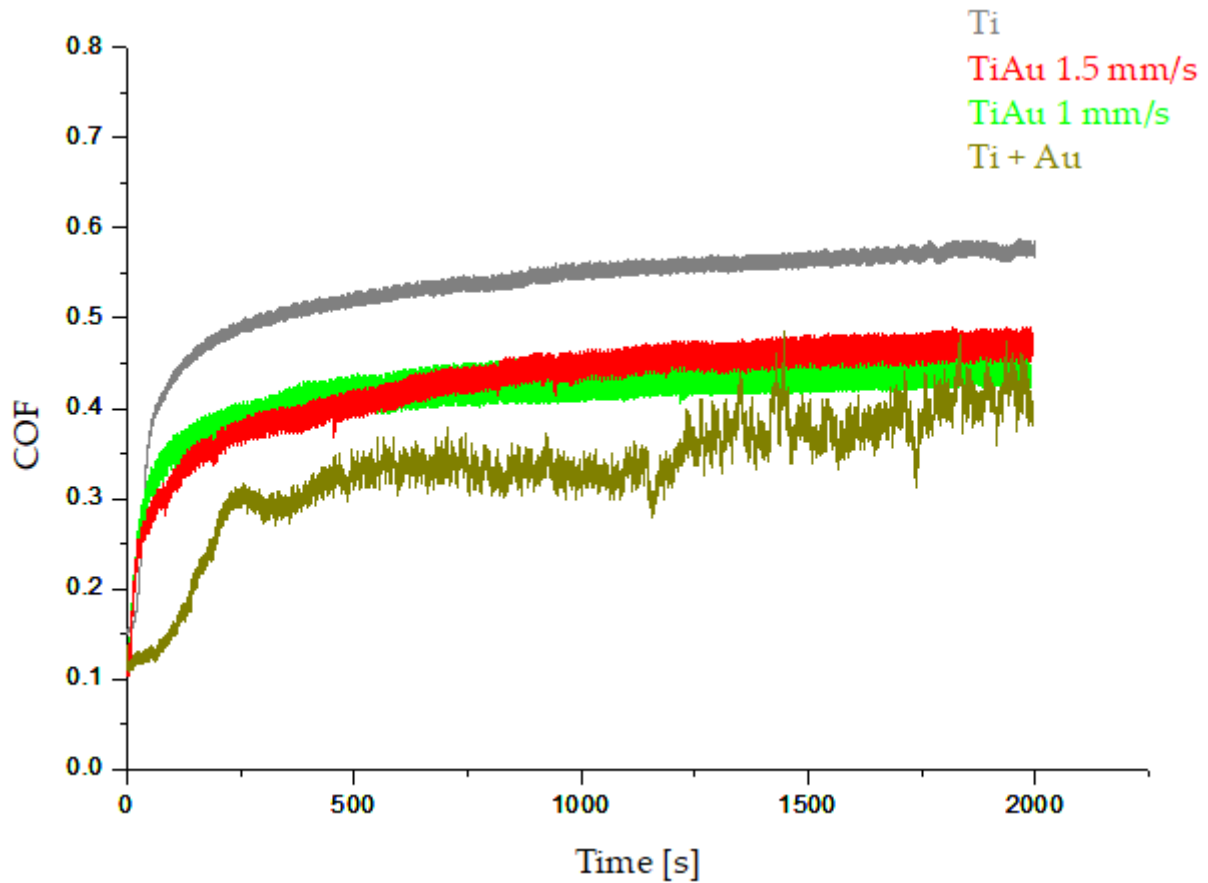


Figure 75. Coefficient of Friction vs Time dependence diagram for the Ti based sample group.

Table 15. Average and standard deviation values of the wear test for Ti based sample group.

	Ti	Au	TiAu 1.5mm/s	TiAu 1mm/s
Average	0.48	0.35	0.40	0.40
Standard deviation	0.24	0.09	0.11	0.10

In Fig. 69 relating to Ti-based sample group under the assumed test parameters, it can be seen from the COF vs time dependence plots that for electrochemically deposited and non-laser-treated gold, the gold layer abrades after approximately 250s, after which it increases steadily until a COF of 0.35 is reached, close to the TiAu parameters of 1.0mm/s and 1.5mm/s. In addition, the COF achieved by pure Ti is the highest (0.48) which prospects faster material wear. The laser-treated samples stabilised at a similar level to each other (average 0.40),

resulting in lower wear under test conditions and a longer product life cycle. The quantitative values of the results are shown in Tab. 16.

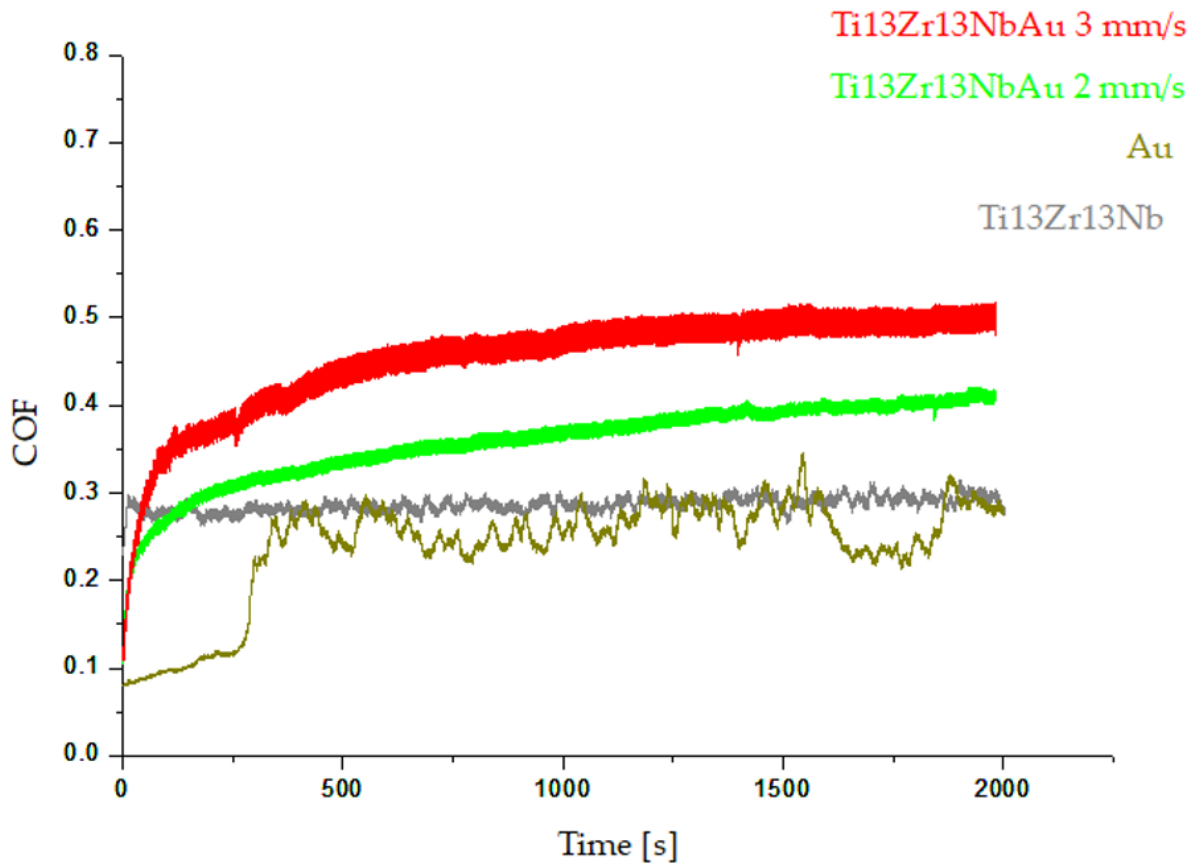


Figure 76. Coefficient of Friction vs Time dependence diagram for the Ti13Zr13Nb based sample group.

Table 16. Average and standard deviation values of the wear test for Ti13Zr13Nb based sample group.

	Ti	Au	Ti13Zr13NbAu 2 mm/s	Ti13Zr13NbAu 3 mm/s
Average	0.28	0.25	0.44	0.43
Standard deviation	0.12	0.12	0.11	0.11

Figure 76. showing Ti13Zr13Nb-based sample group dependencies under the same test parameters as in Fig. 75. It can be seen from the COF vs time dependency plots that for electrochemically deposited and laser untreated gold, the gold layer abrades after exactly the same time of approximately 250s (this indicates a similar thickness and type of coating), after

which the COF increases and stabilises at 0.25 similar to the parameters of the base material (Ti13Zr13Nb). This is due to the lower roughness, which allows Au particles to be completely eliminated from the wear groove area. In the case of Ti- based samples, due to the twice higher roughness, complete removal of gold from the abrasion lodge under the assumed test conditions is impossible, resulting in the penetrator sliding over the softer gold particles, which results in a lower coefficient of friction (COF). An increase in the coefficient of friction with comparison to the native material (Ti13Zr13Nb) is observed for the laser-treated samples, to an average value of 0.44 for both parameters, which is slightly higher than the laser-treated Ti samples. This is not a good predictor of tribological wear in this case. SEM images of samples after tribology tests are presented in Fig. 77.

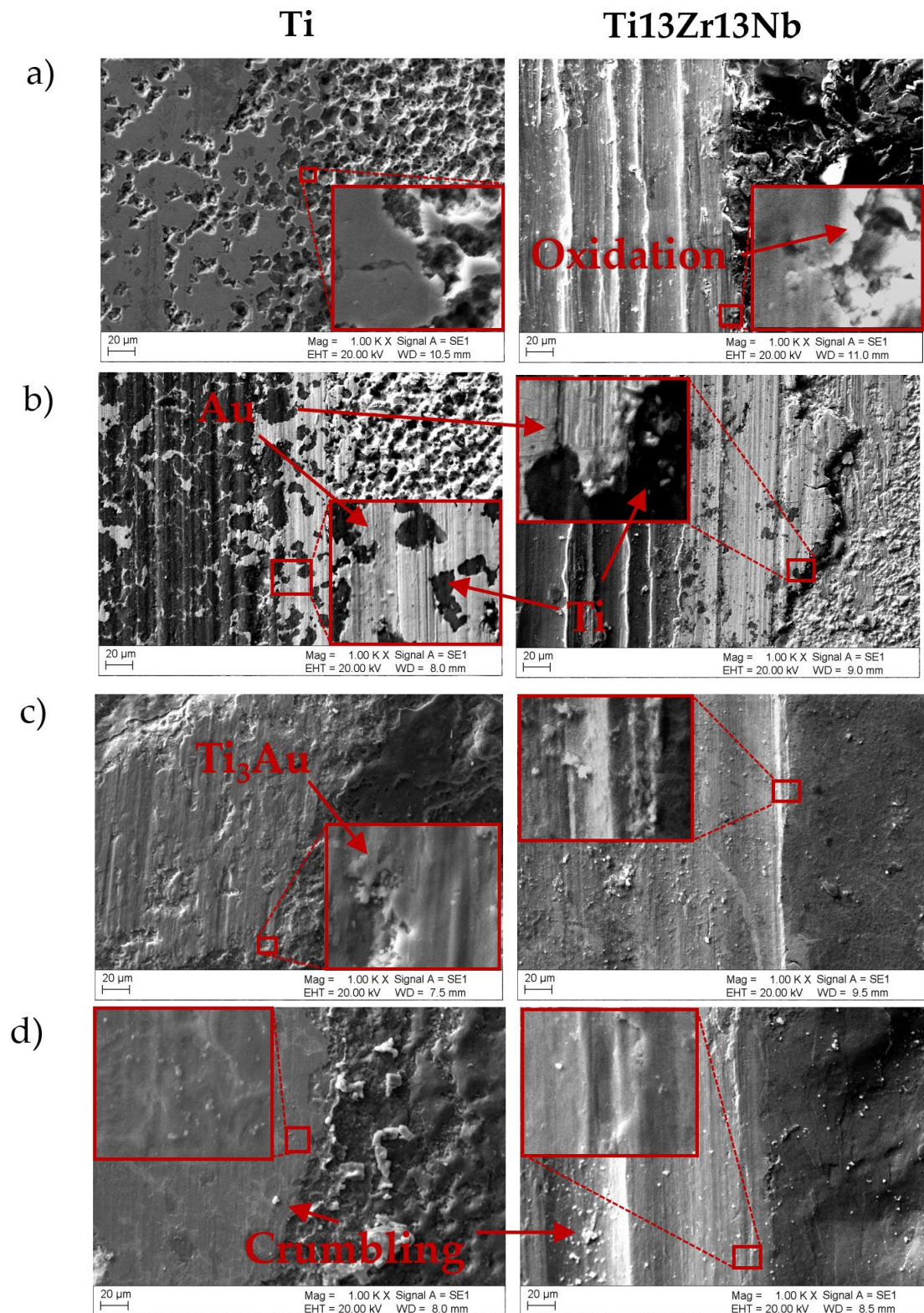


Figure 77. SEM images of samples after tribology testing a) pure Ti and Ti13Zr13Nb, b) samples after Au coating, c) Ti variant 1 mm/s, Ti13Zr13NbAu 2 mm/s, d) Ti 1.5 mm/s, Ti13Zr13NbAu 3 mm/s.

Fig. 77 shows SEM image documentation of the test samples taken after tribological wear tests. The images show a) pure Ti and Ti₁₃Zr₁₃Nb, b) samples after Au coating, c) Ti variant 1 mm/s, Ti₁₃Zr₁₃NbAu 2 mm/s, d) Ti 1.5 mm/s, Ti₁₃Zr₁₃NbAu 3 mm/s. The images indicate the individual dominant chemical compositions in a specific area. The Images highlight the predominance of abrasive wear. The specimens showing the laser-treated variants (image c and d)) have noticeably the smallest wear marks compared to non-laser processed samples, which is confirmed by the hardness results obtained. In the case of samples with an applied layer of gold untreated by laser b), the difference in the abrasive behaviour of titanium and gold can be seen most clearly, loss of adhesion of the layer to the substrate is visible. The surviving coating remnants in the wear groove are also visible, reflecting the COF undershoot obtained in diagram presented in Fig. 69.

5.14 Nanoindentation test

Figures 78 and 79 show load diagrams as a function of vertical indenter displacement for nanoindentation testing for Ti based specimens (Fig. 78) and Ti₁₃Zr₁₃Nb based specimens (Fig. 79). The recorded measurement curves allow the hardness Vickers indentation test (HV_{IT}) and Young's modulus indentation test (E_{IT}) to be read. These values are shown in Table 17 and 18.

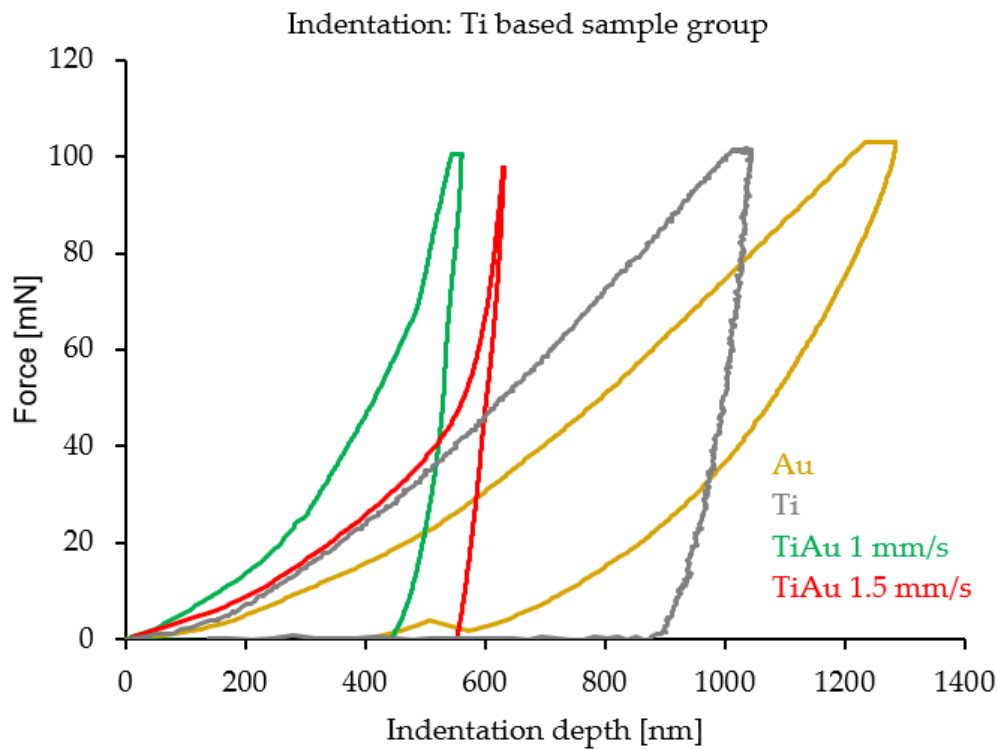


Figure 78. Nanoindentation test results for Ti based sample group.

Table 17. Nanoindentation test results for Ti based sample group.

	HV _{IT}	E _{IT} [GPa]
Au	68.23 ± 21.0	56.7 ± 5.0
Ti	189.0 ± 2.16	71.33 ± 11.2
TiAu 1 mm/s	226.0 ± 27.0	151.3 ± 4.2
TiAu 1.5 mm/s	215.7 ± 20.0	114.3 ± 20.0

During the nanohardness tests, average vickers hardness results of 68 HV for gold were obtained for Ti substrate samples and 64 HV for TiZrNb substrate. Considering tabulated data from chemical element databases (AZOM materials) [119], these values are within the average accepted value for chemically pure gold according to mentioned base approximately 60 HV. A significant increase in hardness was recorded for the TiAu samples after laser treatment in both treatment variants, for TiAu 1 mm/s approximately 226 HV, and for TiAu 1.5 mm/s - 215.7 HV, according to the research reported by Svanidze et. al. [31].

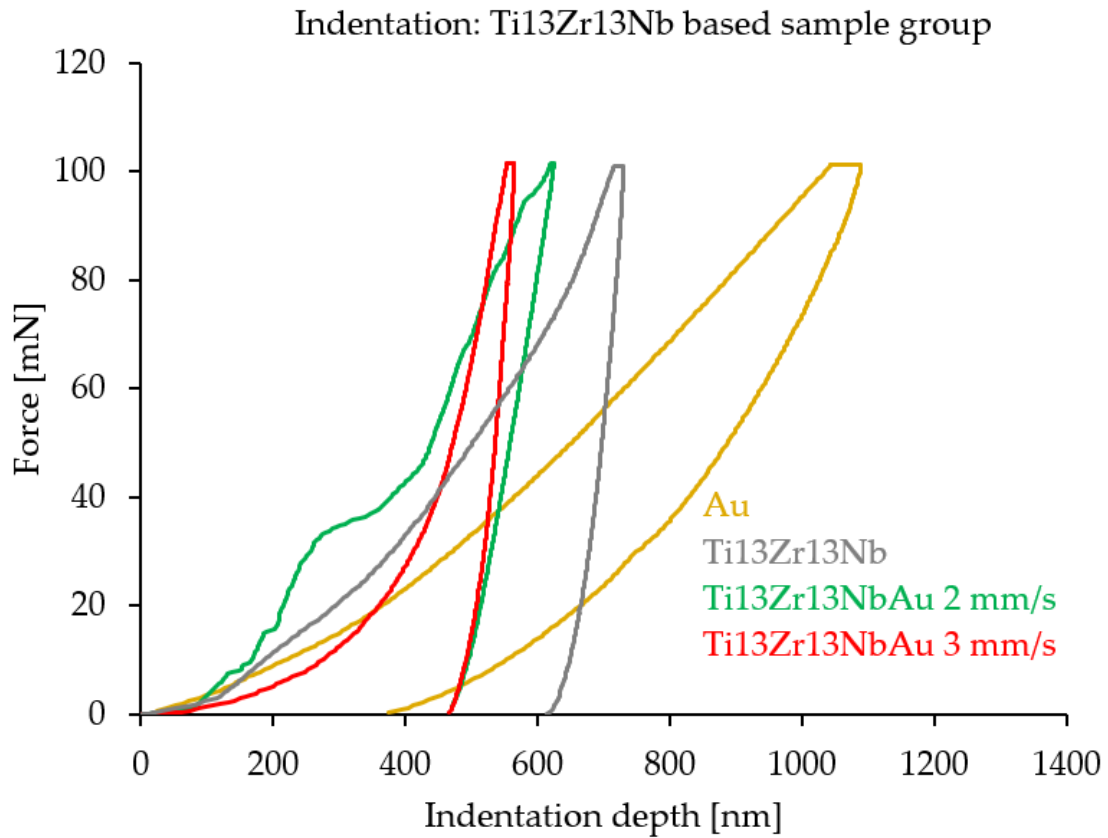


Figure 79. Nanoindentation tests results for TiZrNb based sample group.

Table 18. Nanoindentation test results for Ti13Zr13Nb based sample group.

	HV _{IT}	E _{IT} [GPa]
Au	64.7±4.6	57.7 ± 8.6
Ti13Zr13Nb	113±3.6	158.3±3.4
Ti13Zr13NbAu 2 mm/s	117.7 ± 26.8	125.7 ± 10.3
Ti13Zr13NbAu 3 mm/s	145.3±30.35	109.0 ± 14.7

5.15 Cytotoxicity

In order to simplify the determination of samples for cytotoxicity analysis, samples were labelled as shown in Tab 19 below:

Table 19. Determination of samples for testing.

label	1	2	3	4	5	6	7	8
sample	Ti	Ti + Au	TiAu 1 mm/s	TiAu 1.5 mm/s	Ti13Zr13Nb + Au	Ti13Zr13NbAu 2 mm/s	Ti13Zr13NbAu 3 mm/s	Ti13Zr13Nb

Most of the materials evaluated did not show inferior biocompatibility to the control culture plastic surface (polystyrene plate well, 6-well format, Sarstedt). The exception may be the samples identified with numbers 1 and 5, where the number of counted cells per scanned surface was lower than the untreated control (C). The remaining materials show concordance in the absence of toxicity to the normal human fibroblast lineage (Figure 80).

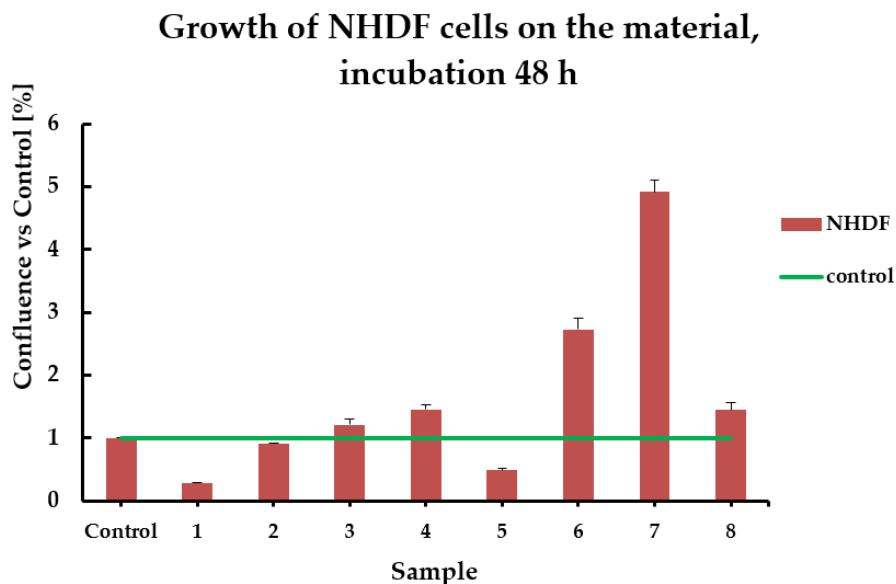


Figure 80. NHDF cell density on materials, 48 h incubation. Results from counts of cell nuclei from the scanned surface. Results are presented as percentage change from control population; mean of 3 experiments +/- SD.

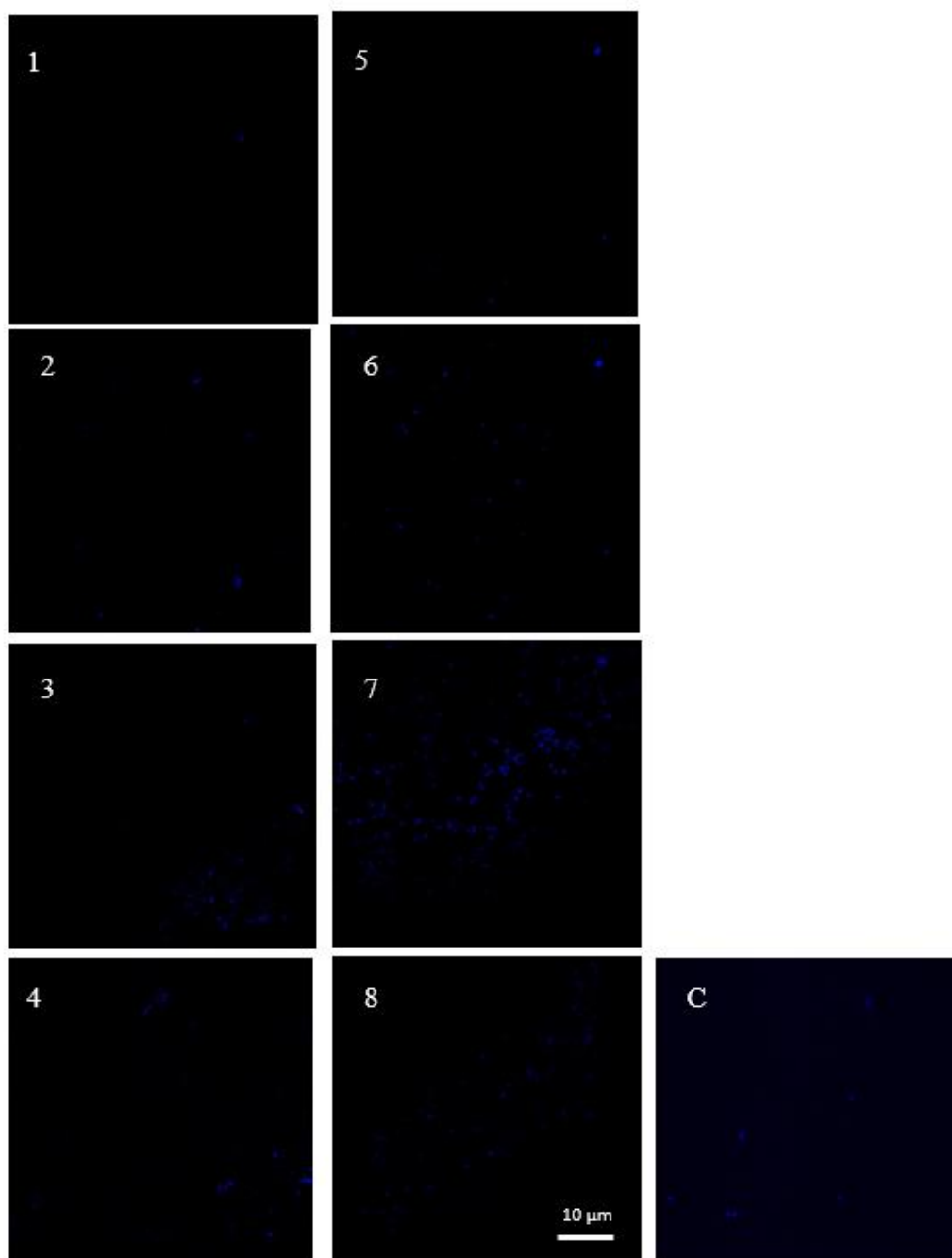


Figure 81. Summary of example images recorded after 48 h of incubation of NHDF cells on material (samples 1-8) and plastic control medium (K). Fluorescence signal of cell nuclei, labelled with DAPI dye; detection with an Olympus FluoView FV1000 confocal microscope in the blue channel; magnification 400 x.

Due to the different structures of the scanned materials, it can be concluded that samples with an uneven and irregular surface create better conditions for fibroblast growth in long-term incubation (Figure 81). The larger surface area allows the use of niches (extra spaces) where

cells proliferate better and faster, which is reflected in the number of cells counted per surface area (Figure 82). The method of counting signals from labelled cell nuclei, similarly, to manually counting them on the image, gives comparable readings (Figures 80 and 82).

Growth of NHDF cells on the material, incubation 48 h

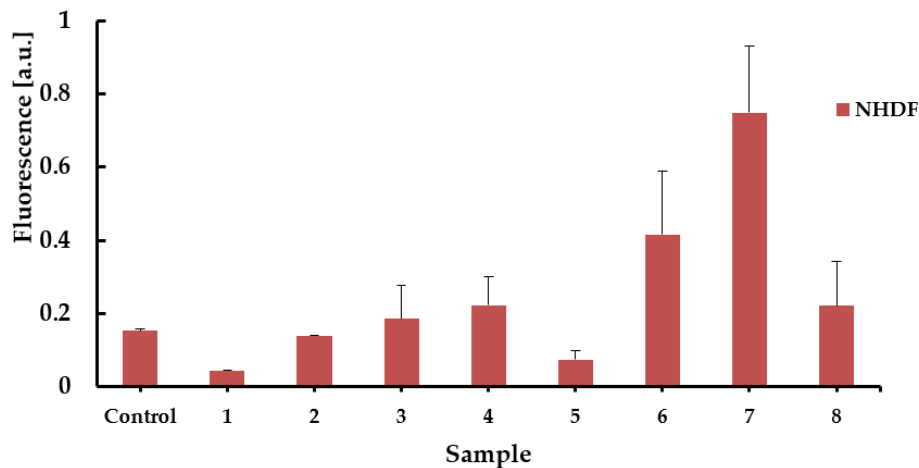


Figure 82. NHDF cell growth on materials, 48 h incubation. Results from fluorescence measurement by automated method; mean of 3 experiments +/- SD.

In a 48-hour growth and biofilm formation test on the materials, it can be concluded that the modified surfaces are suitable for in vitro application, as the growth effects were not reduced below a value of 70% of the number of control cells (cultured on polystyrene control plastics). All steps and tests were performed under sterile conditions, in accordance with the guidelines for the assessment of cytotoxicity according to ISO 10993-5 for the biological evaluation of medical materials by in vitro assays. In the absence of a reduction in the survival fraction below 70 % of the control, the effect of the test material is not considered cytotoxic.

6 Conclusions

Research on the production of a material presenting a thin surface layer enriched in Au on the basis of a material used in medicine and cardiology - Ti and its new generation alloy Ti₁₃Zr₁₃Nb, allowed the following conclusions to be drawn:

1. Titanium and its alloys have a strong tendency to form a heterogeneous, unstable passive layer composed of oxides, which forces the use of etching immediately before the process of electrochemical gold deposition.
2. The composition of the etching bath, etching time, and bath temperature have a decisive influence on the roughness and topography of the material. In order to ensure a sufficiently low roughness (too high roughness may cause local slowing of blood flow and consequently promote thrombus formation), the selection of process parameters was carried out to obtain a material with a target roughness much lower than $R_a = 1.04 \mu\text{m}$ - corresponding to the peripheral roughness of a coronary vessel. Electrochemical gold deposition results in a slight decrease in R_a for Ti and an increase in R_a for Ti₁₃Zr₁₃Nb-substrate material, but no increase in roughness above the assumed value was visualized.
3. Numerical analysis of the heat flow allowed a preliminary assessment of the achieved temperature during laser processing, leading to the observation that in the selected parameters both the substrate material and the coatings (Ti and Au) were in a liquid state allowing dynamic mass exchange between each other following convection movements. The following observations were confirmed empirically using light and electron microscopy
4. The selection of process parameters using laser processing made it possible to establish a parameter window for good coating quality after remelting (avoiding, on the one hand, cracks under quenching stresses and too intensive convection of gold particles preventing stoichiometric concentration allowing crystallization of the Ti₃Au phase, and on the other hand, too low remelting and lack of remelting control). It was shown that the best coating quality is obtained at $P = 100 \text{ W}$, beam rate = 1-3 mm/s and beam deconcentration + 10 mm.
5. Analysis using a wide range of microscopic techniques both in the form of image observation and phase composition determination, as well as XRD analysis allowed us to evaluate the cross-

section of the obtained coatings. Following laser treatment, we obtained multilayered coatings with different concentrations of the enriched element gold Au. The presence of β -Ti₃Au phase in the form of fine crystallites was also revealed in EBSD and TEM analysis.

6. Surface wettability tests indicated an increase in the value of the wetting angle in the direction of hydrophobicity after each successive stage of material processing, but the final coating obtained is still in the hydrophilic range, which has a particularly positive significance for the applicability of the material for biomedical purposes.

7. Corrosion resistance studies generally indicated improved corrosion properties for gold-enriched samples. Studies by EOCP, Tafel curves and EIS techniques allowed a favourable assessment of the material in terms of corrosion behaviour. However, it should be noted the decrease in corrosion resistance in the case of local changes in gold concentration characteristic of the Ti₁₃Zr₁₃Nb 3 mm/s variant, where such a change in concentration leads to the formation of corrosion micro-cells.

8. Investigations of tribological resistance under physiological gait conditions revealed a reduction in the COF friction coefficient, for variants of Ti-based samples, this is undoubtedly related to the combination of laser treatment and the presence of Ti₃Au phase presenting better tribological properties and higher hardness. However, for samples with Ti₁₃Zr₁₃Nb substrate, the COF increases, which is not favourable. The Au coating without laser treatment abrades after 250 s of the experiment.

9. Nano-hardness tests, similar to the numerical analysis of nano-hardness, showed an increase in hardness properties for laser-treated samples having Ti₃Au phases in their composition. Further optimization of the process to maximize the proportion of Ti₃Au in the coating composition seems reasonable.

10. Cytotoxicity tests revealed no toxic effects of the material on the survival of cells seeded on the surface.

The research conducted in this dissertation allows for a positive assessment of the material in terms of both mechanical and biological properties and opens the door for further analysis in accordance with EN 10993-1:2010, "Biological evaluation of medical devices - Part 1: Evaluation and testing in the risk management process.

7 Acknowledgements

I would like to express my gratitude to my parents, Halina and Roman Bialas, my grandmother Katarzyna Marek, and my friend Adam Skowronek, for their valuable discussions, without which this achievement would not have been possible.

At the end of my dissertation, I would like to express my appreciation to Professor Marcin Adamiak for his invaluable support throughout my PhD studies.

The work was partially financially supported by the European Social Fund, grant InterPOWER (POWR.03.05.00-00-Z305)

8 Bibliography

- [1] Wrenn, The Internet Encyclopedia of Philosophy, ISSN 2161-0002, <https://www.iep.utm.edu/priestly/> (23.04.2020r.), (n.d.).
- [2] E.B. Smith, Priestley Conference, BOC Group, eds., Gases in medicine: anaesthesia ; [the proceedings of the BOC Priestley Conference ; held at the Scientific Societies Lecture Theatre, London and Burlington House, London on 22 - 24 April 1997], Cambridge, 1998.
- [3] A. Kluzik, Time perception and general anaesthesia – a historical review, *Anaesthesiology and Rescue Medicine - Poland and the World*. (2010) 14–20.
- [4] J. Thorwald, *Stulecie chirurgów*, Wydawnictwo Literackie, Kraków, 1996.
- [5] D.R. Brothwell, A.T. Sandison, *Diseases in antiquity a survey of the diseases, injuries, and surgery of early populations*, C.C. Thomas, Springfield, Ill., 1967. <http://books.google.com/books?id=AjprAAAAMAAJ> (accessed April 23, 2020).
- [6] J.C.B. Alcázar, R.M.J. Lemos, M.C.M. Conde, L.A. Chisini, M.M.S. Salas, B.S. Noremburg, F.V. da Motta, F.F. Demarco, S.B.C. Tarquinio, N.L.V. Carreño, Preparation, characterization, and biocompatibility of different metal oxide/PEG-based hybrid coating synthesized by sol–gel dip coating method for surface modification of titanium, *Progress in Organic Coatings*. 130 (2019) 206–213. <https://doi.org/10.1016/j.porgcoat.2019.02.007>.

- [7] Y. BhavanChand, R. Ranzani, H. Annapoorani, Evaluation of Hemocompatibility of Titanium after Various Surface Treatments: An in vitro Study, *International Journal of Prosthodontics and Restorative Dentistry*. 2 (2012) 136–142. <https://doi.org/10.5005/jp-journals-10019-1062>.
- [8] X. Gao, M. Fraulob, G. Haïat, Biomechanical behaviours of the bone–implant interface: a review, *J. R. Soc. Interface*. 16 (2019) 20190259. <https://doi.org/10.1098/rsif.2019.0259>.
- [9] I. Przybyszewska-Doroś, W. Okrój, B. Walkowiak, Modyfikacje powierzchni implantów metalicznych, *Inżynieria Biomateriałów*. (2005) 52--62.
- [10] O. Bialas, J. Żmudzki, FEA of displacements and stresses of aortic heart valve leaflets during the opening phase, *Journal of Achievements in Materials and Manufacturing Engineering*. Vol. 92 (2019). <https://doi.org/10.5604/01.3001.0013.3185>.
- [11] K. M, G. J, Wpływ teksturowania powierzchni stopów tytanu na wybrane właściwości endoprotez, *Motrol. Motoryzacja i Energetyka Rolnictwa*. 16 (2014). <http://agro.icm.edu.pl/agro/element/bwmeta1.element.agro-9b0902d2-5fb9-4e96-9052-cf1cb66feb11> (accessed November 3, 2019).
- [12] J. Marciniak, *Biomateriały*, Wydawn. Politechniki Śląskiej, Gliwice, 2002.
- [13] J. Marciniak, *Stenty w chirurgii małoinwazyjnej*, Wydawnictwo Politechniki Śląskiej, Gliwice, 2006.
- [14] D.L. Bark, H. Vahabi, H. Bui, S. Movafaghi, B. Moore, A.K. Kota, K. Popat, L.P. Dasi, Hemodynamic Performance and Thrombogenic Properties of a Superhydrophobic Bileaflet Mechanical Heart Valve, *Ann Biomed Eng*. 45 (2017) 452–463. <https://doi.org/10.1007/s10439-016-1618-2>.
- [15] O. Bialas, J. Żmudzki, M. Adamiak, Advanced polymeric materials for reconstructive treatment after the intra-oral tumor resections, 12 (2020) 9–16.
- [16] R.G. Craig, J.M. Powers, R.L. Sakaguchi, H. Limanowska-Shaw, J.G. Shaw, E. Andrzejewska, *Materiały stomatologiczne*, Elsevier Urban & Partner, Wrocław, 2008.
- [17] H. Hermawan, D. Ramdan, J.R. P. Djuansjah, *Metals for Biomedical Applications*, in: R. Fazel (Ed.), *Biomedical Engineering - From Theory to Applications*, InTech, 2011. <https://doi.org/10.5772/19033>.
- [18] B. Świczko-Żurek, *Biomateriały*, Biblioteka Politechniki Gdańskiej, Gdańsk, 2009. http://pbc.gda.pl/Content/4527/pbc_biomaterialy_swieczko.pdf.

- [19] J. Marciniak, M. Kaczmarek, A. Ziębowicz, *Biomateriały w stomatologii*, Wydawnictwo Politechniki Śląskiej, Gliwice, 2008.
- [20] B.D. Ratner, ed., *Biomaterials science: an introduction to materials in medicine*, 2nd ed, Elsevier Academic Press, Amsterdam ; Boston, 2004.
- [21] C.N. Elias, J.H.C. Lima, R. Valiev, M.A. Meyers, Biomedical applications of titanium and its alloys, *JOM*. 60 (2008) 46–49. <https://doi.org/10.1007/s11837-008-0031-1>.
- [22] S. Dai, Y. Wang, F. Chen, X. Yu, Y. Zhang, Design of new biomedical titanium alloy based on d-electron alloy design theory and JMatPro software, *Transactions of Nonferrous Metals Society of China*. 23 (2013) 3027–3032. [https://doi.org/10.1016/S1003-6326\(13\)62829-0](https://doi.org/10.1016/S1003-6326(13)62829-0).
- [23] A. Wennerberg, T. Albrektsson, Effects of titanium surface topography on bone integration: a systematic review, *Clin Oral Implants Res*. 20 Suppl 4 (2009) 172–184. <https://doi.org/10.1111/j.1600-0501.2009.01775.x>.
- [24] A. Woźniak, M. Adamiak, G. Chladek, M. Bonek, W. Walke, O. Bialas, The Influence of Hybrid Surface Modification on the Selected Properties of CP Titanium Grade II Manufactured by Selective Laser Melting, *Materials*. 13 (2020) 2829. <https://doi.org/10.3390/ma13122829>.
- [25] P. Hallam, F. Haddad, J. Cobb, Pain in the well-fixed, aseptic titanium hip replacement: THE ROLE OF CORROSION, *The Journal of Bone and Joint Surgery. British Volume*. 86-B (2004) 27–30. <https://doi.org/10.1302/0301-620X.86B1.14326>.
- [26] I.N. Safi, B.M.A. Hussein, A.M. Al Shammari, T.A. Tawfiq, Implementation and characterization of coating pure titanium dental implant with sintered β -TCP by using Nd:YAG laser, *Saudi Dent J*. 31 (2019) 242–250. <https://doi.org/10.1016/j.sdentj.2018.12.004>.
- [27] G.C. Babis, N.A. Stavropoulos, G. Sasalos, M. Ochsenkuehn-Petropoulou, P. Megas, Metallosis and elevated serum levels of tantalum following failed revision hip arthroplasty— a case report, *Acta Orthopaedica*. 85 (2014) 677–680. <https://doi.org/10.3109/17453674.2014.950816>.
- [28] K.H. Salem, N. Lindner, M. Tingart, A.D. Elmoghazy, Severe metallosis-related osteolysis as a cause of failure after total knee replacement, *Journal of Clinical Orthopaedics and Trauma*. 11 (2020) 165–170. <https://doi.org/10.1016/j.jcot.2019.04.010>.

- [29] T. Furuzono, M. Okazaki, Y. Azuma, M. Iwasaki, Y. Kogai, Y. Sawa, Newly Developed Biocompatible Material: Dispersible Titanium-Doped Hydroxyapatite Nanoparticles Suitable for Antibacterial Coating on Intravascular Catheters, in: H. Kawanishi, Y. Takemoto (Eds.), *Contributions to Nephrology*, S. Karger AG, 2017: pp. 144–152. <https://doi.org/10.1159/000450744>.
- [30] G. Gafner, The development of 990 gold-titanium: its production, use and properties, *Gold Bull.* 22 (1989).
- [31] E. Svanidze, T. Besara, M.F. Ozaydin, C.S. Tiwary, J.K. Wang, S. Radhakrishnan, S. Mani, Y. Xin, K. Han, H. Liang, T. Siegrist, P.M. Ajayan, E. Morosan, High hardness in the biocompatible intermetallic compound β -Ti₃Au, *Sci. Adv.* 2 (2016) e1600319. <https://doi.org/10.1126/sciadv.1600319>.
- [32] J. Fischer, Mechanical, thermal, and chemical analyses of the binary system Au-Ti in the development of a dental alloy., *Journal of Biomedical Materials Research.* 54 (2000) 678–686. [https://doi.org/10.1002/1097-4636\(20001215\)52:4<678::aid-jbm12>3.0.co;2-p](https://doi.org/10.1002/1097-4636(20001215)52:4<678::aid-jbm12>3.0.co;2-p).
- [33] R. Shukla, V. Bansal, M. Chaudhary, A. Basu, R.R. Bhonde, M. Sastry, Biocompatibility of Gold Nanoparticles and Their Endocytotic Fate Inside the Cellular Compartment: A Microscopic Overview, *Langmuir.* 21 (2005) 10644–10654. <https://doi.org/10.1021/la0513712>.
- [34] O. Bialas, T. Poloczek, M. Lis, A. Skowronek, J. Górka, M. Adamiak, Laser Assisted Size Reduction of Gold (Au) Particles onto a Titanium (Ti) Substrate Surface, *Applied Sciences.* 11 (2021) 8755. <https://doi.org/10.3390/app11188755>.
- [35] O. Bialas, M. Lis, A. Woźniak, M. Adamiak, Laser Superficial Fusion of Gold Nanoparticles with PEEK Polymer for Cardiovascular Application, *Materials.* 14 (2021) 971. <https://doi.org/10.3390/ma14040971>.
- [36] J.-E. Sundgren, P. Bodö, B. Ivarsson, I. Lundström, Adsorption of Fibrinogen on Titanium and Gold Surfaces Studied by ESCA and Ellipsometry, *Journal of Colloid and Interface Science.* 113 (1986) 530–543. [https://doi.org/10.1016/S0021-9797\(86\)90446-7](https://doi.org/10.1016/S0021-9797(86)90446-7).
- [37] A. Asserghine, D. Filotás, L. Nagy, R.M. Souto, G. Nagy, Do titanium biomaterials get immediately and entirely repassivated? A perspective, *Npj Mater Degrad.* 6 (2022) 57. <https://doi.org/10.1038/s41529-022-00270-0>.

- [38] T. Hanawa, Transition of surface modification of titanium for medical and dental use, in: *Titanium in Medical and Dental Applications*, Elsevier, 2018: pp. 95–113. <https://doi.org/10.1016/B978-0-12-812456-7.00005-6>.
- [39] T. Kodama, R. Nakai, K. Goto, K. Shima, H. Iwata, Preparation of an Au-Pt alloy free from artifacts in magnetic resonance imaging, *Magnetic Resonance Imaging*. 44 (2017) 38–45. <https://doi.org/10.1016/j.mri.2017.07.006>.
- [40] M.A. van der Jagt, W.M. Brink, M.J. Versluis, S.C.A. Steens, J.J. Briaire, A.G. Webb, J.H.M. Frijns, B.M. Verbist, Visualization of Human Inner Ear Anatomy with High-Resolution MR Imaging at 7T: Initial Clinical Assessment, *AJNR Am J Neuroradiol*. 36 (2015) 378–383. <https://doi.org/10.3174/ajnr.A4084>.
- [41] D.S. Thylur, R.E. Jacobs, J.L. Go, A.W. Toga, J.K. Niparko, Ultra-High-Field Magnetic Resonance Imaging of the Human Inner Ear at 11.7 Tesla, *Otology & Neurotology*. 38 (2017) 133–138. <https://doi.org/10.1097/MAO.0000000000001242>.
- [42] J. Starčuková, Z. Starčuk, H. Hubáľková, I. Linetskiy, Magnetic susceptibility and electrical conductivity of metallic dental materials and their impact on MR imaging artifacts, *Dental Materials*. 24 (2008) 715–723. <https://doi.org/10.1016/j.dental.2007.07.002>.
- [43] H. Okamoto, M.E. Schlesinger, E.M. Mueller, eds., *Au (Gold) Binary Alloy Phase Diagrams*, in: *Alloy Phase Diagrams*, ASM International, 2016: pp. 152–174. <https://doi.org/10.31399/asm.hb.v03.a0006146>.
- [44] R.L. Williams, ed., *Surface modification of biomaterials: methods, analysis and applications*, Woodhead Pub, Cambridge ; Philadelphia, PA, 2011.
- [45] R.K. Murray, D.K. Granner, V.W. Rodwell, F. Kokot, Z. Aleksandrowicz, H.A. Harper, *Biochemia Harpera ilustrowana*, Wydawnictwo Lekarskie PZWL, Warszawa, 2008.
- [46] G.D. Dangas, J.I. Weitz, G. Giustino, R. Makkar, R. Mehran, Prosthetic Heart Valve Thrombosis, *Journal of the American College of Cardiology*. 68 (2016) 2670–2689. <https://doi.org/10.1016/j.jacc.2016.09.958>.
- [47] A. Mikłaszewski, M. Jurczyk, M. Jurczyk, Modyfikacja warstwy wierzchniej biomateriałów na przykładzie tytanu metodą stopowania plazmowego, *Welding Technology Review*. 83 (2011). <https://doi.org/10.26628/wtr.v83i12.442>.

- [48] P. Trisi, M. Todisco, U. Consolo, D. Travaglini, High versus low implant insertion torque: a histologic, histomorphometric, and biomechanical study in the sheep mandible, *Int J Oral Maxillofac Implants*. 26 (2011) 837–849.
- [49] T. Grandi, P. Guazzi, R. Samarani, G. Grandi, Clinical outcome and bone healing of implants placed with high insertion torque: 12-month results from a multicenter controlled cohort study, *International Journal of Oral and Maxillofacial Surgery*. 42 (2013) 516–520. <https://doi.org/10.1016/j.ijom.2012.10.013>.
- [50] <http://www.enviromet.eu/tox/eko.htm> (dostęp z dnia 10.11.2019r.), n.d.
- [51] M. Zhang, D. Aguilera, C. Das, H. Vasquez, P. Zage, V. Gopalakrishnan, J. Wolff, Measuring Cytotoxicity: A New Perspective on LC50, *ANTICANCER RESEARCH*. (2007) 4.
- [52] A.I. Nicolas-Silvente, E. Velasco-Ortega, I. Ortiz-Garcia, L. Monsalve-Guil, J. Gil, A. Jimenez-Guerra, Influence of the Titanium Implant Surface Treatment on the Surface Roughness and Chemical Composition, *Materials (Basel)*. 13 (2020). <https://doi.org/10.3390/ma13020314>.
- [53] A. Brizuela, M. Herrero-Climent, E. Rios-Carrasco, J. Rios-Santos, R. Pérez, J. Manero, J. Gil Mur, Influence of the Elastic Modulus on the Osseointegration of Dental Implants, *Materials*. 12 (2019) 980. <https://doi.org/10.3390/ma12060980>.
- [54] B. Major, *Ablacja i osadzanie laserem impulsowym*, Akapit, Kraków, 2002.
- [55] G. Singh, Surface Treatment of dental implants: a review, *IOSR-JDMS*. 17 (2018). <https://doi.org/DOI:10.9790/0853-1702154953>.
- [56] A. Shah, S. Izman, S. Ismail, H. Mas Ayu, C. Che Kob, R. Daud, M. Abdul Kadir, The Influence of Ultrasonic Vibration Frequency on the Properties of TiN Coated Biomedical Ti–13Zr–13Nb, *Metals*. 8 (2018) 317. <https://doi.org/10.3390/met8050317>.
- [57] <https://encyklopedia.pwn.pl/haslo/pasywacja;3954910.html> (dostęp z dnia 10.11.2019r.), n.d.
- [58] Y.-Y. Chang, J.-H. Zhang, H.-L. Huang, Effects of Laser Texture Oxidation and High-Temperature Annealing of TiV Alloy Thin Films on Mechanical and Antibacterial Properties and Cytotoxicity, *Materials*. 11 (2018) 2495. <https://doi.org/10.3390/ma11122495>.

- [59] S.G. Hatzikiriakos, S. Moradi, S. Kamal, Superhydrophobic laser-ablated stainless steel substrates exhibiting Cassie–Baxter stable state, *Surface Innovations*. 3 (2015) 151–163. <https://doi.org/10.1680/sufi.15.00001>.
- [60] V. Jokinen, E. Kankuri, S. Hoshian, S. Franssila, R.H.A. Ras, Superhydrophobic Blood-Repellent Surfaces, *Adv. Mater.* 30 (2018) 1705104. <https://doi.org/10.1002/adma.201705104>.
- [61] T. Jiang, J. Koch, C. Unger, E. Fadeeva, A. Koroleva, Q. Zhao, B.N. Chichkov, Ultrashort picosecond laser processing of micro-molds for fabricating plastic parts with superhydrophobic surfaces, *Appl. Phys. A*. 108 (2012) 863–869. <https://doi.org/10.1007/s00339-012-6985-4>.
- [62] L. Wojciechowski, K.J. Kubiak, T.G. Mathia, Impact of morphological furrows as lubricant reservoir on creation of oleophilic and oleophobic behaviour of metallic surfaces in scuffing, *Tribology International*. 116 (2017) 320–328. <https://doi.org/10.1016/j.triboint.2017.07.020>.
- [63] N. Donos, S. Hamlet, N.P. Lang, G.E. Salvi, G. Huynh-Ba, D.D. Bosshardt, S. Ivanovski, Gene expression profile of osseointegration of a hydrophilic compared with a hydrophobic microrough implant surface: Gene expression during osseointegration of modified surfaces, *Clinical Oral Implants Research*. 22 (2011) 365–372. <https://doi.org/10.1111/j.1600-0501.2010.02113.x>.
- [64] W. Ze, T. Wen-sheng, Ye-Xia, Z. Ming, L. Xiao-ping, Q. Jian-guo, Y. Xiao-Hong, Preparation of anticoagulant PyC biomaterials with super-hydrophobic surface, *Journal of Applied Biomaterials & Functional Materials*. 16 (2018) 125–131. <https://doi.org/10.1177/2280800017753315>.
- [65] J. Marciniak, W. Chrzanowski, A. Kajzer, *Gwoździowanie śródszpikowe w osteosyntezie*, Wydawnictwo Politechniki Śląskiej, Gliwice, 2006.
- [66] A. Woźniak, M. Staszuk, Ł. Reimann, O. Bialas, Z. Brytan, S. Voinarovych, O. Kyslytsia, S. Kaliuzhnyi, M. Basiaga, M. Admiak, The influence of plasma-sprayed coatings on surface properties and corrosion resistance of 316L stainless steel for possible implant application, *Archiv.Civ.Mech.Eng.* 21 (2021) 148. <https://doi.org/10.1007/s43452-021-00297-1>.
- [67] T. Burakowski, *Inżynieria powierzchni metali: [podstawy, urządzenia, technologie]*, Wydaw. Naukowo-Techniczne, Warszawa, 1995.

- [68] M. Catauro, F. Barrino, M. Bononi, E. Colombini, R. Giovanardi, P. Veronesi, E. Tranquillo, Coating of Titanium Substrates with ZrO₂ and ZrO₂-SiO₂ Composites by Sol-Gel Synthesis for Biomedical Applications: Structural Characterization, Mechanical and Corrosive Behavior, *Coatings*. 9 (2019) 200. <https://doi.org/10.3390/coatings9030200>.
- [69] B.E. Pippenger, M. Rottmar, B.S. Kopf, S. Stübinger, F.H. Dalla Torre, S. Berner, K. Maniura-Weber, Surface modification of ultrafine-grained titanium: Influence on mechanical properties, cytocompatibility, and osseointegration potential, *Clinical Oral Implants Research*. 30 (2019) 99–110. <https://doi.org/10.1111/clr.13396>.
- [70] A. Woźniak, A. Ziębowicz, B. Ziębowicz, W. Walke, Physicochemical properties of oxide ZrO₂ layer deposited by sol-gel method on Ti-6Al-7Nb alloy, *Archives of Metallurgy and Materials*. 63 (2018). <https://doi.org/10.24425/123793>.
- [71] A. Woźniak, O. Bialas, M. Adamiak, Improvement of the properties of Ti6Al7Nb titanium alloy in terms of the type of surface modification, *Archives of Metallurgy and Materials*. 65 (2020) 759–765. [https://doi.org/DOI: 10.24425/amm.2020.132816](https://doi.org/DOI:10.24425/amm.2020.132816).
- [72] D. Williams, Laser basics, *Anaesthesia & Intensive Care Medicine*. 9 (2008) 550–552. <https://doi.org/10.1016/j.mpaic.2008.09.008>.
- [73] C. Wang, W. Suder, J. Ding, S. Williams, Wire based plasma arc and laser hybrid additive manufacture of Ti-6Al-4V, *Journal of Materials Processing Technology*. 293 (2021) 117080. <https://doi.org/10.1016/j.jmatprotec.2021.117080>.
- [74] N.G.C. Astrath, F.B.G. Astrath, J. Shen, J. Zhou, C.E. Gu, L.C. Malacarne, P.R.B. Pedreira, A.C. Bento, M.L. Baesso, Top-hat cw laser induced thermal mirror: a complete model for material characterization, *Appl. Phys. B*. 94 (2009) 473–481. <https://doi.org/10.1007/s00340-008-3310-1>.
- [75] C. Chan, J. Mazumder, M.M. Chen, A two-dimensional transient model for convection in laser melted pool, *MTA*. 15 (1984) 2175–2184. <https://doi.org/10.1007/BF02647100>.
- [76] M. Bonek, Laser Surface Alloying, in: Q.J. Wang, Y.-W. Chung (Eds.), *Encyclopedia of Tribology*, Springer US, Boston, MA, 2013: pp. 1938–1948. https://doi.org/10.1007/978-0-387-92897-5_687.
- [77] I. Rajagopal, K.S. Rajam, S.R. Rajagopalan, Gold plating of critical components for space applications: Challenges and solutions, *Gold Bull*. 25 (1992) 55–66. <https://doi.org/10.1007/BF03214720>.

- [78] C.C. Camilo, E.C. de Souza, P.L. Di Lorenzo, J.M.D. de A. Rollo, Measurement of the grain boundary energy of commercially-pure grade 2 titanium at high temperature, *RBEB*. 27 (2011) 175–181. <https://doi.org/10.4322/rbeb.2011.014>.
- [79] ASTM B348/B348M, 2019, (n.d.).
- [80] M. Bartmański, Ł. Pawłowski, A. Belcarz, A. Przekora, G. Ginalska, G. Strugała, B.M. Cieślik, A. Pałubicka, A. Zieliński, The Chemical and Biological Properties of Nanohydroxyapatite Coatings with Antibacterial Nanometals, Obtained in the Electrophoretic Process on the Ti13Zr13Nb Alloy, *IJMS*. 22 (2021) 3172. <https://doi.org/10.3390/ijms22063172>.
- [81] D.G. Owen, T. Schenkel, D.E.T. Shepherd, D.M. Espino, Assessment of surface roughness and blood rheology on local coronary haemodynamics: a multi-scale computational fluid dynamics study, *J. R. Soc. Interface*. 17 (2020) 20200327. <https://doi.org/10.1098/rsif.2020.0327>.
- [82] T. Kunimine, R. Miyazaki, Y. Yamashita, Y. Funada, Effects of Laser-Beam Defocus on Microstructural Features of Compositionally Graded WC/Co-Alloy Composites Additively Manufactured by Multi-Beam Laser Directed Energy Deposition, *Sci Rep*. 10 (2020) 8975. <https://doi.org/10.1038/s41598-020-65429-8>.
- [83] A. Kunwar, L. An, J. Liu, S. Shang, P. Råback, H. Ma, X. Song, A data-driven framework to predict the morphology of interfacial Cu₆Sn₅ IMC in SAC/Cu system during laser soldering, *Journal of Materials Science & Technology*. 50 (2020) 115–127. <https://doi.org/10.1016/j.jmst.2019.12.036>.
- [84] W.-H. Xiong, W. Liu, M.-M. Dai, J.-Q. Liu, X.-G. Lu, Assessments of molar volumes of Co-, Ni- and Ti- related bcc and fcc phases, *Calphad*. 66 (2019) 101629. <https://doi.org/10.1016/j.calphad.2019.101629>.
- [85] B. Sundman, U.R. Kattner, M. Palumbo, S.G. Fries, OpenCalphad - a free thermodynamic software, *Integr Mater Manuf Innov*. 4 (2015) 1–15. <https://doi.org/10.1186/s40192-014-0029-1>.
- [86] K. Schüller, J. Kowalski, P. Råback, Curvilinear melting – A preliminary experimental and numerical study, *International Journal of Heat and Mass Transfer*. 92 (2016) 884–892. <https://doi.org/10.1016/j.ijheatmasstransfer.2015.09.046>.

- [87] S. Zhu, T.P. Chen, Z.H. Cen, E.S.M. Goh, S.F. Yu, Y.C. Liu, Y. Liu, Split of surface plasmon resonance of gold nanoparticles on silicon substrate: a study of dielectric functions, *Opt. Express*. 18 (2010) 21926. <https://doi.org/10.1364/OE.18.021926>.
- [88] A. Kunwar, J. Givernaud, H. Ma, Z. Meng, S. Shang, Y. Wang, H. Ma, Modelling the melting of Sn_{0.7}Cu solder using the enthalpy method, in: 2016 17th International Conference on Electronic Packaging Technology (ICEPT), IEEE, Wuhan, China, 2016: pp. 166–169. <https://doi.org/10.1109/ICEPT.2016.7583112>.
- [89] E. Ricci, R. Novakovic, Wetting and surface tension measurements on gold alloys, *Gold Bull.* 34 (2001) 41–49. <https://doi.org/10.1007/BF03214811>.
- [90] P. Paradisa, T. Ishikawaa, N. Koikeb, Density of liquid gold measured by a non-contact technique, *Gold Bull.* 41 (2008) 242–245. <https://doi.org/10.1007/BF03214876>.
- [91] X.-P. Zhang, G. Chen, S.-M. Xiong, Q.-Y. Xu, Computer simulation of the solidification of cast titanium dental prostheses, *J Mater Sci.* 40 (2005) 4911–4916. <https://doi.org/10.1007/s10853-005-0418-0>.
- [92] H. Wang, S. Yang, B. Wei, Density and structure of undercooled liquid titanium, *Chin. Sci. Bull.* 57 (2012) 719–723. <https://doi.org/10.1007/s11434-011-4945-6>.
- [93] J.G. Cook, M.P. van der Meer, The thermal conductivity and electrical resistivity of gold from 80 to 340 K, *Can. J. Phys.* 48 (1970) 254–263. <https://doi.org/10.1139/p70-035>.
- [94] Y.V. Petrov, N.A. Inogamov, S.I. Anisimov, K.P. Migdal, V.A. Khokhlov, K.V. Khishchenko, Thermal conductivity of condensed gold in states with the strongly excited electron subsystem, *J. Phys.: Conf. Ser.* 653 (2015) 012087. <https://doi.org/10.1088/1742-6596/653/1/012087>.
- [95] M. Watanabe, M. Adachi, H. Fukuyama, Heat capacities and thermal conductivities of palladium and titanium melts and correlation between thermal diffusivity and density of states for transition metals in a liquid state, *Journal of Molecular Liquids.* 324 (2021) 115138. <https://doi.org/10.1016/j.molliq.2020.115138>.
- [96] X.W. Zhou, R.A. Johnson, H.N.G. Wadley, Misfit-energy-increasing dislocations in vapor-deposited CoFe/NiFe multilayers, *Phys. Rev. B.* 69 (2004) 144113. <https://doi.org/10.1103/PhysRevB.69.144113>.
- [97] S. Plimpton, Fast Parallel Algorithms for Short-Range Molecular Dynamics, *Journal of Computational Physics.* 117 (1995) 1–19. <https://doi.org/10.1006/jcph.1995.1039>.

- [98] R.-G. Xu, H. Song, Y. Leng, S. Papanikolaou, A Molecular Dynamics Simulations Study of the Influence of Prestrain on the Pop-in Behavior and Indentation Size Effect in Cu Single Crystals, *MATERIALS SCIENCE*, 2021. <https://doi.org/10.20944/preprints202108.0151.v1>.
- [99] A. Stukowski, Visualization and analysis of atomistic simulation data with OVITO—the Open Visualization Tool, *Modelling Simul. Mater. Sci. Eng.* 18 (2010) 015012. <https://doi.org/10.1088/0965-0393/18/1/015012>.
- [100] P. Hirel, AtomsK: A tool for manipulating and converting atomic data files, *Computer Physics Communications.* 197 (2015) 212–219. <https://doi.org/10.1016/j.cpc.2015.07.012>.
- [101] S. Wu, Z. Kou, Q. Lai, S. Lan, S.S. Katnagallu, H. Hahn, S. Taheriniya, G. Wilde, H. Gleiter, T. Feng, Dislocation exhaustion and ultra-hardening of nanograined metals by phase transformation at grain boundaries, *Nat Commun.* 13 (2022) 5468. <https://doi.org/10.1038/s41467-022-33257-1>.
- [102] A.V. Verkhovtsev, A.V. Yakubovich, G.B. Sushko, M. Hanauske, A.V. Solov'yov, Molecular dynamics simulations of the nanoindentation process of titanium crystal, *Computational Materials Science.* 76 (2013) 20–26. <https://doi.org/10.1016/j.commatsci.2013.02.015>.
- [103] S. Amaya-Roncancio, E. Restrepo-Parra, D.M. Devia-Narvaez, D.F. Arias- Mateus, M.M. Gómez-Hermida, Molecular dynamics simulation of nanoindentation in Cr, Al layers and Al/Cr bilayers, using a hard spherical nanoindenter, 81 (2014) 102–107.
- [104] Y. Kamegaya, K. Sasaki, M. Oguri, T. Asaki, H. Kobayashi, T. Mitamura, Improved durability of iridium oxide coated titanium anode with interlayers for oxygen evolution at high current densities, *Electrochimica Acta.* 40 (1995) 889–895. [https://doi.org/10.1016/0013-4686\(94\)00339-3](https://doi.org/10.1016/0013-4686(94)00339-3).
- [105] F. Laves, H. Philipsborn, The influence of impurities on the formation of the Cu₃ Au - type structure from the Cr₃ Si - type, *Acta Crystallographica.* 17 (1964) 213–214.
- [106] K. Schubert, E. Stolz, Strukturuntersuchungen in einigen T(4)-B(1) homologen und quasihomologen Systemen, *Zeitschrift Fuer Metallkunde.* (1962) 433–555.
- [107] J. Zemann, *Crystal structures, 2nd edition. Vol. 1* by R. W. G. Wyckoff, *Acta Cryst.* 18 (1965) 139–139. <https://doi.org/10.1107/S0365110X65000361>.

- [108] R.B.A. Nor Asma, P.A. Yuli, C.I. Mokhtar, Study on the Effect of Surface Finish on Corrosion of Carbon Steel in CO₂ Environment, *J. of Applied Sciences*. 11 (2011) 2053–2057. <https://doi.org/10.3923/jas.2011.2053.2057>.
- [109] A. Toloei, V. Stoilov, D. Northwood, The Relationship Between Surface Roughness and Corrosion, in: *Volume 2B: Advanced Manufacturing*, American Society of Mechanical Engineers, San Diego, California, USA, 2013: p. V02BT02A054. <https://doi.org/10.1115/IMECE2013-65498>.
- [110] Y.-R. Lee, M.-K. Han, M.-K. Kim, W.-J. Moon, H.-J. Song, Y.-J. Park, Effect of gold addition on the microstructure, mechanical properties and corrosion behavior of Ti alloys, *Gold Bull.* 47 (2014) 153–160. <https://doi.org/10.1007/s13404-014-0138-9>.
- [111] M. Takahashi, M. Kikuchi, Y. Takada, O. Okuno, T. Okabe, Corrosion Behavior and Microstructures of Experimental Ti-Au Alloys, *Dental Materials Journal*. 23 (2004) 109–116. <https://doi.org/10.4012/dmj.23.109>.
- [112] W. Shang, B. Chen, X. Shi, Y. Chen, X. Xiao, Electrochemical corrosion behavior of composite MAO/sol–gel coatings on magnesium alloy AZ91D using combined micro-arc oxidation and sol–gel technique, *Journal of Alloys and Compounds*. 474 (2009) 541–545. <https://doi.org/10.1016/j.jallcom.2008.06.135>.
- [113] K. Jüttner, Electrochemical impedance spectroscopy (EIS) of corrosion processes on inhomogeneous surfaces, *Electrochimica Acta*. 35 (1990) 1501–1508. [https://doi.org/10.1016/0013-4686\(90\)80004-8](https://doi.org/10.1016/0013-4686(90)80004-8).
- [114] B.D. Beake, T.W. Liskiewicz, Comparison of nano-fretting and nano-scratch tests on biomedical materials, *Tribology International*. 63 (2013) 123–131. <https://doi.org/10.1016/j.triboint.2012.08.007>.
- [115] Y.X. Ou, J. Lin, H.L. Che, W.D. Sproul, J.J. Moore, M.K. Lei, Mechanical and tribological properties of CrN/TiN multilayer coatings deposited by pulsed dc magnetron sputtering, *Surface and Coatings Technology*. 276 (2015) 152–159. <https://doi.org/10.1016/j.surfcoat.2015.06.064>.
- [116] V.S. de Viteri, E. Fuentes, Titanium and Titanium Alloys as Biomaterials, in: J. Gegner (Ed.), *Tribology - Fundamentals and Advancements*, InTech, 2013. <https://doi.org/10.5772/55860>.
- [117] M. Conradi, A. Kocijan, D. Klobčar, B. Podgornik, Tribological response of laser-textured Ti6Al4V alloy under dry conditions and lubricated with Hank's solution,

Tribology International. 160 (2021) 107049.
<https://doi.org/10.1016/j.triboint.2021.107049>.

- [118] M. Geetha, A.K. Singh, R. Asokamani, A.K. Gogia, Ti based biomaterials, the ultimate choice for orthopaedic implants – A review, *Progress in Materials Science*. 54 (2009) 397–425. <https://doi.org/10.1016/j.pmatsci.2008.06.004>.
- [119] <https://www.azom.com/article.aspx?ArticleID=1965> (access online 01.12.2022), (n.d.).